

UNIVERSITY OF TECHNOLOGY, SYDNEY

Model-Aided State Estimation for Quadrotor Micro Aerial Vehicles

by

Dinuka Malin Wickramasinghe Abeywardena

A thesis submitted in partial fulfillment for the
degree of Doctor of Philosophy

in the
Faculty of Engineering and IT
Centre of Autonomous Systems

February 2015

Declaration of Authorship

I certify that the work in this thesis has not previously been submitted for a degree nor has it been submitted as part of requirements for a degree except as fully acknowledged within the text.

I also certify that the thesis has been written by me. Any help that I have received in my research work and the preparation of the thesis itself has been acknowledged. In addition, I certify that all information sources and literature used are indicated in the thesis.

Signature of Student:

Date:

UNIVERSITY OF TECHNOLOGY, SYDNEY

Abstract

Faculty of Engineering and IT
Centre of Autonomous Systems

Doctor of Philosophy

by Dinuka Malin Wickramasinghe Abeywardena

Due to their manoeuvrability, compactness and vertical take-off and landing capability, quadrotor Micro Aerial Vehicles (MAV) are ideally suited to assist or replace humans in a host of tasks in urban and indoor environments that would otherwise be hazardous, tedious or expensive. However, obtaining reliable pose estimates to perform these tasks safely and efficiently is a significant challenge due to the limited accuracy of GPS in such environments. This thesis presents algorithms for pose estimation of quadrotor Micro Aerial Vehicles (MAVs) operating in GPS-denied environments. The main contributions of the thesis stem from the use of the dynamic model describing the motion of a quadrotor as an additional source of information during state estimation.

A state estimator design for quadrotor MAVs that only employs consumer grade inertial sensors is first proposed. Two major improvements to the conventional inertial only state estimators for MAVs are demonstrated. First, it is shown that incorporating an appropriate dynamic model improves the accuracy of the MAV attitude estimate. Second, in contrast to the conventional designs, it is shown that the new estimator provides a drift free estimate of the horizontal components of the quadrotor body frame velocity. These velocity estimates can be exploited to substantially improve the stability and controllability of a quadrotor MAV.

In addition to inertial sensors, monocular cameras provide an excellent source of information that can be used for the MAV state estimation task. The complementary nature of visual and inertial information means that a fusion of the two information sources can improve the accuracy and robustness of the state estimation algorithms. This thesis demonstrates that further improvements in accuracy and robustness can be obtained by incorporating the quadrotor dynamic model into visual-inertial fusion algorithms. The resulting state estimator design is capable of producing reliable pose estimates even when the quadrotor MAV is travelling at a constant velocity, a case which is known to be difficult to handle with conventional algorithms. A theoretical analysis using Lie derivatives is presented to verify this improvement in observability. Extensive simulations and experiments in a number of practical situations are presented to demonstrate the effectiveness of the proposed methodology and to demonstrate that it outperforms conventional visual-inertial fusion methods.

Employing the dynamic model to aid the state estimation can also be extended to deal with wind disturbances that would otherwise hamper the performance of lightweight quadrotor MAVs. This thesis demonstrates that explicit modelling of the effects of wind on the quadrotor dynamics enables the simultaneous estimation of the vehicle pose and two components of wind velocity, using only a monocular camera and an inertial measurement unit. This design is validated through a non-linear observability analysis and extensive simulations that makes use of a realistic wind model. Experimental results in a controlled lab environment are also presented to demonstrate the effectiveness of the proposed state estimator.

Acknowledgements

I am sincerely in debt to my supervisors, Professor Gamini Dissanayke and Associate Professor Sarath Kodagoda, for believing in me and for giving me a freehand to work on my lifelong passion. Their continuous support, guidance and enthusiasm made this feat both achievable and memorable. Thanks for the countless hours of thought provoking discussions, both technical and otherwise, for they were the bits that I enjoyed the most.

I would also like to thank Dr. Zhan Wang and Assistant Professor Steven Waslander for the fruitful discussions and for their continuous encouragement. Thanks also to Professor Robert Mahony for the much enjoyed stay with the ANU Computer Vision and Robotics group.

To all my friends at CAS, thanks for the four years of good laughs, best ever games of badminton and above all, unrivalled comradeship. To all the academic and support staff at CAS, thanks for taking me in and making me part of the family. Never have I felt more at home than in these past four years.

I would also like to thank professor Rohan Munasinghe, for believing that nothing was impossible and for the guidance during the early days of my research. Thanks also to my friends Amila, Yasiru, Shakoor, Mahesh and Senaka for being there with me through thick and thin and for sharing my passion for aerial robotics.

Finally, I am ever in debt to my family who made great sacrifices in making me who I am today.

Contents

Certificate Of Original Authorship	i
Abstract	ii
Acknowledgements	v
List of Figures	ix
List of Tables	xi
Abbreviations	xii
Nomenclature	xiii
Glossary of Terms	xvi
1 Introduction	1
1.1 Micro Aerial Vehicles	1
1.1.1 Multi-rotor MAVs	2
1.2 Motivation and Objectives	3
1.3 Contributions	5
1.4 Thesis Outline	7
1.5 Publications	9
2 Theoretical and Experimental Background	10
2.1 Introduction	10
2.2 Quadrotor MAVs, An Introduction	11
2.3 Frame Definitions and States	12
2.4 Dynamics of a Quadrotor MAV	14
2.4.1 Rigid Body Dynamics	14
2.4.2 Dominant Aerodynamics	15
2.4.2.1 Forces	16
2.4.2.2 Moments	21
2.5 Inertial Sensors	22

2.6	State Estimators	23
2.6.1	EKF Mechanization Equations	25
2.7	Observability	26
2.8	Quadrotor Simulator	29
2.8.1	Visual Simultaneous Localization And Mapping Simulator	32
2.9	Experimental set-up	32
2.10	Discussion	35
3	Model-Aided Inertial Estimators	36
3.1	Introduction	36
3.2	Related Work	37
3.3	Filter Design with Inertial Sensors	40
3.3.1	Conventional Attitude Estimators	41
3.3.2	Model-Aided Attitude and Velocity Estimator	42
3.4	Observability Analysis	46
3.5	Experiments	49
3.6	Discussion and Limitations	52
4	Model-Aided Visual Inertial Fusion	55
4.1	Introduction	55
4.2	Related Work	57
4.2.1	Vision Based Estimation	57
4.2.2	Visual-Inertial Fusion	59
4.2.3	Observability of Visual-Inertial Fusion	61
4.3	Visual-Inertial Fusion Filter Design	63
4.3.1	Conventional Visual Inertial Fusion	66
4.3.2	Model-Aided Visual Inertial Fusion	67
4.4	Observability of Visual-Inertial Fusion	69
4.4.1	Observability of C-VIF	69
4.4.2	Observability of MA-VIF	72
4.4.3	Discussion	76
4.5	Simulations of C-VIF and MA-VIF	77
4.5.1	Simulations with Consistent VSLAM Estimates	78
4.5.2	Simulations with VSLAM Errors	80
4.6	Experimental Evaluation of C-VIF and MA-VIF	82
4.6.1	VIF with Frequent VSLAM Estimates	83
4.6.2	VIF with Sparse VSLAM Updates	83
4.7	Tightly-Coupled MA-VIF	87
4.7.1	Estimation Results	88
4.8	Discussion and Limitations	89
5	Effects of and Estimating Wind	95
5.1	Introduction	95
5.2	Background and Related Work	96
5.3	Wind Model for Simulations	97

5.4	Effects of Wind on State Estimation	98
5.4.1	Inertial Estimators	99
5.4.2	Visual Inertial Estimators	100
5.5	Incorporating the Wind Effects in the Estimator	101
5.5.1	States, Process Model and Measurements	102
5.5.2	Observability Analysis of Wind Affected System	104
5.5.3	Unobservable Modes	107
5.5.4	Removing Unobservable Modes	108
5.5.5	Similarity between MA-VIF and wMA-VIF	109
5.6	Simulations of wMA-VIF	110
5.7	Experimental Evaluation of wMA-VIF	111
5.7.1	Results	114
5.8	Discussion and Limitations	118
6	Conclusions	121
6.1	Summary of Contributions	122
6.1.1	Quadrotor MAV Dynamic Model	122
6.1.2	Model-Aided Inertial Estimators	122
6.1.3	Model-Aided Visual-Inertial Fusion	122
6.1.4	Model-Aided State Estimation amidst Wind Disturbances	123
6.2	Discussion of Limitations	123
6.3	Future Work	125
Appendices		126
A Estimating the Propeller Drag Coefficient		127
B ID Monocular SLAM and Tightly-Coupled MA-VIF		129
B.1	Inverse-Depth monocular SLAM	129
B.2	Tightly-coupled Model-Aided Visual-Inertial Fusion	131
Bibliography		134

List of Figures

2.1	A typical quadrotor MAV	11
2.2	Motion Primitives for a quadrotor MAV	12
2.3	Coordinate frame definitions	13
2.4	A quadrotor in forward motion	18
2.5	Advancing and retreating blades of a propeller	19
2.6	Lift induced drag of an aerofoil	19
2.7	ARDrone Quadrotor used for experiments	33
2.8	Vicon motion capture setup.	34
2.9	Setup used for ARDrone experiments	35
3.1	3D flight path of the ARDrone experiment	50
3.2	MAVE attitude estimates of ARDrone	51
3.3	CAE attitude estimates of ARDrone	51
3.4	Attitude estimation errors of the MAVE and CAE	52
3.5	MAVE velocity estimates of ARDrone	52
3.6	CAE velocity estimates of ARDrone	53
3.7	Velocity estimation errors of the MAVE and CAE	53
4.1	Coordinate frame assignment for VIF	64
4.2	Structure of a loosely-coupled Visual-inertial fusion set-up	64
4.3	True position and velocity of C-VIF and MA-VIF simulations	78
4.4	2D projection of the VSLAM position estimates and ground truth for the first simulation	78
4.5	Velocity estimation errors of C-VIF and MA-VIF simulations	79
4.6	Scale estimates of C-VIF and MA-VIF simulations	79
4.7	VSLAM position estimates and 2D projection of C-VIF and MA-VIF estimates	80
4.8	Scale estimates of the C-VIF and MA-VIF simulation	81
4.9	2D projection of part of VSLAM position estimates used for ARDrone experiments	83
4.10	Position and velocity estimates of loosely-coupled MA-VIF experiments . .	84
4.11	Position estimation errors of the loosely-coupled MA-VIF and C-VIF experiments	85
4.12	Position and velocity estimation errors of the loosely-coupled MA-VIF and C-VIF experiments with 1Hz VSLAM	86
4.13	Structure of a tightly-coupled Visual-inertial fusion set-up	88

4.14	Tightly-coupled MA-VIF position estimates and errors	90
4.15	Tightly-coupled MA-VIF velocity estimates and errors	91
4.16	Tightly-coupled MA-VIF attitude estimates and errors	92
5.1	True inertial frame wind velocities used for simulations	98
5.2	Estimation errors of the MAVE from constant wind simulations	99
5.3	Estimation errors of the MAVE from wind gust simulations	100
5.4	Estimation errors of the MA-VIF from wind simulations	101
5.5	Estimation errors of the wMA-VIF from constant wind simulations	111
5.6	Estimation errors of MA-VIF and wMA-VIF for wind gust simulations . . .	112
5.7	True wind velocities and wind velocity estimation errors of wMA-VIF . .	113
5.8	Setup for wind disturbed experiments	113
5.9	Simulated VSLAM position and orientation measurements	114
5.10	Position estimates of wMA-VIF and MA-VIF for the wind disturbed experiments	115
5.11	Velocity estimates of wMA-VIF and MA-VIF for the wind disturbed experiments	116
5.12	Scale estimates for the wind disturbed experiments	117
5.13	Wind velocity estimates of the wMA-VIF	117
5.14	Velocity estimation errors of wMA-VIF and MA-VIF for the wind disturbed experiments	119
5.15	Accelerometer bias estimate of the wMA-VIF and MA-VIF	120

List of Tables

2.1	EKF Mechanization Equations	27
2.2	Parameters used in first simulator	30
2.3	Noise variances used in both simulators	32
3.1	Conventional Attitude Estimator	43
3.2	Model-Aided Attitude and Velocity Estimator - Initial Design	45
3.3	Model-Aided Attitude and Velocity Estimator - Final Design	49
4.1	VIF observability constraints	62
4.2	Conventional Visual-Inertial Fusion Estimator	67
4.3	Model-Aided Visual-Inertial Fusion Estimator	68
4.4	Performance of different VIF estimators	87
4.5	Performance comparison of LC and TC MA-VIF implementations	89
5.1	Model-Aided Visual-Inertial Fusion Estimator with Wind States	103
5.2	Modified Model-Aided Visual-Inertial Fusion Estimator with Wind States .	110
B.1	Tightly-Coupled Model-Aided Visual-Inertial Fusion Estimator	133

Abbreviations

BLDC	Brush-Less Direct Current
CAE	Conventional Attitude Estimator
C-VIF	Conventional Visual-Inertial Fusion
EKF	Extended Kalman Filter
GPS	Global Positioning System
ID	Inverse Depth
IMU	Inertial Measurement Unit
MAV	Micro Aerial Vehicle
MAVE	Model-aided Attitude and Velocity Estimator
MA-VIF	Model-Aided Visual-Inertial Fusion
MEMS	Micro-Electro-Mechanical Systems
NED	North, East, Down
PID	Proportional, Integrative, Derivative
PSD	Power Spectral Density
PTAM	Parallel Tracking And Mapping
RGB	Red, Green, Blue
RMS	Root-Mean-Square
SIFT	Scale-Invariant Feature Transform
VIF	Visual-Inertial Fusion
VSLAM	Visual Simultaneous Localization and Mapping
VTOL	Vertical Take-off and Landing
WGN	White Gaussian Noise
wMA-VIF	Wind incorporated Model-Aided Visual-Inertial Fusion

Nomenclature

General Formatting Style

$f(\cdot \cdot \cdot)$	A scalar valued function
$\mathbf{f}(\cdot \cdot \cdot)$	A vector valued function
$[\cdot]_x$	The x component of a vector
$[\cdot]_y$	The y component of a vector
$[\cdot]_z$	The z component of a vector
$B[\cdot]$	The frame of expression of a vector
$\dot{[\cdot]}$	The time derivative of a variable
$[\cdot]^T$	Transpose of a vector or a matrix
$\ \cdot\ $	The magnitude of a vector
$E[\cdot]$	The expectation of a random variable
$[\cdot](p, q)$	The $(p, q)^{th}$ element or block of a matrix
$[\cdot](p, :)$	The p^{th} row or row block of a matrix

Specific Symbol Usage

$\mathbf{0}_n$	$n \times n$ all zero matrix
$\{\mathbf{E}\}$	Earth fixed inertial coordinate frame
$\{\mathbf{B}\}$	Body coordinate frame
\mathbf{a}	A vector containing the measurement of accelerometer triad
${}^B_E R$	Rotation matrix to transform a vector from $\{\mathbf{B}\}$ to $\{\mathbf{E}\}$
c_Q	propeller torque coefficient
c_T	Lumped thrust coefficient
d	Distance from the centre of mass of the quadrotor to propeller hub

d_i	Induced drag coefficient
\bar{D}_L	Lumped parameter drag coefficient matrix
e_i	The i^{th} unit vector
\mathbf{F}	Sum of aerodynamic forces affecting the quadrotor MAV
f_T	The magnitude of the thrust vector
\mathbf{g}	Gravity vector
g	Magnitude of gravity vector
\mathbf{h}_{vp}	VSLAM position estimates
\mathbf{h}_{vo}	VSLAM orientation estimates
\mathbf{I}_n	$n \times n$ identity matrix
J	Inertia matrix of the quadrotor MAV
k_1	Lumped drag coefficient
\mathbf{M}	Sum of aerodynamic moments affecting the quadrotor MAV
m	Mass of the quadrotor MAV
M_i	i^{th} motor
\mathbf{p}	Position of the quadrotor MAV
r_p	The radius of a propeller
\mathbf{u}	Inputs to a dynamic system
\mathbf{v}	Velocity of the quadrotor MAV
\mathbf{v}_w	Velocity of the wind
\mathbf{v}_∞	Free stream velocity of the quadrotor MAV
\mathbf{X}	State of a dynamic system
\mathbf{x}_i	3D position of an environmental feature in $\{E\}$
\mathbf{y}	Measurements of a dynamic system
ϖ_i	Rotational rate of i^{th} propeller
Θ	Orientation of $\{B\}$ with respect to $\{E\}$
ϕ	Roll angle
θ	Pitch angle
ψ	Yaw angle
Ω	Instantaneous rotational rate of $\{B\}$ with respect to $\{E\}$
Ξ	Matrix that transforms instantaneous rotational rates to Euler rates

ω_g	A vector containing the measurement of gyroscope triad
β_g	Gyroscope bias
β_a	Accelerometer bias
η_g	Gyroscope measurement noise
$\eta_{\beta g}$	Gyroscope bias drift noise
η_a	Accelerometer measurement noise
$\eta_{\beta a}$	Accelerometer bias drift noise
η_q	Process noise
η_r	Measurement noise
η_v	Process noise of the quadrotor translational dynamics
η_p	Noise in VSLAM position estimates
η_o	Noise in VSLAM orientation estimates
η_λ	VSLAM scale drift noise
η_w	Wind velocity drift noise
Υ	A 2×3 matrix consisting of the first three rows of I_3
Γ	3×3 matrix of all zeros with the (3,3) element set to one.
λ	Scale of VSLAM estimates
Λ	3×3 Identity matrix with the (3,3) element set to zero

Glossary of Terms

Attitude	The combination of roll and pitch angles.
Consistent estimates	Estimates whose errors agree with the error covariance bounds predicted by the estimator.
Features	Distinctly identifiable points in an image of a 3D environment.
Free stream velocity	Velocity of an object with respect to the air stream around it.
Induced drag	A drag force that occurs due to the redirection of an air stream by a moving object.
Inertial Sensors	Sensors based on inertia. Common examples are accelerometers and gyroscopes.
Model-aided state estimation	Employing dynamic models and kinematic constants of a platform to aid the state estimation processes.
Monocular VS-LAM	VSLAM algorithms that only employs measurements from a RGB camera.
Multi-rotor	A category of aerial vehicles with three or more lift producing propellers.
Observability	The ability to uniquely determine the state of a dynamic system with a causal sequence of measurements.
Pitch	Second Euler angle caused by a rotation around body frame y axis.
Pose	The combination of position and orientation of an object in 3D space with respect to a reference coordinate frame.
Quadrotor	An aerial vehicle with four lift producing propellers.

Roll	Third Euler angle caused by a rotation around body frame x axis.
Scale	The ratio between the true and estimated map by a monocular VSLAM algorithm.
Visual-inertial fusion	The combination of information obtained from visual and inertial sensors to estimate states of interest.
Yaw	First Euler angle caused by a rotation around body frame z axis.

Chapter 1

Introduction

1.1 Micro Aerial Vehicles

Micro Aerial Vehicles (MAV) are a category of Unmanned Aerial Vehicles that typically weigh less than 10kg. There are three main categories of MAVs depending on how lift is produced. Fixed wing MAVs produce lift with the use of wings by continuous forward movement. Rotary wing MAVs employ one or more rotating propellers to produce lift. Lighter-than-air MAVs use buoyancy to float in the air.

Of the three, only the last two categories are capable of Vertical Take-Off and Landing (VTOL). However, rotary wing MAVs far surpass the lighter-than-air MAVs in terms of manoeuvrability and compactness. Fixed wing MAVs on the other hand require large areas for takeoff and landing and are not suitable for operating in confined environments such as indoors. They however have higher power-to-weight ratio due to their large wing span resulting in a larger operational area than their rotary wing counterparts.

Due to their manoeuvrability, compactness and VTOL capability, rotary wing MAVs are ideally suited to assist or replace humans in a host of tasks in urban and indoor environments that would otherwise be hazardous, tedious or expensive. Examples include infrastructure inspection, disaster and recovery services and aerial surveying. Even in remote places such as off-shore oil rigs, wind farms and power plants, rotary wing MAVs can

play an important role when inspection tasks need to be carried out in close proximity to structures.

1.1.1 Multi-rotor MAVs

There are two subcategories of rotary wing MAVs. The first category encompasses the traditional helicopter like platforms. The second category is known as multi-rotor MAVs and makes use of three or more propellers to generate thrust and manoeuvre the craft. This category consists of a variety of platform configurations based on a different number of propellers. Examples include tricopters [1], quadcopters or quadrotors [2], hexacopters [3] and octocopters.

Two main reasons motivate the use of multi-rotor MAVs instead of those based on the helicopter design, when the requirement is for a commercial platform that is portable and useful in close proximity to people and structures. Traditional helicopters employ a complex mechanism known as the “swashplate” to adjust the pitch of each propeller blade as they make a full revolution. This controls the attitude of the propeller plane and that, in turn, controls the aircraft attitude. Swashplates are susceptible to a high probability of failure due to the number of moving parts involved in its design and the speeds at which those parts operate. Small scale helicopters also use a “Bell-Hillier stabiliser” to slow the natural dynamic response of the rotor [4]. The complexity of these components means that helicopter MAVs are difficult and expensive to construct and are also prone to an increased risk of mechanical failures. Multi-rotor platforms on the other hand do not rely on such sophisticated mechanisms and are considerably easier to construct and are more robust to mechanical failures.

Also, multi-rotor MAVs are more compact than helicopters due to the reduced propeller diameters and closely spaced layout. By design, multi-rotors do not require tail rotors that protrude from the main body and thus can be easily enclosed in a protective hull to prevent the propellers from colliding with obstacles. This makes multi-rotor MAVs ideally suitable for operations in cluttered environments.

1.2 Motivation and Objectives

Out of the various manifestations of multi-rotors, quadrotors are the most popular due to the fact that they employ the smallest number of propellers in a symmetrical configuration. Most high level control and estimation algorithms developed for quadrotors can be readily applied to hexacopters and octocopters due to their symmetrical nature. Therefore, the discussion in this thesis focuses exclusively on quadrotor MAVs.

There are two main challenges that need to be overcome to realize the full potential of quadrotor MAVs in the field. First is the estimation of pose (position and orientation) of the quadrotor with respect to its environment. Second is the designing of suitable control and navigation algorithms which would employ these estimates to perform a given task safely and efficiently. It has been demonstrated that quadrotor MAVs can be made extremely manoeuvrable when fast and accurate state estimates are available from off-board pose estimation solutions such as a motion capture set-up[5], [6], [7]. Though such pose estimates can be obtained within lab environments, achieving the same task in the field is a difficult task because of the cost and complexity associated with these off-board pose estimation solutions. Outside the lab environments, it is critical to have a self contained set-up where all pose estimation and control tasks are performed on-board the MAV, so as to minimize the dependence on the availability of specific infrastructure and also to minimise the potential points of failures.

To fulfil the on-board state estimation task, mobile robots make use of state estimation algorithms which fuse information available from different sources to produce the best estimate of the variables that describe the state of the robot. Each source of information, when correctly utilized, will improve the estimation accuracy. Therefore, in the absence of other constraints such as Size, Weight, Power and Cost (SWaP-C), it is desirable to have as many information sources as possible incorporated into the state estimation algorithms.

The main information source for mobile robotic platforms are sensors that either observe the internal state of the platform (interoceptive) or its relationship with the external world (exteroceptive). Interoceptive sensors such as accelerometers, gyroscopes, inclinometers and exteroceptive sensors such as cameras, GPS, laser range finders are the commonly

available options for MAV state estimation. Out of these options, the most common configuration is a combination of GPS and inertial sensors [8], [9]. These sensors alone are, however, not suitable for operating in indoor and urban environments with close proximity to obstacles due to the limited accuracy of GPS in such environments¹.

In GPS-denied environments, information from laser range finders [11], depth cameras [12] or monocular cameras [13] can be combined with inertial sensors to design state estimators suitable for a mobile robot. There is however, another source of information that can be exploited to improve the accuracy of state estimators based on these sensors. This originates from the knowledge of the dynamic behaviour of the robot. Constraints or relationships between the states of the system can provide useful information about states that are not directly measured thus improving the accuracy of the estimation algorithm as a whole. The amount of information available though such constraints is inherently dependent on the nature of the constraint and as a result on the dynamics of the robotic platform being considered.

Most of the existing pose estimation algorithms for quadrotor MAVs rely on approximate motion models such as constant velocity model for state prediction. (The few exceptions to this design are discussed in Section 3.2). Such models were developed to be equally applicable to a variety of mobile robotic platforms and as a result do not encompass any platform specific behaviour that can be exploited as an information source to aid the state estimation. The accuracy and robustness of these state estimators can be improved if a suitable dynamic model of the quadrotor MAV is available.

Recent advances in modelling the behaviour of quadrotor MAVs has resulted in a dynamic model that is ideally suited as a source of information for the task of state estimation. In the right form, this dynamic model can be employed to improve the performance of quadrotor MAV state estimation algorithms that fuse the measurement of both interoceptive and exteroceptive sensors. However, the level of performance improvement and the conditions under which such an improvement is possible is not apparent and need to be thoroughly investigated.

¹With an unobstructed view of multiple satellites, civilian grade GPS can achieve a maximum accuracy of about 2m error in horizontal direction and 6m error in vertical direction [10]

The main objective of this thesis is to evaluate the utility of the quadrotor MAV dynamic model in GPS-denied state estimation in both indoor and outdoor environments. It incorporates the quadrotor MAV dynamic model into two state estimators; one based solely on interoceptive sensors and the other based on a combination of interoceptive and exteroceptive sensors. These sensors were chosen considering the SWaP-C constraints of quadrotor MAVs. Each of the two estimation scenarios are studied in detail with aim of identifying the benefits of model-aided state estimation and also the conditions under which those benefits can be obtained.

1.3 Contributions

This thesis presents four main contributions to the quadrotor MAV state estimation framework. First, a simplified formulation of the quadrotor MAV dynamic model that can be seamlessly integrated with the existing pose estimation algorithms is presented. This model can be employed to improve the estimation accuracy of most quadrotor MAV state estimators that make use of inertial sensors measurements. The underlying dynamics employed in deriving this model has been presented previously by other authors who have analysed the impact of propeller aerodynamics on the quadrotor MAV behaviour [14]. However, the adaptation of these equations into a dynamic model suitable for state estimation was first presented by the author in [15]. A detailed derivation of this model is presented here as the first contribution.

As the second contribution, this thesis illustrates how the formulated MAV dynamic model can be employed to design an improved state estimator using the measurements of a consumer grade Inertial measurement Unit (IMU). While there is a significant body of literature on employing dynamic or kinematic constraints to aid the state estimation of ground and fixed wing robotic platforms (see for example [16], [17], [18]), this is the first time such a model has been employed for multi-rotor MAV state estimation. This design was first presented by the author in [15],[19] and is included here as a key component of this contribution. Further, an analysis of the existing methodologies for MAV state estimation is presented to identify their shortcomings when compared to the proposed design. An observability analysis of the proposed design is also presented to illustrate

that the attitude of the quadrotor MAV and the lateral and longitudinal components of its body frame velocity are observable in contrast to the existing methods which can only provide attitude estimates. This analysis is complemented by experimental results which demonstrate that the proposed design can outperform the existing designs in real world conditions.

Inertial-only state estimators play a key role in MAVs because even the smallest MAVs are guaranteed to feature on-board IMUs. Any additional sensors may or may not be available depending on the SWaP-C constraints. Therefore, it is of importance to explore the possibility of improving the inertial-only state estimators before exploring other sensing modalities. However, there are several limitations to the inertial only state estimators, even with the improvements brought about by the incorporation of the quadrotor MAV dynamic model. These limitations can be overcome by introducing a monocular camera as an additional sensor into the state estimation process. The third main contribution of this thesis is to show how some of the limitations of the traditional methods of combining inertial and visual information can be overcome by incorporating the quadrotor MAV dynamic model in the sensor fusion algorithm. A rigorous non-linear observability analysis forms the backbone of this contribution. Based on the insights from the observability analysis, this thesis then proposes a state estimator that improves the accuracy and robustness of the existing designs while also reducing the computational resources required to process the sensor data.

The dynamic model of the quadrotor MAV is dependent on the ambient wind velocity incident on the MAV. This dependency can be neglected for operations in spacious indoor environments. However, when the quadrotor MAV is operating outdoors, the effects of wind needs to be explicitly modelled in the quadrotor dynamic model if it is to be employed to aid the state estimation. The fourth contribution of the thesis shows how the model-aided state estimation framework can be extended to incorporate the effects of wind. An observability analysis that identifies the observable states of the wind affected system and the underlying conditions on the MAV trajectory for ensuring the observability form an integral part of this contribution. Additionally, a state estimator design based on the insights gained through the observability analysis is proposed to simultaneously estimate the pose of the quadrotor MAV and the components of the wind velocity that affect it. Such

a state estimator would allow the quadrotor MAV to be safely and successfully deployed in outdoor environments or when it is required to operate in close proximity to structures and obstacles.

1.4 Thesis Outline

This thesis consists of five main chapters and two appendices. The second chapter presents the background material required for the design and analysis of the state estimators presented throughout the thesis. It discusses the quadrotor MAV dynamic model and derives a simplified form of the translational dynamics that is suitable to be incorporated into the state estimation algorithms. This chapter also presents details about the quadrotor MAV simulations and the experimental set-up with which the experimental data were gathered to verify the designed state estimators.

The third chapter considers the state estimation algorithms that only employ inertial sensors. It first analyses the existing inertial-only state estimators for quadrotor MAVs to identify the shortcomings of their designs. An improved design that employs the quadrotor MAV dynamics is presented next. The observability of this proposed design is analysed to identify and remove the unobservable modes. Experimental results that compare the state estimation accuracy of the proposed design with a design that captures the state-of-the-art in MAV state estimation are presented to highlight the merits of the former.

The fourth chapter identifies the limitations of the proposed inertial-only state estimator and introduces a monocular camera as an additional sensor to overcome these limitations. After identifying the unique challenges of designing a state estimator to fuse the visual and inertial data for a MAV, the details on two main methodologies that can be employed to design such an estimator are presented. This chapter then proposes a novel state estimator that combines the quadrotor MAV dynamic model with the visual and inertial sensor measurements. A state-of-the-art visual-inertial fusion estimator design is presented so that the performance of the proposed design can be benchmarked. A rigorous non-linear observability analysis as well as extensive simulation and experimental results are presented next to highlight the benefits of the proposed approach.

The fifth chapter considers the effect of wind disturbances on the model-aided state estimation for quadrotor MAVs. It first shows that the performance of the state estimators that are based on the quadrotor MAV dynamic model degrades with increasing wind disturbances. To overcome this issue, this chapter extends the model-aided state estimation framework to incorporate the effects of wind. An observability analysis is performed on the wind affected system to identify the observable modes and a theoretically sound strategy to remove the unobservable modes is presented next. Extensive simulations and experimental results are presented to show that this design is capable of simultaneously estimating both the pose of the quadrotor MAV and also the components of wind that affect the MAV.

Finally, chapter six concludes the thesis with a summary of the key findings and the contributions. It also points to several interesting future MAV research avenues that results from the model-aided state estimation framework presented in this thesis.

1.5 Publications

The work in this thesis has been previously presented in the following publications.

1. D. Abeywardena, S. Kodagoda, R. Munasinghe, and G. Dissanayake. A virtual odometer for a quadrotor micro aerial vehicle. In *Proc. Australasian Conference on Robotics and Automation (ACRA)*, Dec. 2011
2. D. Abeywardena, S. Kodagoda, G. Dissanayake, and R. Munasinghe. Improved state estimation in quadrotor MAVs: A novel drift-free velocity estimator. *IEEE Robotics Automation Magazine*, 20(4):32 – 39, Dec. 2013
3. D. Abeywardena, Z Wang, S. Kodagoda, and G. Dissanayake. Visual-inertial fusion for quadrotor Micro Air Vehicles with improved scale observability. In *Proc. IEEE International Conference on Robotics and Automation (ICRA)*, pages 3133 – 3138, May 2013
4. D. Abeywardena and G. Dissanayake. Tightly-coupled model aided visual-inertial fusion for quadrotor micro air vehicles. In *Field and Service Robotics*, volume 105 of *Springer Tracts in Advanced Robotics*, pages 153 – 166. Springer International Publishing, 2015
5. D. Abeywardena, Z Wang, G. Dissanayake, S. L. Waslander, and S. Kodagoda. Model-aided state estimation for quadrotor micro air vehicles amidst wind disturbances. In *Proc. IEEE/RSJ International Conference on Intelligent Robots and Systems (IROS)*, Sept. 2014
6. D. Abeywardena, Z Wang, S. Kodagoda, and G. Dissanayake. Model-aided visual-inertial fusion for quadrotor micro air vehicles with improved observability. *IEEE Transactions on Robotics*, under review

Chapter 2

Theoretical and Experimental Background

2.1 Introduction

This chapter presents the background material required for the design and analysis of the quadrotor MAV state estimation algorithms described throughout this thesis. It consists of two parts. The first part presents the theoretical background required for the design of state estimators for quadrotor MAVs. The second part details the methodologies that will be employed in analysing and evaluating the designed state estimations.

The first part begins by defining the states that need to be estimated and then describes the dynamics of a quadrotor MAV as a function of those states. It then details two types of inertial sensors and the characteristics of their measurements when mounted on-board a quadrotor MAV. A state estimation framework capable of fusing these and other sensor measurements with the quadrotor MAV dynamics is detailed next to conclude the first section.

This thesis employs three main methodologies to analyse the designed state estimators. The main theoretical tool employed for this purpose is the observability analysis. The second part of this chapter begins by detailing a differential geometry based non-linear observability analysis method commonly used to analyse state estimators in mobile robotics.

It then describes the quadrotor MAV simulator that will be used to further verify the observability results and also to analyse the performance of the state estimators under ideal conditions. Irrespective of how detailed they are, simulations alone are insufficient to validate novel state estimator designs. Real world experiments need to be performed and ground truth state estimates need to be obtained to critically analyse the accuracy, consistency and robustness of the estimator designs. The second part of this chapter concludes by detailing the experimental set-up used for this purpose.

2.2 Quadrotor MAVs, An Introduction

A quadrotor MAV consists of four fixed pitch propellers usually powered by an electric propulsion system (see Fig. 2.1). Brushless DC motors (BLDC) are commonly used as the propulsion system due to their high efficiency and reliability. The four propellers consists of two counter-rotating pairs arranged in a symmetrical cross configuration.



FIGURE 2.1: A typical quadrotor MAV. Shown on the side is the radio controller used for manual piloting.

Thrust produced by each propeller of the quadrotor MAV can be changed by varying its rotational speed. By changing the thrust of various propellers in different schemes, different flight patterns can be achieved. The four basic flight primitives, namely, rolling, pitching, yawing and thrusting are shown in Fig. 2.2. Pitching, rolling and thrusting respectively causes forward, sideways and vertical movement. Yawing causes a change in the heading angle of the MAV.

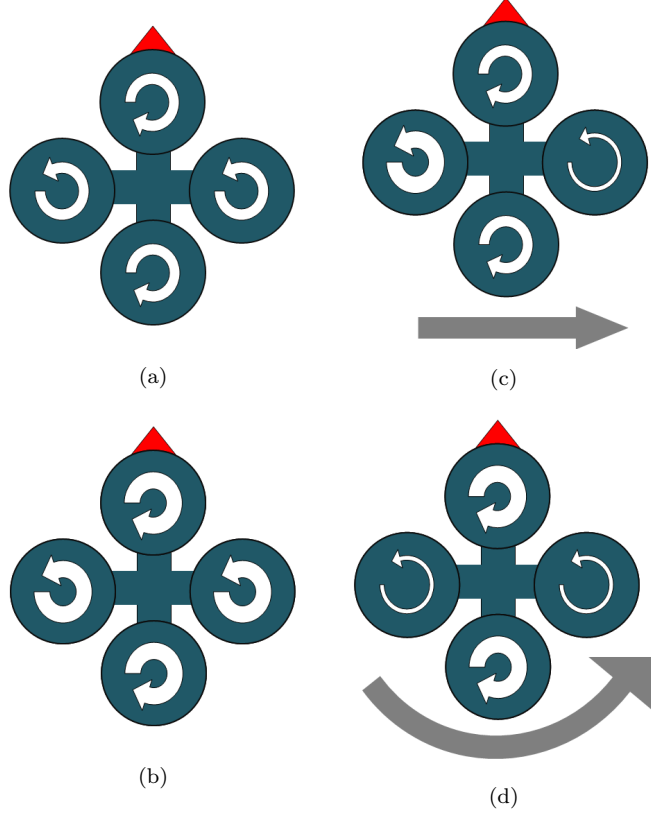


FIGURE 2.2: Motion Primitives for a quadrotor MAV. The width of the circular arrows indicate the propeller rotational rates. The red arrow on the top marks the forward direction. (a) - Hovering in place, (b) - moving up, (c) - Moving sideways by rolling, (c) - Yawing

2.3 Frame Definitions and States

The platform under consideration is a quadrotor MAV affixed with a suite of sensors. An earth fixed NED (North, East, Down) coordinate frame $\{E\}$ is defined and is also assumed to be an inertial frame given the typical range and flight time of a quadrotor MAV. Also a body fixed coordinate frame $\{B\}$ is defined with its origin at the centre of mass of the quadrotor MAV, with its ${}^Bx - {}^By$ plane aligned with the propeller plane, and Bx axis aligned along one arm of the MAV. (see Fig. 2.3) The quadrotor MAV is assumed to be symmetric around the Bz axis with four motors $M_i, i \in \{1, 2, 3, 4\}$ located at $[d \ 0 \ 0]$, $[0 \ d \ 0]$, $[-d \ 0 \ 0]$, $[0 \ -d \ 0]$ respectively, where d is the distance from the centre of mass of the quadrotor to the propeller hub. The Rotational rates of the propellers are denoted by $\varpi_i, i \in \{1, 2, 3, 4\}$. Without loss of generality, it is assumed that M_1 and M_3 are rotating counter-clockwise and M_2 and M_4 are rotating clockwise, when viewed from above.

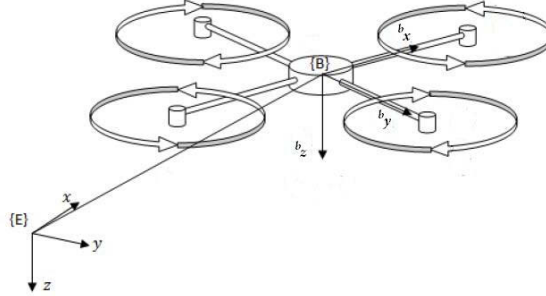


FIGURE 2.3: Quadrotor and the coordinate systems.

The position of the origin of $\{B\}$ with respect to $\{E\}$ is denoted by \mathbf{p} , the velocity of $\{B\}$ with respect to $\{E\}$ by \mathbf{v} , the orientation of $\{B\}$ with respect to $\{E\}$ expressed in Z-Y-X Euler angles by $\Theta = \{\phi, \theta, \psi\}$ and the rotational rate of $\{B\}$ with respect to $\{E\}$ by Ω . Thus the vector of states required to describe the motion of the quadrotor MAV is given by: $\mathbf{X} = [\mathbf{p} \ \mathbf{v} \ \Theta]^T$ ¹. The rotation matrix ${}^E_B R \in SO(3)$ transforms a vector in $\{B\}$ to $\{E\}$ and can be expressed in terms of $\{\phi, \theta, \psi\}$:

$${}^E_B R = \begin{bmatrix} c(\psi)c(\theta) & c(\psi)s(\phi)s(\theta) - c(\phi)s(\psi) & s(\phi)s(\psi) + c(\phi)c(\psi)s(\theta) \\ c(\theta)s(\psi) & c(\phi)c(\psi) + s(\phi)s(\psi)s(\theta) & c(\phi)s(\psi)s(\theta) - c(\psi)s(\phi) \\ -s(\theta) & c(\theta)s(\phi) & c(\phi)c(\theta) \end{bmatrix} \quad (2.1)$$

where s and c are shorthand forms for sin and cosine, respectively. Also Ξ denotes the matrix that relates angular velocity ${}^B \Omega$ to the Euler rates:

$$\dot{\Theta} = \Xi {}^B \Omega \quad (2.2)$$

$$\Xi = \begin{bmatrix} 1 & t(\theta)s(\phi) & t(\theta)c(\phi) \\ 0 & c(\phi) & -s(\phi) \\ 0 & s(\phi)/c(\theta) & c(\phi)/c(\theta) \end{bmatrix} \quad (2.3)$$

where t is the shorthand form for tangent. In the aerodynamics literature, ϕ, θ, ψ angles are referred to as roll, pitch and yaw, respectively. It is also common to refer to the combination of roll and pitch angles as the attitude and the yaw angle as the heading. The same conventions are adhered to in this thesis.

¹This state vector will be augmented later with other parameters related to sensors measurements

Besides Euler angles, there are several other parametrizations that can be used to represent the orientation of an object with respect to a given coordinate frame. At a minimum, three parameters are required to represent the orientation. However, all three-parameter orientation representations are singular [24]. These singularities can be avoided by employing higher-dimensional parametrizations such as the quaternion or rotation matrix. However, elements in these over-parametrised representations have additional constraints that need to be maintained to ensure that they represent a valid orientation. Such constraints increase the complexity of state estimators that employ over-parametrised orientation representations. On the other hand, the singularities of Euler angle parametrization occur when either the roll or the pitch angle is equal to $\pi/2$ and can be easily avoided in the normal operations of a quadrotor MAV. Therefore, in this thesis the Euler angle parametrization will be used to represent the orientation of the quadrotor MAV with respect to the inertial coordinate frame.

2.4 Dynamics of a Quadrotor MAV

2.4.1 Rigid Body Dynamics

The rigid body dynamics of a quadrotor MAV in motion are governed by the Newton-Euler equations:

$${}^E\dot{\boldsymbol{p}} = {}^E\boldsymbol{v} \quad (2.4a)$$

$${}^E\dot{\boldsymbol{v}} = \boldsymbol{g} + \frac{1}{m} {}^B_R {}^B\boldsymbol{F} \quad (2.4b)$$

$${}^B\dot{\boldsymbol{\Omega}} = J^{-1}({}^B\boldsymbol{M} - {}^B\boldsymbol{\Omega} \times J {}^B\boldsymbol{\Omega}) \quad (2.4c)$$

$$\dot{\boldsymbol{\Theta}} = \boldsymbol{\Xi} {}^B\boldsymbol{\Omega} \quad (2.4d)$$

where $\boldsymbol{g} = g\mathbf{e}_3$ is the gravity vector in $\{E\}$ with $\mathbf{e}_3 = [0 \ 0 \ 1]^T$ and $g = \|\boldsymbol{g}\|$, m is the mass of the quadrotor, \boldsymbol{F} , \boldsymbol{M} are respectively the sum of aerodynamic forces and moments acting on the quadrotor and J is the constant inertia matrix of the vehicle expressed in

$\{B\}$. For a typical quadrotor MAV, J is a diagonal matrix of the form:

$$J = \begin{bmatrix} J_{xx} & 0 & 0 \\ 0 & J_{yy} & 0 \\ 0 & 0 & J_{zz} \end{bmatrix} \quad (2.5)$$

where J_{xx} , J_{yy} , J_{zz} are positive constants. Also, due to the symmetric design of the quadrotor MAV, it is reasonable to assume that $J_{xx} \approx J_{yy}$.

2.4.2 Dominant Aerodynamics

This section derives the expressions for the aerodynamic forces and moments, \mathbf{F} , \mathbf{M} . Much of the work in the early quadrotor MAV literature assumes that the thrust produced by the propeller is the only dominant aerodynamic force affecting the motion of the MAV and that this thrust is always vertical to the rotor hub. (see for example [25], and [2]). However, when a rotor translates laterally through the air, it displays an effect known as blading flapping, which results in a tilt in the resultant thrust vector. Blade flapping plays an important role in the dynamics of full-scale helicopters due to the semi-rigidity of their propellers. The dynamic equations that model blade flapping are well known in the helicopter community [26]. The X-4 flyer platform developed by Pounds et al. [27] incorporated teetering rotor hubs that allow for adjustment of the blade flapping characteristics to improve the quadrotor MAV stability. To account for the blade flapping, they extended the MAV dynamic model by including the forces and moments due to blade flapping. Pounds [4] adjusted the classical blade flapping model so that it is more suitable for small scale rotary wing platforms and presented a detailed derivation of the various secondary aerodynamic effects that affect such vehicles including flapping due to rolling, pitching, yawing and also inflow damping. However, later work on quadrotor MAV dynamic modelling assumed that the blade flapping does not play a critical role in the dynamic behaviour of quadrotor MAVs constructed with unhinged, semi-rigid, fixed pitch propellers [28],[29].

Huang et al. [30] acknowledged that there are additional secondary aerodynamic effects that make the true behaviour of a quadrotor MAV with fixed pitch propellers different

from that obtained using ideal models, even when the rotor blades were unhinged to restrict flapping motion. As pointed out by Pounds [4], this was due to the flexibility of the semi-rigid propellers and the considerable forces that small propeller blades encounter during lateral motion of the propeller ([4], section 5.2). Huang et al. [30], however, chose to employ controllers to compensate for these effects rather than to incorporate them in the quadrotor MAV dynamic model. Martin and Salaun [14] also presented a derivation of the some of secondary aerodynamic forces and moments affecting a typical quadrotor MAV in near hover flight. They also showed that these dynamics can be combined with the measurement equations of on-board accelerometers to derive a biased estimate of the quadrotor MAV velocity. A more recent investigation by Mahony et al. [31] presented a simplified form of the quadrotor MAV flapping equations and also incorporated the effects of induced drag into the model. They neglected the effects of flapping due to roll, pitch, yaw motions and also the effects of inflow damping, as those effects only have a transient impact on the motion of the quadrotor MAV during pitching, rolling or yawing motions. The development below is based on their model as experiments with several quadrotor MAV platforms have indicated that this simplified model serves well for the task of quadrotor MAV state estimation [15] [32]. The notation used in this thesis follows that from Mahony et al. [31].

2.4.2.1 Forces

For a quadrotor MAV in hover condition, \mathbf{F} consists only of the hover thrust f_T , which by design is perpendicular to the propeller plane².

$$\mathbf{F} = f_T {}^B \mathbf{z} \quad (2.6)$$

$$= c_T \sum_{i=1}^4 \varpi_i^2 {}^B \mathbf{z} \quad (2.7)$$

²Some quadrotor MAV designs have their thrusters tilted slightly inwards. However, since this tilt is the same for each thruster, the horizontal thrust component of each propeller due to this tilt is cancelled by that of the opposing propeller. Any residual horizontal thrust component arising from this tilt due to propeller speed differences are assumed negligible in this thesis.

where c_T is a positive coefficient. However, when the quadrotor is in motion, secondary aerodynamic forces that change both the direction and magnitude of hover thrust are induced. A detailed description of all these forces was presented by Pounds [4].

A comprehensive dynamic model that incorporates all such forces may become necessary when performing a mathematical simulation of a quadrotor MAV. However, when designing a dynamic model that can be employed to aid the state estimation of real systems, the main requirement is to mathematically capture the effects of the dominant forces in a manner that would satisfactorily explain the dynamics of a quadrotor MAV in-flight. Therefore, the following exposition makes use of several assumptions about the behaviour and operating conditions of the quadrotor MAV as employed by Mahony et al. [31] and Martin and Salaun [14] in deriving the quadrotor MAV dynamic model.

To keep the resulting mathematical models tractable, Mahony et al. [31] made the assumption that the quadrotor MAV is operating in near hover conditions with small \mathbf{v} and $\boldsymbol{\Omega}$ when compared to the propeller tip velocities of the MAV. Propeller tip velocities is in the range of a few tens of meters per second for typical quadrotor MAVs³ and therefore translational velocities up to about $5ms^{-1}$ can be considered small [14]. They also suggested that for near hover conditions, only those forces due to blade flapping and induced drag are of significance.

Blade flapping is caused by the aerodynamic moments of a semi-rigid propeller moving with respect to the surrounding air mass. Consider the case illustrated in Fig. 2.4 which illustrates a quadrotor MAV moving right with a non-zero velocity. For a propeller with two blades, it is possible identify a retreating and an advancing blade, as shown in blue and green respectively in Fig. 2.5. The velocity of the advancing blade with respect to air is higher than that of the retreating blade, due to the translational velocity of the whole quadrotor. This increased velocity causes the advancing blade to produce more thrust than the retreating blade, creating a force imbalance between the two blades of the same propeller. This force imbalance causes the advancing blade to flap up, decreases the angle of attack of the advancing blade thus decreasing the thrust produced and vice-versa for the retreating blade. If the blades are hinged at the rotor hub, the flapping stabilizes at

³The propeller tip velocity is about $35ms^{-1}$ for the ARDrone quadrotor MAV described in Section 2.9

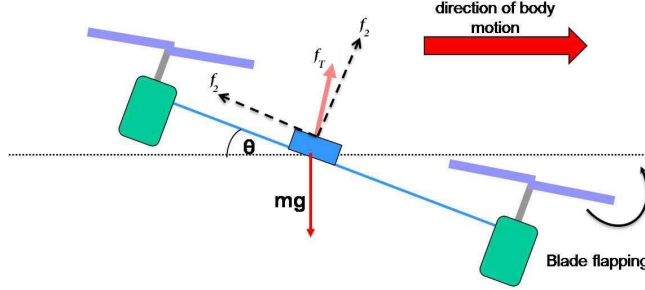


FIGURE 2.4: A quadrotor in forward motion. The thrust force f_T tilts as a result of the no-zero apparent wind as seen by the propeller. f_1 and f_2 are the orthogonal components of f_T

an angle such that the increase (decrease) of thrust due to the translational velocity of the quadrotor is matched with the thrust decrease (increase) due to the change in angle of attack of the advancing (retreating) blade. The net effect of blade flapping causes both blades to produce the same amount of lift. However, blade flapping also causes the thrust force of the propeller as a whole to be tilted in a direction which opposes the motion of the quadrotor. Assuming small flapping angles, the thrust force in $\{B\}$ can be modelled as:

$${}^B \mathbf{F} \approx f_T \mathbf{e}_3 - f_T A_{flap} {}^B \mathbf{v}_\infty \quad (2.8)$$

with

$$A_{flap} = \frac{1}{\varpi r_p} \begin{bmatrix} A_{1c} & -A_{1s} & 0 \\ A_{1s} & -A_{1c} & 0 \\ 0 & 0 & 0 \end{bmatrix}$$

where ϖ is the nominal propeller rotational rate at hover, r_p is the propeller radius, A_{1c}, A_{1s} are positive constants [31]. Also $\mathbf{e}_3 = [0 \ 0 \ 1]^T$ and \mathbf{v}_∞ is the velocity of the quadrotor with respect to air given by:

$${}^B \mathbf{v}_\infty = {}^B \mathbf{v} - {}^B \mathbf{v}_w$$

where \mathbf{v}_w is the wind velocity.

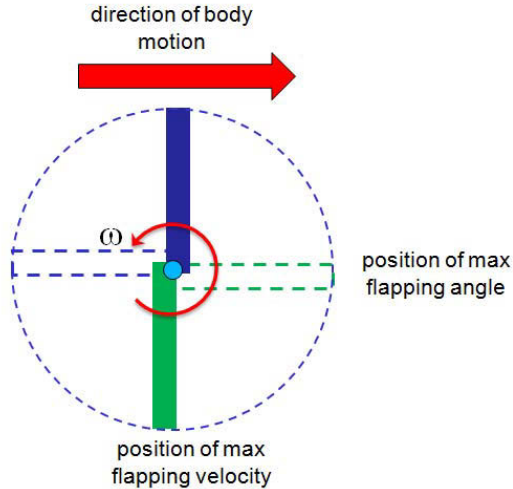


FIGURE 2.5: Advancing (green) and retreating (blue) blades of a propeller. As the propeller blades rotate, flapping is determined by their position with respect to the direction of motion of the propeller as a whole.

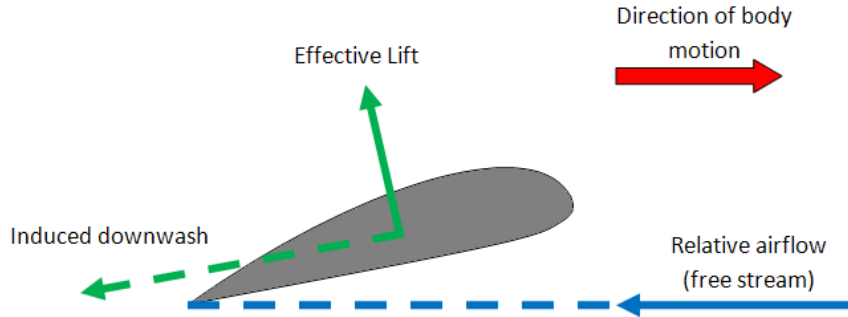


FIGURE 2.6: A cross section of the advancing blade showing the backward inclination of lift with respect to aerofoil. The aerofoil of the blade causes the downwash of air in the vicinity of the blade to be inclined downward with respect to the free stream. The lift produced is perpendicular to the downwash, and thus is tilted backward with respect to the aerofoil.

If, however, the blades are not hinged, as is the case for fixed pitch propellers employed in typical quadrotor MAVs, then the stiffness of the propeller creates a resistance to flapping. As a result, the flapping angle reduces and this causes the advancing blade to produce more lift than the retreating blade. The more rigid the propeller is, the less the blades will flap resulting in a larger thrust difference between the advancing and retreating blades. For

any aerofoil that generates lift, there is an associated induced drag due to the backward inclination of the aerodynamic force with respect to the aerofoil (see Fig. 2.6). The induced drag is proportional to the total aerodynamic force acting on the aerofoil and thus to the lift generated from the aerofoil. As the advancing blade of a quadrotor MAV propeller produces more lift than the retreating blade, it produces more induced drag, resulting in a net drag force that opposes the direction of the apparent wind. The induced drag in $\{B\}$ can be approximately modelled as:

$${}^B \mathbf{F}_{id} \approx -f_T D_{id} {}^B \mathbf{v}_\infty \quad (2.9)$$

with

$$D_{id} = \begin{bmatrix} d_i & 0 & 0 \\ 0 & d_i & 0 \\ 0 & 0 & 0 \end{bmatrix}$$

where d_i is the induced drag coefficient [31].

Blade flapping and induced drag are simultaneous effects. The total aerodynamic force affecting the quadrotor is the sum of the thrust, blade flapping effects and induced drag forces:

$${}^B \mathbf{F} \approx f_T \mathbf{e}_3 - f_T D_L {}^B \mathbf{v}_\infty \quad (2.10)$$

where $D_L = A_{flap} + D_{id}$. In practice, the propellers of quadrotor MAVs are small and are relatively more rigid than those of helicopters, resulting in small flapping angles. This has the net effect of decreasing the thrust deviations due to blade flapping and increasing induced drag components. That in-turn causes the terms due to induced drag to dominate the elements in D_L [33]. Therefore, it can be assumed that $D_L \approx D_{id}$. Also, it is reasonable to assume that the total thrust of a quadrotor MAV near hovering is approximately a constant. Thus, $\frac{1}{m} f_T D_L$ can be considered as a constant lumped parameter matrix. These assumptions result in:

$${}^B \mathbf{F} \approx f_T \mathbf{e}_3 - \bar{D}_L {}^B \mathbf{v}_\infty \quad (2.11)$$

where:

$$\bar{D}_L = \begin{bmatrix} k_1 & 0 & 0 \\ 0 & k_1 & 0 \\ 0 & 0 & 0 \end{bmatrix} = \begin{bmatrix} \frac{f_T d_i}{m} & 0 & 0 \\ 0 & \frac{f_T d_i}{m} & 0 \\ 0 & 0 & 0 \end{bmatrix}$$

and k_1 is a constant parameter that has to be determined through an one-time, off-line process using the quadrotor dynamic equations and ground truth state estimates. Details on estimating k_1 can be found in Appendix A.

It is now possible to re-write the translational dynamics of the quadrotor MAV using Equations (2.4b) and (2.10).

$${}^E\dot{\boldsymbol{v}} \approx \boldsymbol{g} + \frac{1}{m} {}^B_R(\boldsymbol{f}_T \boldsymbol{e}_3 - \bar{D}_L {}^B\boldsymbol{v}_\infty) \quad (2.12)$$

2.4.2.2 Moments

Moments affecting the quadrotor MAV body are mainly caused by the lift generated by each individual propeller. Assuming small flapping angles, this moment can be modelled as:

$${}^B\boldsymbol{M} = \begin{bmatrix} 0 & -dc_T & 0 & dc_T \\ -dc_T & 0 & dc_T & 0 \\ c_Q & -c_Q & c_Q & -c_Q \end{bmatrix} \begin{bmatrix} \varpi_1^2 \\ \varpi_2^2 \\ \varpi_3^2 \\ \varpi_4^2 \end{bmatrix} \quad (2.13)$$

where c_Q is a positive coefficient. If the propeller plane is vertically displaced from the centre of mass of the quadrotor, then induced drag will cause a moment as well. However, here it is assumed that, by design, the vertical displacement of the propeller plane is small. Thus it is possible neglect the moments due to propeller drag forces.

Additionally, the spinning propellers create gyroscopic moments that act on the MAV body during roll and pitch rotations of the MAV. However, the counter-rotating propeller pairs result in a cancellation of the positive and negative gyroscopic moments around both

pitch and roll axes. Any residual gyroscopic moment due to differences in rotational rates of the propeller pairs are assumed to be negligible.

2.5 Inertial Sensors

Consider a quadrotor MAV affixed with an Inertial Measurement Unit (IMU) consisting of a triad of accelerometers and gyroscopes. To simplify the ensuing analysis, it is assumed that the accelerometers and gyroscope triads are aligned with $\{B\}$ and also that the accelerometers are mounted at the centre of mass of the quadrotor MAV. Note that it is relatively easy to align the inertial sensors with $\{B\}$ and to position the accelerometers along the body vertical axis Bz , due to the symmetric vehicle design. Nevertheless, in practise a small displacement from this ideal arrangement is inevitable. In the design of state estimators, these misalignments will be taken into account by adding suitable noise terms to the expected sensor measurements.

MAVs typically use consumer grade microelectromechanical systems (MEMS) inertial sensors due to their low cost and small size. Measurements of MEMS inertial sensors are corrupted by various deterministic and random errors sources. The state estimation algorithms need to account for these measurement errors by employing approximate models that describe the main characteristics of their sources. Standard MEMS noise models consists of a slowly varying bias and a zero-mean white Gaussian noise term [34], [35].

Gyroscopes measure the instantaneous rotational rate of a body with respect to the inertial frame. Their measurements can be modelled independently of the equations of motion of the moving platform to which they are attached:

$${}^B\boldsymbol{\omega}_g = \boldsymbol{\Omega} + \boldsymbol{\beta}_g + \boldsymbol{\eta}_g \quad (2.14a)$$

$$\dot{\boldsymbol{\beta}}_g = \boldsymbol{\eta}_{\beta g} \quad (2.14b)$$

where ${}^B\boldsymbol{\omega}_g$ is the measurement of a body mounted triad of gyroscopes, $\boldsymbol{\beta}_g$ is a 3×1 vector of gyroscope biases, and $\boldsymbol{\eta}_g, \boldsymbol{\eta}_{\beta g}$ are both 3×1 vectors of zero mean White Gaussian Noise (WGN) variables.

Accelerometers measure a combination of inertial and gravitational acceleration:

$${}^B\boldsymbol{a} = {}^B_R({}^E\dot{\boldsymbol{v}} - \boldsymbol{g}) + \boldsymbol{\beta}_a + \boldsymbol{\eta}_a \quad (2.15a)$$

$$\dot{\boldsymbol{\beta}}_a = \boldsymbol{\eta}_{\beta a} \quad (2.15b)$$

where ${}^B\boldsymbol{a}$ is the measurement of a body mounted triad of accelerometers, ${}^B_R = {}^E_R T$ is the rotation matrix that transforms a vector from $\{E\}$ to $\{B\}$, $\boldsymbol{\beta}_a$ is a 3×1 vector of accelerometers biases, and $\boldsymbol{\eta}_a, \boldsymbol{\eta}_{\beta a}$ are both 3×1 vectors of zero mean White Gaussian Noise (WGN) terms. The accelerometer measurement model of Equation (2.15a) can be combined with the quadrotor MAV translational dynamics in Equations (2.12) to obtain:

$${}^B\boldsymbol{a} = \frac{f_T}{m}\boldsymbol{e}_3 - \bar{D}_L {}^B\boldsymbol{v}_\infty + \boldsymbol{\beta}_a + \boldsymbol{\eta}_a \quad (2.16)$$

Equation (2.16) indicates that the accelerometers along the ${}^B\boldsymbol{x}, {}^B\boldsymbol{y}$, directions of the quadrotor MAV are not affected either by gravity or by the propeller thrust. Intuitively, the absence of gravity in Equation (2.16) can be explained by the fact that the ${}^B\boldsymbol{x}, {}^B\boldsymbol{y}$, accelerometers are effectively free falling under the effect of gravity⁴. These two accelerometers are only affected by a force that is linearly proportional to the free stream velocity ${}^B\boldsymbol{v}_\infty$ of the quadrotor MAV. As \bar{D}_L is approximately a constant diagonal matrix with a zero in the (3,3) entry, it can be seen that a biased and noisy measurement of the ${}^B\boldsymbol{x}, {}^B\boldsymbol{y}$, components of the quadrotor MAV velocity can be obtained from an on-board accelerometer. This key insight was first reported by Martin and Salaun [14] and will be used in later chapters of this thesis to improve the accuracy of quadrotor MAV state estimators.

2.6 State Estimators

The task of a state estimator is to produce an optimal current estimate of the system states, given all the past measurements. A state estimator usually makes use of process and measurement models to achieve this task. Process models describe the dynamic and kinematic

⁴A free falling accelerometer, irrespective of its orientation, registers a zero measurement in the absence of error sources such as bias.

relationships between the states themselves. Measurement models describe the relationships between the states and measurements. In reality the measurements are corrupted by various noise sources and the process and measurement models are often tractable approximations of the true relationships. One way to cope with these uncertainties is to produce an estimate of the probability density function that describes the likelihood of the state estimate given all past measurements instead of attempting to estimate the state itself.

The Kalman Filter [36] is one such state estimation algorithm that aims to minimise the mean-squared estimation error. It is based on the assumption that all noise sources can be modelled as linear transformations of unbiased Gaussian random variables. If the process and measurement equations are linear with respect to the state variables and if the noise sources adhere to the above assumption, it can be easily shown that the resulting state estimates should also be jointly-Gaussian distributed. The Kalman filter provides a direct way of estimating this resulting probability distribution function of the estimates, given the statistical models of process and measurement equations ([37], chapter 4-5).

However, in practise, process and measurement equations are rarely linear. Extended Kalman filter (EKF) aims to apply the principles of linear Kalman filtering to non-linear problems by linearising the process and measurement equations around nominal state trajectories. Though the resulting estimates will not, in general, be optimal, EKF is known to produce acceptable estimates in many practical problems ([37], chapter 12).

All estimation algorithms designed and analysed in this thesis are based on the Kalman filter. Specifically, all state estimation algorithms were implemented as EKFs. The more complex variations of Kalman filter implementations such as unscented Kalman filters [38] may provide better results but were avoided in this thesis because EKF has been shown to perform satisfactorily in estimation problems with similar non-linearities as those discussed in the proceeding chapters⁵. However, the observability analysis performed on the designed state estimators would be equally applicable to all variations of the Kalman filter. Other forms of non-linear estimation algorithms such as non-linear complementary filters [39] do exist but their design is not straightforward and the analysis becomes difficult for all but the simplest estimation problems.

⁵More details included in the Related Work section of each chapter

An excellent introduction to Kalman filters including the practical considerations of implementing an EKF can be found in [37]. The remainder of this section only presents the core equations of the standard EKF formulation. These equations remain the same for all state estimators presented in later chapters of this thesis except for the process and measurement equations they employ. Therefore, for each of the proposed estimator designs, only the respective process and measurement equations will be presented in the subsequent chapters.

2.6.1 EKF Mechanization Equations

Assume that a non-linear system is described by the process and measurement equations given by:

$$\dot{\mathbf{X}} = \mathbf{f}(\mathbf{X}, \mathbf{u}, \boldsymbol{\eta}_q)$$

$$\mathbf{y} = \mathbf{h}(\mathbf{X}, \boldsymbol{\eta}_r)$$

where \mathbf{X} is the state vector, \mathbf{u} is the inputs to the system and $\boldsymbol{\eta}_q, \boldsymbol{\eta}_r$ are WGN terms accounting for the errors in process and measurement models. An EKF follows a two stage process consisting of state prediction and correction. For the estimators presented here, state prediction is performed by 2nd order Runge-Kutta integration of the process equations given by:

$$\mathbf{X}_k^- = \mathbf{X}_{k-1} + 1/2T_s[\mathbf{f}_{k-1} + \mathbf{f}_k]$$

$$\text{where } \mathbf{f}_{k-1} = \mathbf{f}(\mathbf{X}_{k-1}, \mathbf{u}_{k-1})$$

$$\mathbf{f}_k = \mathbf{f}(\mathbf{X}_{k-1} + T_s \mathbf{f}_{k-1}, \mathbf{u}_k).$$

Covariance prediction is performed by:

$$\begin{aligned}
 P_k^- &= F_k P_{k-1} F_k^T + G_k Q_k G_k^T \\
 \text{where } F(t) &= \frac{\partial f(\mathbf{X}, \mathbf{u}, \boldsymbol{\eta}_q)}{\partial \mathbf{X}} \Big|_{\mathbf{X}(t), \mathbf{u}(t), \mathbf{0}} \\
 G(t) &= \frac{\partial f(\mathbf{X}, \mathbf{u}, \boldsymbol{\eta}_q)}{\partial \boldsymbol{\eta}_q} \Big|_{\mathbf{X}(t), \mathbf{u}(t), \mathbf{0}} \\
 Q(t) &= E[\boldsymbol{\eta}_q \boldsymbol{\eta}_q^T]
 \end{aligned}$$

and F_k , G_k , Q_k are the discretized versions of $F(t)$, $G(t)$, Q respectively, with a time step of T_s . $E[\cdot]$ denotes the expectation operator. The value of elements in the resulting process covariance noise matrix Q need to be chosen after considering the magnitude of possible deviations of the process dynamics of each system and further fine tuned for optimal filter performance. State and covariance updates are performed according to:

$$\begin{aligned}
 K_k &= P_k^- H_k^T (H_k P_k^- H_k^T + R)^{-1} \\
 \mathbf{X}_k &= \mathbf{X}_k^- + K_k (\mathbf{y}_k - h(\mathbf{X}_k, \mathbf{0})) \\
 P_k &= (I - K_k H_k) P_k^-
 \end{aligned}$$

where H_k , R_k are the discretized versions of $H(t)$, $R(t)$ given by:

$$\begin{aligned}
 H(t) &= \frac{\partial h(\mathbf{X}, \boldsymbol{\eta}_r)}{\partial \mathbf{X}} \Big|_{\hat{\mathbf{X}}(t), \mathbf{0}} \\
 R(t) &= E[\boldsymbol{\eta}_r \boldsymbol{\eta}_r^T]
 \end{aligned}$$

respectively. Also, \mathbf{y}_k combines all measurements obtained at time step k . A summary of EKF prediction and update equations are presented in Table 2.1.

2.7 Observability

Observability of the underlying system of process and measurement equations is a necessary condition for any state estimator based on the Kalman filter to perform as expected. A system is observable if and only if its state at any given time can be uniquely determined

TABLE 2.1: EKF Mechanization Equations

Prediction	Update
	Kalman gain
State prediction $\mathbf{X}_k^- = \mathbf{X}_{k-1} + 1/2T_s[\mathbf{f}_{k-1} + \mathbf{f}_k]$	$K_k = P_k^- H_k^T (H_k P_k^- H_k^T + R)^{-1}$
Covariance prediction $P_k^- = F_k P_{k-1} F_k^T + G_k Q_k G_k^T$	State update $\mathbf{X}_k = \mathbf{X}_k^- + K_k (\mathbf{y}_k - h(\mathbf{X}_k, \mathbf{0}))$
	Covariance update $P_k = (I - K_k H_k) P_k^-$

given a finite sequence of measurements. The measurements from an unobservable system would not contain sufficient information for an accurate reconstruction of the state at a given time. For complex systems involving many different state variables, the observability properties are usually not apparent. Therefore, it is essential to examine the observability of such complex systems prior to designing state estimators for them.

The observability properties of linear time-invariant systems can be analysed by employing the well known rank test of the Gramian matrix [37]. However, the systems under consideration in this thesis comprises of non-linear process and measurement equations, precluding the use of these linear observability analysis tools. Hermann and Krener [40] presented a method for analysing the observability properties of non-linear systems based on differential geometry. They proposed a rank condition test for “locally weak observability” of a non-linear system: *a system is locally weakly observable if it satisfies the observability rank condition generically* [40]. A system described by a process equation of the form⁶ $\dot{\mathbf{X}} = f_0(\mathbf{X}) + \sum f_i(\mathbf{X})u_i, i = 1 \dots l$, and a measurement equation of the form $\mathbf{y} = \mathbf{h}(\mathbf{X})$ satisfies the observability rank condition if any one of the possible matrices whose rows are of the form:

$$\mathcal{O} = \{\nabla L_{f_i \dots f_j}^n h_k(\mathbf{X}) | i, j = 0, \dots, l; k = 1, \dots, m; n \in \mathbb{N}\}$$

is of full column rank. Here m is the number of measurements and $h_k(\mathbf{X})$ is the k^{th} measurement. Also, $\nabla L_{f_i}^n h_k(\mathbf{X})$ is the gradient of the n^{th} order Lie derivatives of $h_k(\mathbf{X})$

⁶This is also known as the input linear form as the process equation is linear with respect to the inputs.

with respect to f_i and can be calculated iteratively as:

$$\begin{aligned}\nabla L_f^0 h_k &= \frac{\partial h_k}{\partial \mathbf{X}} \\ \nabla L_{f_i}^n h_k &= \nabla L_{f_i}^{n-1} h_k \frac{\partial f_i}{\partial \mathbf{X}} + \left[\frac{\partial (\nabla L_{f_i}^{n-1} h_k)^T}{\partial \mathbf{X}} f_i \right]^T\end{aligned}$$

where h_k represents $h_k(\mathbf{X})$ and f_i represents $f_i(\mathbf{X})$.

Locally weak observability is a necessary condition but not sufficient for strict observability. However, following the approach by Kelly and Sukhatme [38], Martinelli [41], Mirzaei and Roumeliotis [42] and many others, in this thesis it is assumed that for most mobile robotic navigational tasks, locally weak observability implies that the considered system contains enough information to perform state estimation. Simulation and experimental results are also presented in chapters 4 and 5 to further validate the claims made based on this assumption.

If the observability matrix \mathcal{O} is rank deficient, then one or more of the states are not observable. However, it may be possible to remove the unobservable states so that the estimates of the observable states can be made. Thus, a method to identify the unobservable states is required. Martinelli [41] introduced a method for identifying the unobservable modes using the null space of \mathcal{O} .

PROPERTY 1: $g(\mathbf{X})$ is an observable mode if and only if its gradient is orthogonal to the null space of \mathcal{O} . This property can be expressed by a system of partial differential equations:

$$\sum_{i=1}^n w_{si}(\mathbf{X}) \frac{\partial g(\mathbf{X})}{\partial \mathbf{X}_i} = 0 \quad (2.17)$$

where n is the dimension of \mathbf{X} , $w_s(\mathbf{X})$ is a non-zero element of the null space of \mathcal{O} and $w_{si}(\mathbf{X})$ is the i^{th} component of $w_s(\mathbf{X})$ [41].

It is possible to use a software package capable of performing symbolic computations to obtain the different variations of \mathcal{O} and to calculate its rank. Matlab and Maple are widely available examples of such software packages. However, it should be noted that such

computer based rank calculations are usually based on numerical substitution of symbolic variables. This can lead to erroneous results if not performed with care. Moreover, local observability, as the name implies, is a local condition that depends on the state trajectory. Thus it is important to identify the state trajectories for which the system is observable. A computer based rank calculation does not provide a straightforward method to identify these trajectories. For these reasons, the observability analyses presented in the later chapters of this thesis are all performed through analytical calculations instead of through symbolic computational software.

2.8 Quadrotor Simulator

To test the validity of the observability properties and also to test the performance of the designed estimators, two Matlab/Simulink based quadrotor MAV simulators were employed. The first simulator uses the simplified dynamic model of a quadrotor MAV that was developed in Section 2.4. As mentioned before, this model assumes near hover operating conditions and as such does not incorporate some of the secondary aerodynamic forces that become dominant in more aggressive flight envelopes. This model was intentionally kept simple to analyse the estimator designs in chapters 3 and 4 under ideal conditions. In addition to the simulation results, chapters 3 and 4 present extensive experimental results along with ground truth state estimators to analyse the proposed estimators under practical conditions. The dynamic and kinematic equations associated with this first simulator are reproduced below.

Force equation:

$${}^B\mathbf{F} = f_T \mathbf{e}_3 - \bar{D}_L {}^B\mathbf{v}_\infty$$

Moment equation:

$${}^B\boldsymbol{M} = \begin{bmatrix} 0 & -dc_T & 0 & dc_T \\ -dc_T & 0 & dc_T & 0 \\ c_Q & -c_Q & c_Q & -c_Q \end{bmatrix} \begin{bmatrix} \varpi_1^2 \\ \varpi_2^2 \\ \varpi_3^2 \\ \varpi_4^2 \end{bmatrix}$$

Rigid body kinematic equations:

$$\begin{aligned} {}^E\dot{\boldsymbol{p}} &= {}^E\boldsymbol{v} \\ {}^E\dot{\boldsymbol{v}} &= \boldsymbol{g} + \frac{1}{m} {}^E\boldsymbol{R} {}^B\boldsymbol{F} \\ {}^B\dot{\boldsymbol{\Omega}} &= J^{-1}({}^B\boldsymbol{M} - {}^B\boldsymbol{\Omega} \times J {}^B\boldsymbol{\Omega}) \\ \dot{\boldsymbol{\Theta}} &= \Xi {}^B\boldsymbol{\Omega} \end{aligned}$$

The coefficients required for above equations were derived through a parameter identification process similar to that described Bangura and Mahony [33] using the ARDrone quadrotor MAV platform introduced in Section 2.9. The parameter and noise values used in this simulation are summarised in Table 2.2.

TABLE 2.2: Parameters used in first simulator

Description	Variable	Value
Distance from the quadrotor centre of mass to the propeller hub	d	0.23m
Magnitude of gravity vector	g	$9.81ms^{-1}$
Total mass of the quadrotor	m	0.5kg
Quadrotor moment of inertia	J_{xx}	$1.455 \times 10^{-3}kgm^{-3}$
Quadrotor moment of inertia	J_{yy}	$1.455 \times 10^{-3}kgm^{-3}$
Quadrotor moment of inertia	J_{zz}	$2.91 \times 10^{-3}kgm^{-3}$
Thrust coefficient	c_T	$2.92 \times 10 - 5$
Propeller drag coefficient	c_Q	$3.12 \times 10 - 7$
Induced drag coefficient	d_i	0.04

The second simulator was used to validate all estimator designs in Chapter 5. The reason for using a different simulator stems from the nature of the estimators designed in Chapter 5, which focuses on estimating the quadrotor MAV pose in windy environments. In this case it is difficult to perform the experiments in a realistic manner and still obtain ground

truth estimates to asses the accuracy of the state estimators. Also, Chapter 5 aims to produce estimates of wind velocity simultaneously with the quadrotor MAV pose. Obtaining true wind velocities to analyse the accuracy of wind velocity estimates is a complicated task in real world experiments. To augment these shortcomings of the available experimental setup, a more realistic, high fidelity quadrotor MAV simulator with an integrated wind model was required. This requirement was fulfilled by utilizing the quadrotor MAV simulator that was developed as a part of the Stanford Testbed for Autonomous Rotorcraft for Multi Agent Control (STARMAC) [43] project. The quadrotor dynamic model used in this simulator incorporates additional secondary aerodynamic forces such as full blade flapping dynamics and translational lift and drag forces that affect thrust generation at high speeds. It also incorporates a realistic wind model with the aim of simulating typical wind conditions in urban environments. A detailed description of the quadrotor dynamics and wind model of this simulator was presented by Waslander and Wang [44]. More information on the wind model is also provided in Chapter 5.

Both these simulators were augmented with the same sensor models. The following equations, discretized with a time step of 0.005s, were used to simulate accelerometers and gyroscopes operating at 200Hz.

$$\begin{aligned} {}^B\boldsymbol{\omega}_g &= \boldsymbol{\Omega} + \boldsymbol{\beta}_g + \boldsymbol{\eta}_g \\ \dot{\boldsymbol{\beta}}_g &= \boldsymbol{\eta}_{\beta g} \\ {}^B\boldsymbol{a} &= {}^B_R({}^E\dot{\boldsymbol{v}} - \boldsymbol{g}) + \boldsymbol{\beta}_a + \boldsymbol{\eta}_a \\ \dot{\boldsymbol{\beta}}_a &= \boldsymbol{\eta}_{\beta a} \end{aligned}$$

The noise values used in both simulations are summarised in Table 2.3. These values are based on the IDG-500 gyroscope and BMA150 accelerometer found in the ARDrone quadrotor MAV platform using the stochastic model parameter identification process described by Park and Gao [34].

TABLE 2.3: Noise variances used in both simulators

Description	Variable	Value
Gyroscope measurement noise	η_g	0.01rads^{-1}
Accelerometer measurement noise	η_a	0.1ms^{-2}
Gyroscope bias drift noise	$\eta_{\beta g}$	0.001rads^{-2}
Accelerometer bias drift noise	$\eta_{\beta a}$	0.01ms^{-3}
Gyroscope initial bias	β_{g0}	0.1rads^{-1}
Accelerometer initial bias	β_{a0}	0.2ms^{-2}

2.8.1 Visual Simultaneous Localization And Mapping Simulator

The state estimator designs presented in Chapter 4 makes use of pose estimates obtained from a Visual Simultaneous Localization and Mapping (VSLAM) algorithm. To evaluate the performance of those estimators, a simulation framework was developed using Matlab. This framework consisted of two components. First component is a virtual world consisting of uniformly distributed point features and a pinhole camera assumed to be mounted on the quadrotor MAV, facing forward. Given the current pose of the pinhole camera, this component returns the images that would be captured by triggering the camera at a rate of 10Hz. The true pose of the quadrotor MAV available from either of the quadrotor MAV simulations described in the previous section was provided to this component as the pose of the camera. This allows to capture a sequence of images from a simulated camera onboard the quadrotor MAV, as it travels within the virtual world.

The second component of this simulation was a VSLAM estimator that processes these images to produce and estimate of the camera pose. An open-source implementation [45] of the Inverse-Depth monocular SLAM algorithm was used for this purpose. More details of this implementation can be found in Appendix B.

2.9 Experimental set-up

The quadrotor platform used for the experiments presented in this thesis is the Parrot ARDrone⁷ (see Fig. 2.7). The ARDrone weighs about 420g including the protective hull and has a flight time of about 10 minutes. It is equipped with a wide array of sensors

⁷<http://ardrone.parrot.com/parrot-ar-drone>

including a triad of accelerometers, a triad of gyroscopes, two cameras -one facing front and other facing down- and a downward pointing sonar sensor. The forward facing camera is equipped with a 93^0 wide-angle lens and produces images with a resolution of 320×240 pixels. All sensor data from the ARDrone can be wirelessly transmitted to a ground station PC either running Windows or Linux. An open source C API which can be easily extended to develop application on the ground station to process incoming sensor data and to send out control commands to the ARDrone is provided by the manufacturers. It is also equipped with a pre-programmed closed source attitude control system, which takes care of the low-level stabilisation and control tasks, while providing users the ability to develop applications for higher level navigational tasks.

The images required for visual-inertial fusion experiments detailed in chapters 4 and 5 were captured using the front camera of the ARDrone. The intrinsic parameters of this camera were derived using the Camera Calibration Toolbox by Bouguet [46]. The relative orientation of the camera with respect to $\{B\}$ was obtained using accelerometer measurements and calibration images captured by the camera according to the method detailed by Lobo and Dias [47]. The approximate position of the camera with respect to $\{B\}$ was obtained through manual measurements.



FIGURE 2.7: ARDrone Quadrotor used for experiments

It is desirable to have “ground truth” states trajectories for performance evaluation of proposed estimators. Therefore, all ARDrone experiments were performed in a Vicon motion capture environment, approximately $6 \times 4 \times 3$ m in size. The Vicon motion capture system uses a set of reflective markers rigidly attached to the quadrotor body (see Fig. 2.8). These are observed by 8 fixed IR cameras which are connected to a specialized hardware unit that captures and stores the image data. These images can then be post-processed using the Vicon iQ software to directly compute the orientation and position

of the quadrotor with respect to the Vicon coordinate frame at a rate of 120Hz. Vicon position data was numerically differentiated to obtain velocity estimates, which were then transformed to the body coordinate frame using Vicon orientation data.

The accuracy and precision data for this Vicon setup was not available from the OEM due to it being no longer supported by them. To obtain this data, an experiment was performed by measuring distance between two stationary markers 10cm apart from each other using both the Vicon measurements and measurements obtained from a Vernier caliper. These measurements indicated an average error in the Vicon measurement of 1mm with a standard deviation of 0.1mm. Given that this accuracy and precision are an order of magnitude lower than those for the best estimates obtained from the state estimators designed in this thesis, it was decided that the Vicon measurements could be treated as ground truth state estimates.



FIGURE 2.8: Vicon motion capture setup. (a) - ARDrone quadrotor attached with four reflective markers. Also shown is the body coordinate frame. (b) - ARDrone quadrotor operating in the Vicon environment. Note the Vicon IR cameras fixed to the wall.

In all experiments, ARDrone was manually piloted within the Vicon environment using a joystick attached to the ground station computer. The images from the forward facing camera of the ARDrone were captured at approximately 10Hz along with accelerometer and gyroscope measurements at 200Hz. These measurements were timestamped on-board the MAV and wirelessly transmitted to a laptop computer executing the ARDrone Ground Control Station (GCS) software. Vicon generated ground truth state estimated were also stored in a separate PC. Matlab computing environment in another PC was used for post processing of all data. The EKF implementations were also performed within the Matlab

computing environment and the estimation tasks performed in an off-line manner. Figure 2.9 illustrates the complete experimental setup.

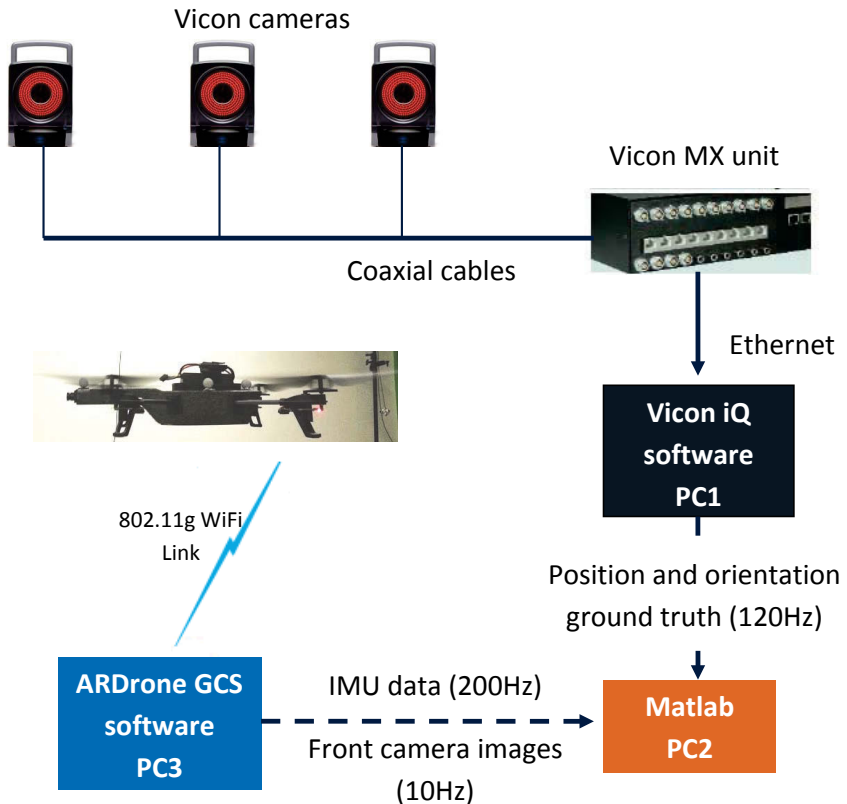


FIGURE 2.9: Setup used for ARDrone experiments

2.10 Discussion

This chapter presented the main theoretical framework employed in this thesis to design and analyse state estimators for quadrotor MAVs. It also detailed the simulation and experimental setup that would be employed throughout the thesis to quantitatively analyse the performance of the designed state estimators, the first of which is presented in the next chapter.

Chapter 3

Model-Aided Inertial Estimators

3.1 Introduction

Inertial sensors play a crucial role in estimating the state of robotic platforms with fast dynamics. The underlying concept of all Inertial Navigation Systems (INS) is to integrate accelerometer and gyroscope measurements to obtain a relative position and orientation estimate of the platform to which the sensors are attached [48]. In practice, the measurements of all inertial sensors are corrupted by various noise sources. Therefore, such an integration causes the estimated pose to deviate from the true pose over time. The amount of deviation for a given time period depends on the accuracy and precision of the employed inertial sensors. Therefore, in the absence of other information about the motion of the vehicle in consideration, all INS have a period of operation after which their estimates become far too inaccurate to be of any use.

For example, inertial navigation systems that employ navigation grade IMUs can produce pose estimates that remain sufficiently accurate up to several hours [49], [50]. However, such IMUs are extremely expensive and bulky, making them unsuitable for mobile robotic applications. Barshan and Durrant-Whyte [51] applied the concepts of inertial navigation to the state estimation of ground robots using a relatively less expensive industrial grade inertial sensor package. They showed that position estimates obtained from the this set-up were only reliable over a period of 5 - 10s, thus concluding that even industrial grade

inertial sensors are not suitable for the task of position estimation of mobile robots unless other means are employed to reduce or limit the estimation error.

The unbounded pose drift associated with the integration of noisy IMU measurements can be constrained if periodic pose related information is available from some other source. There are two main sources or “aids” from which such information can be obtained. First are exteroceptive sensors such as GPS, laser range finders and cameras. The suitability of such sensors for the MAV pose estimation task is discussed in Chapter 4. The discussion in this chapter focuses on the second source of information, namely the use of kinematic or dynamic constraints of the platform in consideration.

More specifically, the focus of this chapter is on developing a state estimation algorithm suitable for quadrotor MAV by only employing MEMS inertial sensor measurements and kinematic or dynamic constraints. It first introduces a state-of-the-art attitude estimator for MAVs that makes use of the zero-accelerations kinematic constraint to limit the drift associated with integrating gyroscope measurements. After detailing the shortcomings of this approach, a novel state estimator design for quadrotor MAVs is proposed. This novel design makes use of quadrotor MAV dynamics derived in Chapter 2 to aid the state estimation process, resulting in improved attitude estimation accuracy. Additionally and more importantly, this proposed design is capable of producing a drift free estimate of two components of the quadrotor body frame velocity whereas the existing algorithms can only produce an attitude estimate. The advantages of the proposed state estimator design are illustrated through real-world experiments performed with a quadrotor MAV.

3.2 Related Work

In one of the earliest examples of applying the concepts of inertial navigation for ground robot state estimation, Barshan and Durrant-Whyte [51] made use of industrial grade inertial sensor package consisting of accelerometers, gyroscopes and inclinometers. They illustrated that by employing accurate models for the measurement errors, it is possible to produce orientation estimates that were reliable over a period of at least 10 minutes. They also showed that position estimates obtained from the same set-up were only reliable

over a period of 5 - 10s. In general, all inertial estimators need to be aided through external means to bound the pose estimation error induced by the integration of noisy sensor measurements. Two main categories of inertial estimators can be identified in the literature depending on the type of information source employed for this aiding.

The first category makes use of additional sensors to aid inertial estimators. When the objective is to obtain orientation estimates, the commonly used methodology is to use sensors that can observe a known fixed vector, in the body coordinate frame. These sensors can include: star trackers [52], sun sensors [53] and magnetometers [54]. These measurements are then used to reset the orientation estimation error caused by the integration of gyroscope measurements. If position estimates are required, then an absolute position measurement system such as GPS can be employed. In addition to limiting the position estimation errors, GPS measurements can also be employed to estimate the inertial acceleration of the vehicle in consideration, thereby enabling the accelerometers to be used as tilt sensors observing the gravity vector. This measurement of the gravity vector and the measurement of the earth magnetic field obtained by a magnetometer can then be used to limit the orientation estimation errors associated with the integration of gyroscope measurements. Hua [55] provides the details of such a set-up.

The second category of inertial estimators does not make use of additional sensors. Instead, they employ the kinematic and dynamic constraints of the platform to which the inertial sensors are attached to aid the estimation process. Often these are soft constraints, based on the simplified characteristics of the mobile robotic platform under consideration. For example, the zero-velocity constraint employed in ground robot state estimators operates under the assumption that the periods when the robot is stationary can be identified by observing wheel encoder measurements. During these periods, the velocity estimates can be reset to bound the error growth. In a similar manner, Dissanayake et al. [16] exploited the nonholonomic constraints governing the motion of a land vehicle moving on a surface to improve the accuracy of roll and pitch estimates obtained by fusing accelerometer and gyroscope measurements. In another example, Koifman and Bar-Itzhack [17] illustrated how the aircraft dynamics of a fixed wing MAV can be used to aid a consumer grade INS, so that the estimation accuracy can be improved. They made use of two navigation systems operating in parallel, one consisted of the standard INS equations driven by IMU

measurements and the other consisted of the dynamic model of the aircraft driven by known control inputs. The pose estimates from the two systems were combined in an EKF to estimate the errors of the two navigation systems. Through simulations they demonstrated that these errors can be accurately estimated for flight trajectories that consist of frequent turn manoeuvres. Mahony et al. [18] presented an improved design for attitude estimation of a fixed wing MAV using the measurements from an IMU, air-speed sensor and a first-order dynamic model for the vehicle angle of attack. They made use of the gyroscope measurements, the air-speed measurement and the dynamic model to predict the inertial acceleration of the vehicle during a sustained level turn manoeuvre. This predicted inertial acceleration was then used to derive an estimate of the gravitational acceleration from accelerometer measurement which in-turn was used to derive an estimate of the vehicle attitude.

Kinematic constraints employed for state estimation of ground robotics and fixed wing MAV platforms are unsuitable for quadrotor MAVs which have considerably different characteristics. The state-of-the-art in inertial state estimation for quadrotor MAVs rely on the small inertial acceleration constraint, which assumes that the inertial acceleration of the platform is negligible when compared to the gravitational acceleration. This allows the accelerometers to be used as tilt sensors observing the gravity vector, the measurement of which can then be used to limit the error growth in attitude estimates. Mahony et al. [39] presented an example of such a system and showed that if in addition a magnetometer is available, then the full orientation vector can be recovered. Other similar examples include [56], [57], [58].

However, even the state-of-the-art inertial estimators of this second category for quadrotor MAVs can only produce drift free orientation estimates. Neither the velocity nor the position estimation errors can be bounded by employing the small inertial acceleration assumption. Obtaining drift free position or velocity estimates require additional dynamic or kinematic characteristics of the vehicle to be incorporated in to the estimation process.

Martin and Salaun [14] were the first to suggest that dynamics of quadrotor MAVs could be used to produce drift free velocity estimates relying only on inertial sensors. They illustrated that in the absence of biases, accelerometer measurements can be low pass

filtered to obtain an initial estimate of two components of the quadrotor MAV translational velocity. The state estimator proposed in this chapter is an extension of that approach, and makes use of both accelerometer and gyroscope measurements in a coherent manner to estimate both the MAV attitude and body frame x, y components of the velocity. In addition to obtaining the drift free velocity estimate, the proposed design is also capable of improving the accuracy of the attitude estimate through the use of the MAV dynamic model.

This design was first presented by the author in [15] and later in [19]. Subsequently and independently Leishman et al. [32] presented a similar design that incorporates the quadrotor MAV dynamic equations into an inertial estimator. They also reported similar results to those that are presented later in this chapter.

3.3 Filter Design with Inertial Sensors

This section first presents the basic inertial navigation equations. It then details how kinematic and dynamic constraints of the vehicle in consideration can be employed to aid inertial navigation systems.

Assuming that the accelerometers are placed at the centre of gravity of the platform, that both accelerometer and gyroscope triad are aligned with the body coordinate frame and that they produce ideal measurements, the equations presented in Section 2.5 can be used to derive the basic equations of inertial navigation:

$$\dot{\Theta}(t) = \Xi^B \omega_g \quad (3.1)$$

$$\Theta(t) = \Theta_{t0} + \int_{t0}^t \dot{\Theta}(t) dt \quad (3.2)$$

$${}^E\dot{v}(t) = R^T(t) {}^B a + g \quad (3.3)$$

$${}^E v(t) = v_{t0} + \int_{t0}^t {}^E\dot{v}(t) dt \quad (3.4)$$

$${}^E p(t) = p_{t0} + \int_{t0}^t {}^E v(t) dt \quad (3.5)$$

where $\Theta_{t0}, \mathbf{v}_{t0}, \mathbf{p}_{t0}$ are the initial conditions and $R(t)$ is the rotation matrix constructed from $\Theta(t)$. As mentioned before, the accuracy of MEMS inertial sensors are such that the estimates produced from these basic equations become substantially erroneous within minutes. The remainder of this section presents two estimation algorithms that can be employed to bound the estimation errors of some of the above states. First is an attitude estimator that represents the state-of-the-art in MAV inertial estimation. The second is the proposed attitude and velocity estimator that makes use of the quadrotor MAV dynamic constraints in the estimation process.

3.3.1 Conventional Attitude Estimators

For quadrotor MAVs, the only kinematic constraint that has been used to aid inertial only state estimation is based on the assumption that the inertial accelerations of the vehicle is small when compared to the gravitational acceleration. When the motion of the vehicle satisfies this assumption, the accelerometer triad can be employed as a tilt sensor measuring the gravity vector in the body coordinate frame. However, the bandwidths of MEMS accelerometers may not be adequate to capture the fast rotational dynamics of quadrotor MAVs. Information from the accelerometers can be combined with the rotational rate measurements from gyroscopes to obtain fast and drift free estimates of the vehicle attitude. However, the tilt information obtained from the accelerometers is insensitive to any rotations of the vehicle around the gravity vector. Measurements from an additional sensor such as a magnetometer are required to estimate these rotations. This principle has been widely employed to estimate the orientation of ground robots [56] and fixed-wing MAVs [58]. Mahony et al. [39] applied the same principles successfully for the state estimation of a ducted fan vertical take-off and landing MAV. In a more recent publication, Mahony et al. [31] demonstrated that this method can be used to obtain reasonable orientation estimates for near hover operation of a quadrotor MAV.

In this section, an attitude estimator that captures the essence of this conventional paradigm of aided inertial only state estimation is presented. Note that the design presented here does not employ magnetometers as they are susceptible to unknown soft-iron disturbances

in indoor environments. Therefore, only an attitude estimate of the platform in consideration can be obtained. For this reason this category of state estimators are referred to as “conventional attitude estimators” (CAE) in this thesis.

Specifically, all conventional attitude estimators are based on two main assumptions. The first is that the inertial accelerations of the platform are small when compared to the magnitude of gravity. The second is that the accelerometer biases are constants that can be calculated off-line and subtracted from all subsequent measurements to compensate for bias offset¹. Under these two assumptions, the accelerometers can be used to obtain an estimate of the gravity vector in $\{B\}$. Considering Equation (2.15a), assuming that $\dot{\mathbf{v}}$ is approximately zero, and bias free measurements, the following can be obtained:

$${}^B \mathbf{a} = - {}^B_E R \mathbf{g} + \boldsymbol{\eta}_a. \quad (3.6)$$

In addition, the rotational kinematics of the platform under consideration can be written as:

$$\dot{\Theta} = \Xi({}^b \boldsymbol{\omega}_g - \boldsymbol{\beta}_g - \boldsymbol{\eta}_g). \quad (3.7)$$

Equations 3.6 and 3.7 are independent of the dynamic equations governing the platform motion. For this reason, the conventional attitude estimation algorithms can be used with any vehicle platform as long as the assumption about small inertial accelerations is justified. Equations 3.6 and 3.7 can be employed to design a state estimator for the partial states $\mathbf{X}_{cae} = \{\phi \ \theta \ \beta_{gx} \ \beta_{gy} \ \beta_{gz}\}$. Table 3.1 summarises the process and measurement equations for this estimator. These equations together with the EKF mechanization equations presented in Table 2.1 complete the design of the CAE.

3.3.2 Model-Aided Attitude and Velocity Estimator

If a simple mathematical model that can satisfactorily explain some of the vehicle dynamics is available, then it is possible to improve the accuracy of the conventional estimator. In the case of a quadrotor MAV, it is possible to exploit the dynamic model developed in Chapter

¹The implications of this assumption are discussed in section 3.6

TABLE 3.1: Conventional Attitude Estimator

Process Equations	
$\begin{bmatrix} \dot{\phi} \\ \dot{\theta} \\ \dot{\beta}_{gx} \\ \dot{\beta}_{gy} \\ \dot{\beta}_{gz} \end{bmatrix}$	$= \begin{bmatrix} {}^b\omega_{gx} - \beta_{gx} - \eta_{gx} + t(\theta)s(\phi)({}^b\omega_{gy} - \beta_{gy} - \eta_{gy}) \\ \dots + t(\theta)c(\phi)({}^b\omega_{gz} - \beta_{gz} - \eta_{gz}) \\ c(\phi)({}^b\omega_{gy} - \beta_{gy} - \eta_{gy}) - s(\phi)({}^b\omega_{gz} - \beta_{gz} - \eta_{gz}) \\ \eta_{\beta_{gx}} \\ \eta_{\beta_{gy}} \\ \eta_{\beta_{gz}} \end{bmatrix}$
Measurement Equations	
$\begin{bmatrix} {}^B a_x \\ {}^B a_y \end{bmatrix}$	$= \begin{bmatrix} -gs(\theta) + \eta_{ax} \\ gc(\theta)s(\phi) + \eta_{ay} \end{bmatrix}$

2 to derive such a relationship. As will be apparent later, this dynamic relationship not only improves the accuracy of the attitude estimates but also provides a method to obtain a drift free velocity estimate using only the inertial sensors. For this reason the proposed state estimator is referred to as the Model-aided Attitude and Velocity Estimator (MAVE) in this thesis .

The process equations for the MAVE can be derived from the quadrotor MAV translational dynamics equation from Chapter 2, which is reproduced below:

$${}^E \dot{\mathbf{v}} \approx \mathbf{g} + {}_B^E R \left(\frac{f_T}{m} \mathbf{e}_3 - \bar{D}_L {}^B \mathbf{v}_\infty \right). \quad (3.8)$$

The discussion in this chapter is restricted to the case when the quadrotor MAV is operating in environments with zero wind velocity². In such a situation ${}^B \mathbf{v}_\infty = {}^B \mathbf{v}$. Expressing

²The case with wind will be analysed later in Chapter 5

the velocity of the quadrotor MAV in $\{B\}$ results in:

$${}^E \dot{\mathbf{v}} = {}^E R_B {}^B \dot{\mathbf{v}} + {}^E R_B ({}^B \boldsymbol{\Omega} \times {}^B \mathbf{v}) \quad (3.9)$$

where ${}^E \mathbf{v} = {}^E R_B {}^B \mathbf{v}$ and ${}^B \dot{\mathbf{v}}$ is the time derivative of ${}^B \mathbf{v}$. Substituting for ${}^E \dot{\mathbf{v}}$ in Equation 3.8 results in:

$${}^B \dot{\mathbf{v}} \approx {}^B {}_E R \mathbf{g} + \frac{f_T}{m} \mathbf{e}_3 - \bar{D}_L {}^B \mathbf{v} - {}^B \boldsymbol{\Omega} \times {}^B \mathbf{v}. \quad (3.10)$$

Considering the typical flight characteristics of the quadrotor MAV, it is reasonable to assume that the second order term ${}^B \boldsymbol{\Omega} \times {}^B \mathbf{v}$ is negligible near hover. This results in:

$${}^B \dot{\mathbf{v}} \approx {}^B {}_E R \mathbf{g} + \frac{f_T}{m} \mathbf{e}_3 - \bar{D}_L {}^B \mathbf{v}. \quad (3.11)$$

However, in practice, slight deviation from this ideal model can be expected. To account for these deviations, the quadrotor MAV dynamic model in Equation 3.11 can be augmented with a process noise variable:

$${}^B \dot{\mathbf{v}} = {}^B {}_E R \mathbf{g} + \frac{f_T}{m} \mathbf{e}_3 - \bar{D}_L {}^B \mathbf{v} + \boldsymbol{\eta}_v \quad (3.12)$$

where $\boldsymbol{\eta}_v$ is a 3×1 vector of zero mean WGN terms.

Estimating the thrust f_T generated by the propellers require propeller speed measurements, which are not available with most commercial quadrotor platforms that use off-the-shelf motor controllers. However, analysing the elements of the accelerometer measurement expressed in Equation 2.16 reveals that $\frac{f_T}{m}$ can be replaced by ${}^B a_z - \beta_{az} + \eta_{az}$. Equation 3.12 can now be written as:

$${}^B \dot{\mathbf{v}} = {}^B {}_E R \mathbf{g} + ({}^B a_z - \beta_{az}) \mathbf{e}_3 - \bar{D}_L {}^B \mathbf{v} + \boldsymbol{\eta}_v \quad (3.13)$$

where η_{az} has been incorporated into η_{vz} . Rotational kinematic Equation 3.7 and accelerometer and gyroscope bias Equations 2.15b and 2.14b make up the rest of the process model for the MAVE.

The measurements for the MAVE are obtained from the ${}^B a_x$, ${}^B a_y$ accelerometers, the equation for which can be extracted from Equation 2.16 as:

$$\begin{bmatrix} {}^B a_x \\ {}^B a_y \end{bmatrix} = \Upsilon(\bar{D}_L {}^B v + \beta_a + \eta_a) \quad (3.14)$$

where

$$\Upsilon = \begin{bmatrix} 1 & 0 & 0 \\ 0 & 1 & 0 \end{bmatrix}.$$

Table 3.2 summarizes the process and measurement equations discussed in this section. It is possible to design a state estimator for the partial state $\mathbf{X}_{mave} = \{{}^B v \ \Theta \ \beta_a \ \beta_g\}$ by combining these equations with the EKF mechanization equations presented in 2.1. However, before proceeding with the filter design, the observability of the MAVE need to be analysed to discern whether there are any unobservable modes in the systems.

TABLE 3.2: Model-Aided Attitude and Velocity Estimator - Initial Design

Process Equations
$\begin{bmatrix} {}^B \dot{v} \\ \dot{\Theta} \\ \dot{\beta}_a \\ \dot{\beta}_g \end{bmatrix} = \begin{bmatrix} {}^B_E R g + ({}^B a_z - \beta_{az}) e_3 - \bar{D}_L {}^B v + \eta_v \\ \Xi({}^b \omega_g - \beta_g - \eta_g) \\ \eta_{\beta a} \\ \eta_{\beta g} \end{bmatrix}$

Measurement Equations
$\begin{bmatrix} {}^B a_x \\ {}^B a_y \end{bmatrix} = \Upsilon(\bar{D}_L {}^B v + \beta_a + \eta_a)$

3.4 Observability Analysis

Mahony et al. [39] analysed a non-linear observer that makes use of the same equations as the conventional attitude estimator and concluded that the roll and pitch angles with gyroscope biases are observable. In this section the observability of the proposed Model-Aided Attitude and Velocity Estimator (MAVE) is analysed.

The measurement equation of the MAVE is linear and the process equations can be linearised around hover condition assuming small ϕ and θ angles. The linearised system excluding the noise terms, which do not affect the observability of a given system, can thus be represented as:

$$\dot{\mathbf{X}}_{mave} = \begin{bmatrix} {}^B\dot{\mathbf{v}} \\ \dot{\Theta} \\ \dot{\beta}_a \\ \dot{\beta}_g \end{bmatrix} = \underbrace{\begin{bmatrix} -\bar{D}_L & G & \Gamma & \mathbf{0}_{3 \times 3} \\ \mathbf{0}_{3 \times 3} & \mathbf{0}_{3 \times 3} & \mathbf{0}_{3 \times 3} & -I_3 \\ \mathbf{0}_{3 \times 3} & \mathbf{0}_{3 \times 3} & \mathbf{0}_{3 \times 3} & \mathbf{0}_{3 \times 3} \\ \mathbf{0}_{3 \times 3} & \mathbf{0}_{3 \times 3} & \mathbf{0}_{3 \times 3} & \mathbf{0}_{3 \times 3} \end{bmatrix}}_A \mathbf{X}_{mave} + \begin{bmatrix} {}^B a_z \mathbf{e}_3 \\ {}^b \omega_g \\ \mathbf{0}_{3 \times 1} \\ \mathbf{0}_{3 \times 1} \end{bmatrix} \quad (3.15)$$

$$\mathbf{y} = \begin{bmatrix} {}^B a_x \\ {}^B a_y \end{bmatrix} = \underbrace{\begin{bmatrix} -\Upsilon \bar{D}_L & \mathbf{0}_{2 \times 3} & \Upsilon & \mathbf{0}_{2 \times 3} \end{bmatrix}}_C \mathbf{X}_{mave} \quad (3.16)$$

where I_n denotes a $n \times n$ identity matrix, $\mathbf{0}_{p \times q}$ denotes a $p \times q$ matrix of all zeros and

$$G = \begin{bmatrix} 0 & -g & 0 \\ g & 0 & 0 \\ 0 & 0 & 0 \end{bmatrix} \quad \Gamma = \begin{bmatrix} 0 & 0 & 0 \\ 0 & 0 & 0 \\ 0 & 0 & 1 \end{bmatrix}.$$

The observability matrix \mathcal{O}_{mave} can now be constructed as:

$$\begin{aligned}\mathcal{O}_{mave} &= \left[C^T \quad (CA)^T \quad (CA^2)^T \quad (CA^3)^T \quad (CA^4)^T \quad \dots (CA^{11})^T \right]^T \quad (3.17) \\ &= \begin{bmatrix} -k\Upsilon & \mathbf{0}_{2 \times 3} & \Upsilon & \mathbf{0}_{2 \times 3} \\ k^2\Upsilon & -k\Upsilon G & \mathbf{0}_{2 \times 3} & \mathbf{0}_{2 \times 3} \\ 2k^2\Upsilon & -2k\Upsilon G & \mathbf{0}_{2 \times 3} & \mathbf{0}_{2 \times 3} \\ k^4\Upsilon & -k^3\Upsilon G & \mathbf{0}_{2 \times 3} & -k^2\Upsilon G \\ -k^5\Upsilon & k^4\Upsilon G & \mathbf{0}_{2 \times 3} & k^3\Upsilon G \\ \vdots & \vdots & \vdots & \vdots \\ k^{12}\Upsilon & -k^{11}\Upsilon G & \mathbf{0}_{2 \times 3} & -k^{10}\Upsilon G \end{bmatrix}\end{aligned}$$

It can be seen that (CA^2) is a linear multiple of (CA) and that $CA^4 \dots CA^{11}$ are linear multiples of CA^3 . Thus \mathcal{O}_{mave} can be redefined as:

$$\mathcal{O}_{mave} \rightarrow \left[C^T \quad (CA)^T \quad (CA^3)^T \right]^T \quad (3.18)$$

which is a 6×12 matrix and therefore has rank at most of 6. The following 6 null vectors of \mathcal{O}_{mave} can also be identified:

$$N(\mathcal{O}_{mave}) = \begin{bmatrix} \mathbf{n}_1 \\ \mathbf{n}_2 \\ \mathbf{n}_3 \\ \mathbf{n}_4 \\ \mathbf{n}_5 \\ \mathbf{n}_6 \end{bmatrix}^T = \begin{bmatrix} \mathbf{e}_3 & \mathbf{0}_{3 \times 1} & \mathbf{0}_{3 \times 1} & \mathbf{0}_{3 \times 1} \\ \mathbf{0}_{3 \times 1} & \mathbf{e}_3 & \mathbf{0}_{3 \times 1} & \mathbf{0}_{3 \times 1} \\ \mathbf{0}_{3 \times 1} & \mathbf{0}_{3 \times 1} & \mathbf{e}_3 & \mathbf{0}_{3 \times 1} \\ \mathbf{0}_{3 \times 1} & \mathbf{0}_{3 \times 1} & \mathbf{0}_{3 \times 1} & \mathbf{e}_3 \\ \frac{1}{k_1}\mathbf{e}_1 & -\frac{1}{g}\mathbf{e}_2 & \mathbf{e}_1 & \mathbf{0}_{3 \times 1} \\ \frac{1}{k_1}\mathbf{e}_2 & \frac{1}{g}\mathbf{e}_1 & \mathbf{e}_2 & \mathbf{0}_{3 \times 1} \end{bmatrix}^T \quad (3.19)$$

where $\mathbf{e}_1 = [1 \ 0 \ 0]^T$ and $\mathbf{e}_2 = [0 \ 1 \ 0]^T$. The first four null vectors represent four unobservable states, namely ${}^Bv_z, \psi, \beta_{az}, \beta_{gz}$. Null vectors $\mathbf{n}_5, \mathbf{n}_6$ indicates that the accelerometer biases β_{ax}, β_{ay} are involved in the remaining two unobservable modes. As mentioned before, when only inertial sensors are available, all attitude estimators employ the assumption that the accelerometer biases are constants, albeit unknown [31], [39].

This was the case with the conventional attitude estimator design presented in the previous section. Adopting the same assumption, the process and measurement equations for the modified MAVE can be written as:

$$\dot{\mathbf{X}}_{m_mave} = \begin{bmatrix} {}^B\dot{\mathbf{v}} \\ \dot{\Theta} \\ \dot{\beta}_g \end{bmatrix} = \underbrace{\begin{bmatrix} -\bar{D}_L & G & \mathbf{0}_{3 \times 3} \\ \mathbf{0}_{3 \times 3} & \mathbf{0}_{3 \times 3} & -\mathbf{I}_3 \\ \mathbf{0}_{3 \times 3} & \mathbf{0}_{3 \times 3} & \mathbf{0}_{3 \times 3} \end{bmatrix}}_{A_m} \mathbf{X}_{m_mave} + \begin{bmatrix} {}^B a_z \mathbf{e}_3 \\ {}^b \omega_g \\ \mathbf{0}_{3 \times 1} \end{bmatrix} \quad (3.20)$$

$$\mathbf{y}_m = \begin{bmatrix} {}^B a_x \\ {}^B a_y \end{bmatrix} = \underbrace{\begin{bmatrix} -\Upsilon \bar{D}_L & \mathbf{0}_{2 \times 3} & \mathbf{0}_{2 \times 3} \end{bmatrix}}_{C_m} \mathbf{X}_{m_mave} \quad (3.21)$$

As before, the observability matrix \mathcal{O}_{m_mave} for the modified MAVE can be identified as:

$$\begin{aligned} \mathcal{O}_{m_mave} &\rightarrow \left[C_m^T \quad (C_m A_m)^T \quad (C_m A_m^3)^T \right]^T \quad (3.22) \\ &= \begin{bmatrix} -k\Upsilon & \mathbf{0}_{2 \times 3} & \mathbf{0}_{2 \times 3} \\ k^2\Upsilon & -k\Upsilon G & \mathbf{0}_{2 \times 3} \\ k^4\Upsilon & -k^3\Upsilon G & -k^2\Upsilon G \end{bmatrix} \\ &= \begin{bmatrix} \Upsilon & \mathbf{0}_{2 \times 3} & \mathbf{0}_{2 \times 3} \\ \mathbf{0}_{2 \times 3} & \Upsilon & \mathbf{0}_{2 \times 3} \\ \mathbf{0}_{2 \times 3} & \mathbf{0}_{2 \times 3} & \Upsilon \end{bmatrix} \end{aligned}$$

where the last step was obtained through block Gaussian elimination of \mathcal{O}_{m_mave} . Thus the rank of \mathcal{O}_{m_mave} is six and a calculation of its null space shows that ${}^B v_z, \psi, \beta_{gz}$ are the three unobservable modes.

It is now possible to redefine the MAVE by discarding the unobservable states ${}^B v_z, \psi, \beta_{gz}$. The process and measurement equations of this redefined MAVE can be extracted from Equations in Table 3.2. Out of the three unobservable states, ${}^B v_z, \psi$ can be easily removed as the other states do not depend on them. Removing β_{gz} is not straightforward as the (1, 3) and (2, 3) elements of Ξ are non-zero. However, by analysing the process and measurement equations of Table 3.2, it can be seen that the main source of information for the attitude is the accelerometer measurements. The gyroscopes only produce high frequency attitude information and for this reason the impact of β_{gz} on the attitude

estimate is negligible for near hover operation. For this reason, the state β_{gz} can be replaced by an offline estimate of β_{gz} without a significant impact on the accuracy of the MAVE.

The process and measurement equations for the final MAVE design are summarised in Table 3.3. These equations together with the EKF mechanization equations presented in Table 2.1 complete the MAVE design.

TABLE 3.3: Model-Aided Attitude and Velocity Estimator - Final Design

Process Equations	
$\begin{bmatrix} {}^B\dot{v}_x \\ {}^B\dot{v}_y \\ \dot{\phi} \\ \dot{\theta} \\ \dot{\beta}_{gx} \\ \dot{\beta}_{gy} \end{bmatrix}$	$= \begin{bmatrix} -gs(\theta) - k_1 {}^Bv_x + \eta_{vx} \\ gc(\theta)s(\phi) - k_1 {}^Bv_y + \eta_{vy} \\ {}^b\omega_{gx} - \beta_{gx} - \eta_{gx} + t(\theta)s(\phi)({}^b\omega_{gy} - \beta_{gy} - \eta_{gy}) \\ \dots + t(\theta)c(\phi)({}^b\omega_{gz} - \beta_{gz} - \eta_{gz}) \\ c(\phi)({}^b\omega_{gy} - \beta_{gy} - \eta_{gy}) - s(\phi)({}^b\omega_{gz} - \beta_{gz} - \eta_{gz}) \\ \eta_{\beta_{gx}} \\ \eta_{\beta_{gy}} \end{bmatrix}$
Measurement Equations	
<hr/>	
$\begin{bmatrix} {}^B a_x \\ {}^B a_y \end{bmatrix}$	$= \begin{bmatrix} -k_1 {}^Bv_x + \eta_{ax} \\ -k_1 {}^Bv_y + \eta_{ay} \end{bmatrix}$

3.5 Experiments

All flights to gather experimental data were conducted in the Vicon motion capture environment with the set-up detailed in Section 2.9. The data from one such flight is employed in this section to evaluate the performance of the CAE and MAVE.

During this flight, the AR Drone was manually operated within the Vicon environment in a random pattern. A three-dimensional trace of the path taken by the MAV is shown in Fig. 3.1.

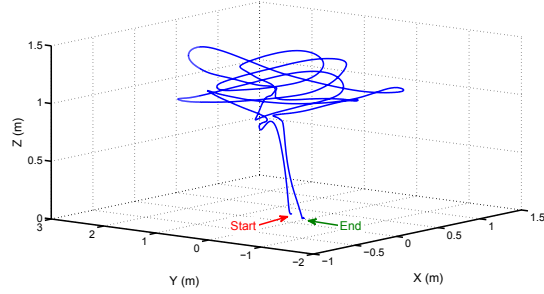


FIGURE 3.1: Three-dimensional flight path of the ARDrone experiment.

Fig. 3.2 and 3.3 shows the estimates of the Conventional Attitude Estimator (CAE) and the proposed Model-aided Attitude and Velocity Estimator (MAVE) respectively, together with the ground truth obtained from the Vicon system. It can be seen that the MAVE attitude estimates have improved accuracy when compared to those of the CAE. This is specially the case with the roll estimates. Also, this improvement is more pronounced in places where the quadrotor changes its flight direction (for example around 235 and 245 sec). This is due to the fact that during those intervals, the quadrotor undergoes high inertial accelerations. In such situations the assumption that the accelerometer measurements are dominated by gravitational acceleration fails to hold. As the CAE is based on this assumption, it produces erroneous results when that assumption is violated.

Fig. 3.4(a) and 3.4(b) present a comparison between the errors in the roll and pitch attitude estimates of both estimators. Even with the proposed MAVE, unmodelled dynamics (such as displacement of accelerometer from the centre of mass of the quadrotor) cause increased estimation errors when the quadrotor undergoes large accelerations. However, it is clear that the errors in the proposed design are considerably less than those of the CAE. The Root Mean Square (RMS) error for the roll and pitch angles for the CAE were respectively 2.46 and 3.57 degrees and the same for the MAVE were 1.05 and 1.4 degrees.

Fig. 3.5 presents the velocity estimate from the MAVE together with the ground truth. The CAE does not produce any velocity estimates. However, for comparison purposes the velocity was estimated by integrating inertial accelerations which was calculated by gravity

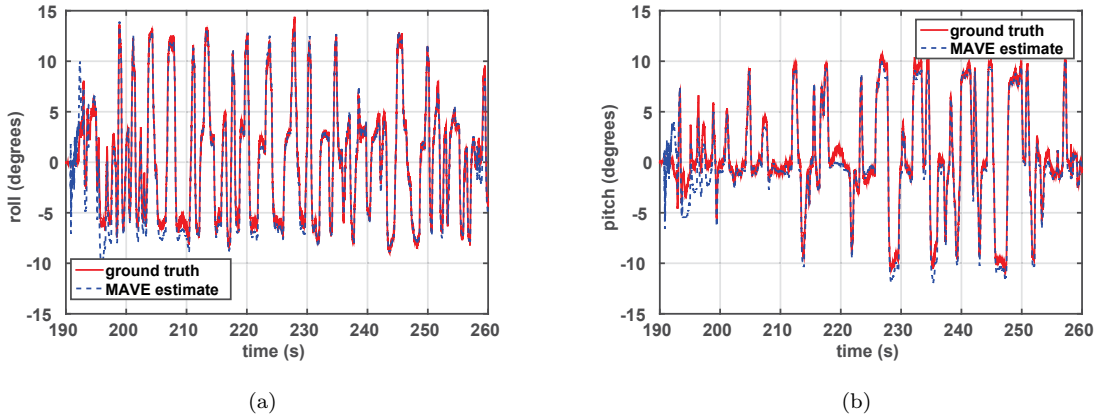


FIGURE 3.2: Comparison of ground truth and MAVE attitude estimates for the ARDrone experiment.

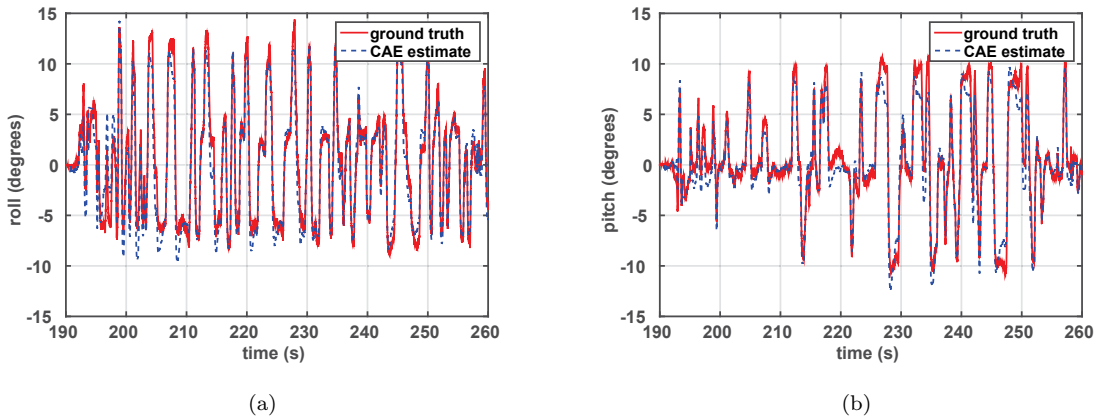


FIGURE 3.3: Comparison of ground truth and CAE attitude estimates for the ARDrone experiment.

compensated accelerometer measurements. This velocity estimate is presented in Fig. 3.6. A comparison between the errors in velocity estimate obtained from two estimators is shown in Fig. 3.7, where total velocity error is the sum of root square errors of both ${}^B\mathbf{x}$ and ${}^B\mathbf{y}$ axes. It is clearly seen that the proposed strategy produces velocity estimates in which errors do not grow with time, while estimating velocity through direct integration of accelerations as implemented in the conventional design leads to a significant drift. As zero velocity updates, that can be used to correct this behaviour in land vehicles, are no longer viable with a MAV without some deliberate control strategies, this points to a significant advantage of the MAVE design.

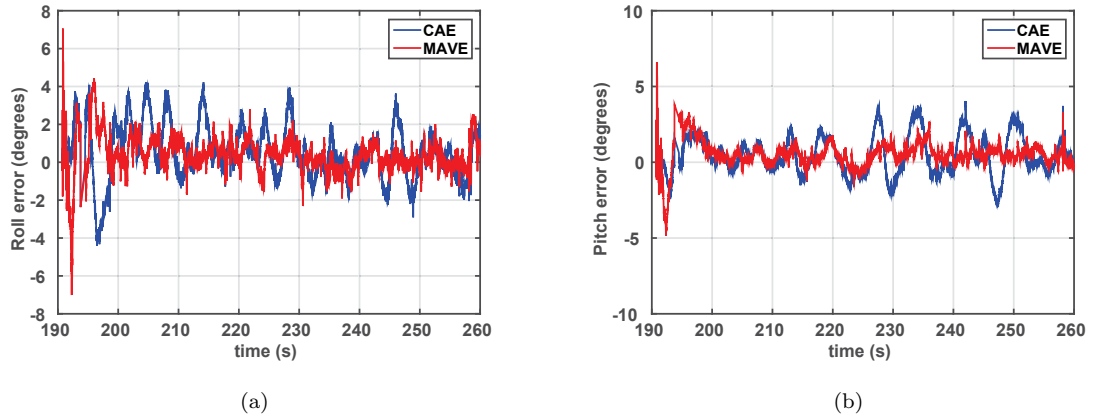


FIGURE 3.4: Attitude estimation errors of MAVE and CAE estimators for the ARDrone experiment.

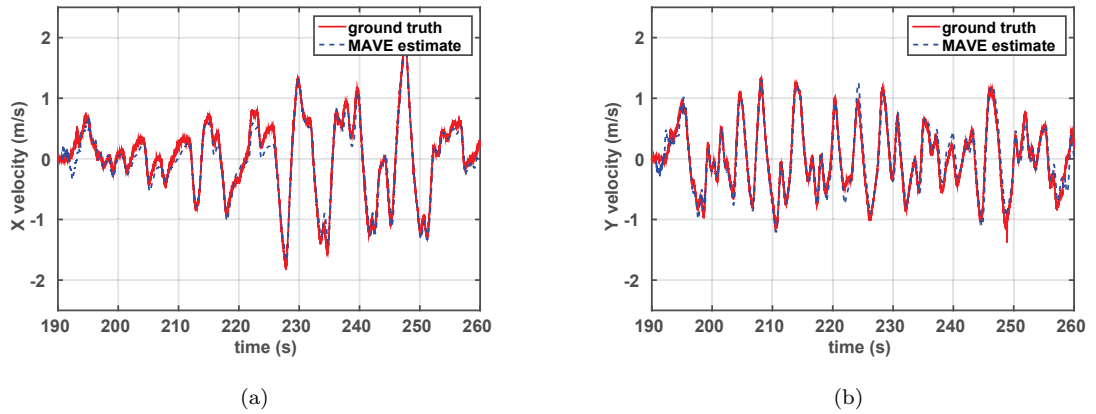


FIGURE 3.5: Comparison of ground truth and MAVE velocity estimates for the ARDrone experiment.

3.6 Discussion and Limitations

The Conventional Attitude Estimator (CAE), by design is platform agnostic. It can be employed for the task of attitude estimation of any platform without modification as long as the underlying assumptions are satisfied. While this is advantageous when designing an off-the-shelf Attitude and Heading Reference System (AHRS), it may not provide the best accuracy when designing a state estimator for a specific type of a mobile robot. The experimental results presented in this chapter demonstrate that the proposed Model-aided Attitude and velocity Estimator (MAVE) design has two advantages over the CAE. First,

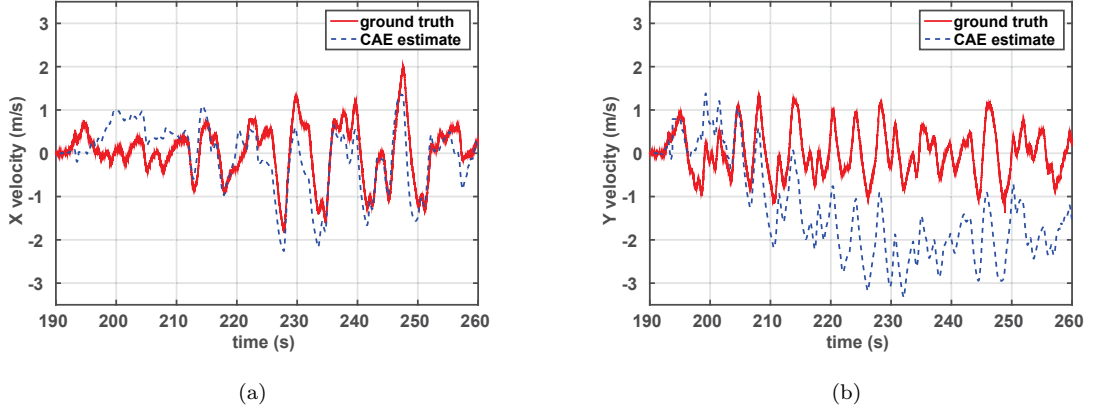


FIGURE 3.6: Comparison of ground truth and CAE velocity estimates for the ARDrone experiment.

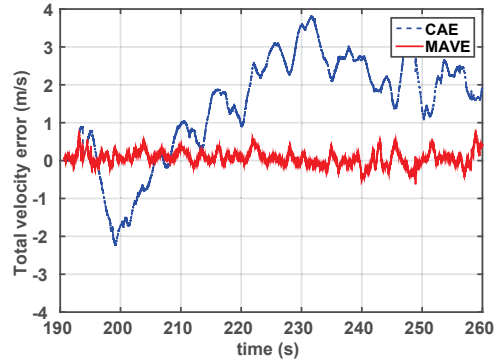


FIGURE 3.7: Total velocity estimation errors of MAVE and CAE estimator designs for the ARDrone experiment.

it produces more accurate attitude estimates and second it produces an estimate of the ${}^B\mathbf{x}, {}^B\mathbf{y}$, components of the quadrotor MAV velocity. The advantage of the MAVE design stems from its ability to employ the dynamic characteristics of the quadrotor MAV in the state estimation process. However, the same dynamics that were employed in the MAVE are not applicable in general to other robotic platforms. Therefore, the MAVE can only be employed for the state estimation of quadrotor MAVs.

One limitation common to both the CAEs and MAVE is their inability to produce an online accelerometer bias estimate. For this reason, implementations of both estimator designs require an offline calibration of the accelerometer biases. An accurate calibration of accelerometer requires the x-y plane of the accelerometer triad be perpendicular to the

gravity vector. It is difficult to achieve this in the field without additional equipment. Moreover, the accelerometer biases are known to have a strong correlation with the temperature of the sensor [59]. Though an off-line temperature calibration may be performed to account for this variation, such calibration process are often tedious and need to be repeated often to account for the varying physical properties of the sensor and its attachment to the circuit board. Therefore, it is advantageous to be able to estimate the accelerometer biases on-line.

Another limitation of both CAEs and MAVE designs is the unobservability of yaw angle. Roll and pitch angles are sufficient to stabilise the quadrotor MAV but yaw angle is necessary if the MAV is required to perform autonomous navigation. Also, the MAVE can only estimates two components of the body frame velocity of the quadrotor MAV. The unobservability of the component of velocity in the Bz direction is a limitation that needs to be overcome for autonomous operation.

Despite these limitations, the proposed MAVE design can successfully replace the state-of-the-art conventional attitude estimates that are currently employed for the state estimation of quadrotor MAVs. Many of the off-the-shelf quadrotor MAV platforms are only equipped with MEMS IMUs, and as such the improved attitude estimates and the new velocity estimates of the MAVE can significantly enhance stability of these platforms. Also the basic concept behind the proposed algorithm can be employed to improve the accuracy of more complex state estimation algorithms for quadrotor MAVs with additional on-board sensors such as GPS, laser range finders or camera sensors. This last case, namely the integration of inertial and visual information, will be further developed in the next chapter to overcome the limitations of the MAVE design.

Chapter 4

Model-Aided Visual Inertial Fusion

4.1 Introduction

The Model-aided Attitude and Velocity Estimator (MAVE) designed in Chapter 3 demonstrated how the quadrotor MAV dynamic model can be successfully employed to improve inertial only state estimators. The MAVE was capable of producing a partial velocity and orientation estimate which are of critical importance during manual and line-of-sight operation of a quadrotor MAV. However, to improve its use as a state estimator that supports fully autonomous operation of the quadrotor MAV, the following functionality needs to be added.

1. Ability to estimate the position of the MAV with respect to an inertial coordinate frame.
2. Ability to estimate the vertical velocity and the Yaw angle of the MAV.
3. Ability to produce an online estimate of the accelerometer biases.

Adding these functionalities require the use of exteroceptive sensors. However, limited payload and power budget impose restrictions on the sensing modalities that can be used

for quadrotor MAV state estimation. Absolute positioning systems such as GPS are obvious candidates but they are not suitable for indoor operation and even for some outdoor environments in which quadrotor MAVs are expected to operate. Recent advances in sensor technology have provided several alternatives to GPS. These include laser range finders, depth cameras and monocular cameras. Quadrotor MAV state estimators based on the fusion of measurements from these three sensor modalities with those of inertial sensors have already been evaluated (see for example [11], [12] and [13]).

Irrespective of the type of exteroceptive sensor employed, all such state estimators for quadrotor MAVs can benefit from the unique dynamic characteristics of the MAV derived in Chapter 2. Similar to the MAVE design of Chapter 3, incorporating the quadrotor MAV dynamic model into the state prediction process and also incorporating the biased velocity measurements obtainable from the accelerometers into the state update process has the potential to improve both the observability and the accuracy of the state estimation algorithms that fuse exteroceptive and inertial sensor measurements. The key objective of this chapter is to explore that potential for one such sensor fusion algorithm; namely the fusion of visual information from a monocular camera with inertial information from an IMU. Algorithms that fuse these two information sources are commonly known as a Visual-Inertial Fusion (VIF) algorithms. This chapter proposes to add yet another information source, namely the quadrotor MAV dynamic model, to a VIF algorithm with the aim of improving its performance.

There are two reasons why monocular vision was chosen as the exteroceptive sensor for the analysis in this chapter. First, monocular cameras are more desirable as sensors for quadrotor MAVs than laser range finders or depth cameras due to their reduced weight and cost. Second, it is more challenging to extract the required pose information from monocular images than from measurements of laser range finders or depth cameras due to the projective nature of monocular cameras. Therefore, monocular VIF algorithms stand to benefit the most from the additional information brought about by the incorporation of the quadrotor dynamic model.

The remainder of this chapter is organized as follows. Section 4.2 presents the related work on vision based estimation and visual-inertial fusion. Section 4.3 details the proposed

model-aided VIF formulation. To benchmark the performance of the proposed design this section also presents a standard VIF formulation without model-aiding. Section 4.4 analyses the observability of both designs and highlights the merits of employing the dynamic model for state estimation. Section 4.5 and 4.6 presents the simulation and experimental results of the two designs to show the performance improvements brought about by model-aiding. Section 4.7 details a more streamlined way of incorporating the quadrotor dynamic into the VIF algorithm by tightly-coupling the three sources of available information; camera measurements, IMU measurements and quadrotor dynamic model. Section 4.8 concludes the chapter with a discussion on the advantages and limitations of the model-aided VIF framework.

4.2 Related Work

4.2.1 Vision Based Estimation

A monocular camera can be thought of as a sensor that measures the bearing to environmental features that fall within its field of view. Given an image sequence acquired while the camera moves through a stationary environment, these bearing measurements can be used to obtain an estimate of the environment structure and the camera motion up to a scale factor [60]. In mobile robotics literature, such an approach is commonly known as Visual Simultaneous Localization and Mapping (VSLAM). There are two main categories of VSLAM algorithms. The first category operates by first identifying environmental features that appear in a pair or more images and then applying a nonlinear optimization algorithm on the camera and feature positions to minimize the feature reprojection errors. This optimization is usually performed for a subset of the image sequence considering the requirement of obtaining real-time estimates for mobile robotic navigational tasks. For example, the Parallel Tracking And Mapping (PTAM) implementation by Klein and Murray [61] performed the optimization over a series of spatially distributed “key frame” images.

The second category of VSLAM algorithms makes use of probabilistic filtering approaches to sequentially process the bearing-only measurements to environmental features as they appear in each image. A real-time implementation of the bearing-only VSLAM based on

an EKF was first presented by Davison [62]. They made use of images obtained at 30 Hz from a hand-held camera operating in a small room size environment. Image patches corresponding to interest points in the environment were tracked throughout the image sequence. Bearing measurements to those features were employed to simultaneously estimate both the camera pose and the 3D position of the features. A similar implementation that also makes use of straight line features was detailed by Smith et al. [63]. The structure of these filter based implementations is such that they can be easily augmented with additional sensor measurements such as those available from an IMU. For this reason, the discussion in this thesis focuses more on filter based VSLAM implementations than those based on optimization. However, it should be noted that VSALM algorithms based on either category are equally applicable to the VIF algorithms discussed in Section 4.3.

A fundamental problem of all filter based bearing-only VSLAM algorithms is the initialization of environmental features. To initialise an environmental feature in the filter, an estimate of its distance from the camera is required. However, multiple bearing-only measurements to each feature are required before this distance, or the feature depth, can be estimated. Davison [62] overcame this problem by employing multiple auxiliary filters for each new feature based on different hypothesis of its depth. After several observations, it is possible to identify the filter that was based on the correct hypothesis and to initialize the environmental feature based on that hypothesis. Bryson and Sukkarieh [64] overcame the feature initialization problem by waiting for the new feature to be observed from multiple camera locations and then using triangulation to obtain an initial position estimate. This meant that new environmental features did not contribute to the filter estimates until they were observed from multiple different camera positions. The need for such "delayed" feature initialization stemmed from fact that the Euclidean position uncertainty of newly observed environmental features was not Gaussian distributed, due to the non-linearities associated with bearing-only observations.

In an indoor environment with close proximity features and fast camera motion, most environmental features will move out of the field of view of the camera in a relatively short period of time. Those features will nevertheless provide information about camera motion and delayed feature initialization approaches might fail to exploit such information. A new parametrization for feature positions that overcame this limitation was presented by

Civera et al. [65]. Known as the “inverse depth” parametrization, this approach represents a feature location by a vector pointing toward it combined with the inverse of the distance to the feature along that vector. Such a parametrization provides the means to capture the complete uncertainty of the depth of a feature when it is first observed using a Gaussian probability distribution. This facilitates un-delayed feature initialization and alleviates the need to bootstrap the VSLAM algorithms with known features. Due to these advantages, the algorithm presented by Civera et al. [65] will be used throughout the rest of this thesis as the default VSLAM algorithm.

4.2.2 Visual-Inertial Fusion

A tutorial level introduction to visual-inertial fusion along with a summary of applications was presented by Corke et al. [66]. There, the authors differentiate between loosely-coupled and tightly-coupled VIF systems. The former is a combination of two filters; one to extract information about the camera pose from the images and another to fuse that information with inertial measurements. The latter combines these two filters into one coherent estimator that fuses direct visual measurements such as pixel positions of environmental features with inertial measurements. Loosely-coupled formulations are modular and easier to design. Tightly-coupled VIF designs are more challenging to implement but are more accurate and robust.

Of the two categories, loosely-coupled VIF has received significant attention of the research community in the recent past with the advent of “black-box” VSLAM algorithms such as PTAM [61]. As PTAM pose estimates are only accurate up-to-a-scale, other sensors such as accelerometers or air-speed sensors have to be employed to derive metric scale pose estimates. Weiss et al. [67] proposed a set-up where images were processed using a variation of PTAM to obtain the camera pose. This pose was then combined with accelerometer and gyroscope measurements in an EKF to estimate the pose of a quadrotor MAV. A similar setup was presented by Nützi et al. [13] but with the addition of an air pressure sensor. A similar approach was followed by Sa et al. [68], where measurements from a downward facing sonar is combined with PTAM altitude estimates to derive metric scale

motion estimates. While Sa et al. [68] claims accuracies in the order of a few centimetres, it is important to note that their experiments only considered a quadrotor MAV in hovering, which is the ideal operating scenario for PTAM. Real indoor flights in unknown environments would encounter frequent linear accelerations on the order of a few tens of meters per seconds squared and rotational rates on the order of few tens of degrees per second. Later in this chapter it will be shown that PTAM like VSLAM algorithms that rely on constant velocity motion models fail to produce consistent pose estimates when the camera motion is not smooth.

Tightly-coupled VIF implementations are less common in literature because of their increased complexity. Mirzaei and Roumeliotis [42] presented an iterated EKF design to fuse visual and inertial measurements with the aim of estimating the inter-sensor calibration parameters and camera pose. A similar approach that made use of an unscented Kalman filter was presented by Kelly and Sukhatme [38]. However, in both these approaches, the focus was on estimating the calibration parameters. Therefore, the motion of the camera was restricted such that it observed a specific set of environmental features in all images. A similar formulation by Jones and Soatto [69], included experimental results that span long indoor and outdoor trajectories. However, the lack of accurate ground truth inhibited a thorough evaluation of the estimation errors. Kim and Sukkarieh [70] presented a tightly-coupled implementation of bearing-only inertial SLAM that can be used to estimate the pose of fixed wing aerial vehicle along with the position of a set of artificial landmarks placed on the ground. The distance to the features at the initialization was calculated by employing the known dimensions of the artificial features. Bryson and Sukkarieh [64] detailed a similar implementation but resorted to a delayed initialization of the features assuming their dimensions are unknown. As discussed before, such delayed initialization schemes are unsuitable for MAVs that operate indoors in close proximity to features.

None of the above loosely-coupled or tightly-coupled approaches make use of the specific dynamic characteristics of the quadrotor to aid the estimation process. An example of incorporating the dynamic model into a loosely-coupled VIF algorithm was presented by Engel et al. [71]. They made use of the quadrotor MAV dynamic equations and inertial measurements to derive metric scale velocity estimates. These velocity estimates were later combined with PTAM velocity estimates in a maximum likelihood estimator to derive the

scale of PTAM position estimates. The metric scale position estimates were then fused again with inertial measurements within an EKF, while ignoring the correlation between the two information sources. This could result in overconfident state estimates, but no comparison against ground truth states were provided in [71] to examine whether this was indeed the case. Furthermore, Engel et al. [71] did not evaluate the observability of the proposed VIF algorithm to establish whether it was capable of producing consistent state estimates.

4.2.3 Observability of Visual-Inertial Fusion

A theoretical analysis of the observability properties of a visual-inertial fusion system is of critical importance because of the inherent scale ambiguities present in monocular VSLAM algorithms. Several authors have applied the locally weak observability analysis tools proposed by Hermann and Krener [40] to analyse the observability of VIF algorithms. As detailed in the following, they have analysed VIF problems of varying degrees of complexity and have demonstrated that the more information that needs to be extracted from the fusion of the visual and inertial information, the more stricter the constraint that need to be placed on the motion of the platform under consideration to ensure observability.

Martinelli [72] analysed the problem of deriving closed-form solutions for the pose of a camera affixed with an IMU. He showed that if inter-sensor calibration parameters and gravity vector are known, then all considered states are only observable up to a scale factor if the IMU-camera system is moving at a constant velocity. Mirzaei and Roumeliotis [42] investigated this problem further to estimate the unknown transformation between the camera and IMU in addition to the pose of the camera with an EKF. An observability analysis revealed that all states are observable if the IMU-camera system is undergoing a rotation around an axis that is not parallel to any of the three principal axes of the IMU coordinate frame (angular velocity constraint). Kelly and Sukhatme [38] further extended this approach by also incorporating the gravity vector as a state that needs to be estimated. They showed that all considered states are observable given that the IMU-camera system undergoes linear accelerations along an axis that is not parallel to any of the three principal axes of the IMU coordinate frame (linear acceleration constraint),

TABLE 4.1: Results of observability analyses for different VIF formulations

Analysis	Estimated States	Constraints on motion
Martinelli [72]	camera pose	non-zero acceleration
Mirzaei and Roumeliotis [42]	camera pose camera-IMU extrinsics	angular velocity constraint
Kelly and Sukhatme [38]	camera pose camera-IMU extrinsics gravity vector	angular velocity constraint linear acceleration constraint
Weiss et al. [67]	camera attitude camera velocity camera-IMU extrinsics	angular velocity constraint linear acceleration constraint

in addition to satisfying the angular velocity constraint mentioned above. Weiss et al. [67] employed a camera to obtain a scaled velocity estimate for a MAV and proposed to combine that with the inertial sensor measurements in an EKF to obtain metric scale pose estimates for the MAV. They also included the inter-sensor calibration parameters in the state estimator and claimed that all states except for the MAV position and yaw angle are observable when the camera-IMU system supports both the linear acceleration and angular velocity constraints. However, they did not present the details of the analysis upon which this claim was made.

A table summarising these analyses and their respective motion constraints is presented in Table 4.1. Clearly, all of these existing approaches for visual-inertial fusion require that at least the angular velocity or the linear acceleration constraint be satisfied to ensure observability. It is difficult to satisfy either of these constraints during the normal operation of a quadrotor MAV. Experiments performed by Weiss et al. [67] demonstrated that these constraints cannot be satisfied to a level that facilitates well conditioned estimates - even when the quadrotor is moved by hand. In contrast, Section 4.4 of this thesis shows that, for a quadrotor MAV, the observability can be made independent of these constraints on trajectory by making use of platform specific dynamic characteristics to aid the state estimation.

4.3 Visual-Inertial Fusion Filter Design

Visual-inertial fusion algorithms can be broadly categorized based on how the overall filter is structured, resulting in two main categories; loosely-coupled VIF and tightly-coupled VIF. This section presents the design of two loosely-coupled VIF algorithms. The first algorithm makes use of only the visual and inertial information. Estimators based on this algorithm [67] or its variations [73] have been employed previously for state estimation of quadrotor MAVs. It provides an example of how VIF algorithms are designed in the absence of the additional information provided by the quadrotor MAV dynamics and is included here as a benchmark to study the improvements brought about by model-aiding. For ease of reference, in this thesis it is referred to as the “Conventional Visual Inertial Fusion” (C-VIF) algorithm.

The second algorithm presented in this section proposes to extend the C-VIF algorithm by employing the unique dynamic characteristics of the quadrotor MAV. Similar to the model-aided inertial estimator design of Chapter 3, this involves augmenting the process model of the state estimator with the quadrotor MAV dynamic model and also incorporating the biased velocity measurements obtained from the accelerometer into the measurement model. For ease of reference, this proposed algorithm is termed as the “Model-Aided Visual Inertial Fusion” (MA-VIF) algorithm in this thesis.

All VIF algorithms analysed in this chapter require the images gathered from a camera onboard the quadrotor MAV. It is assumed that the coordinate system $\{C\}$ of this camera coincides with the body coordinate frame $\{B\}$. Any misalignment between the camera and the body frame can be calculated, and accounted for with the help of accelerometer measurements and calibration images captured by the camera [47]. It is also assumed that the $\{B_0\}$, which is set to be $\{B\}$ at the start of the estimation algorithm, is aligned with the inertial coordinate frame, $\{E\}$. As the position and heading of $\{E\}$ can be chosen arbitrarily, this amounts to ensuring that the vertical axis of $\{C\}$ is aligned with gravity. In practice, this can be achieved by placing the quadrotor MAV on a level surface prior to initializing the state estimator. Any misalignment of the vertical axis of $\{B_0\}$ with gravity will affect the accuracy of the state estimates. However, this misalignment is

assumed small in this thesis to simplify the observability analysis of VIF designs. Fig. 4.1 illustrates the coordinate frame assignment.

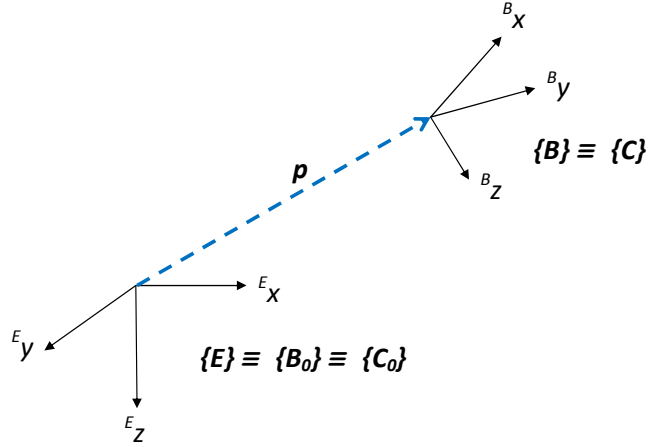


FIGURE 4.1: Coordinate frame assignment for VIF

Both the C-VIF and the proposed MA-VIF adhere to the same structure shown in Fig. 4.2. There are two separate estimators in this set-up, one feeding into the other. The VSLAM module accepts the images from the camera onboard the quadrotor MAV as inputs. This module can be implemented with either an optimization based or filter based VSLAM algorithm discussed in Section 4.2. An open-source implementation [45] of the Inverse-Depth (ID) monocular SLAM algorithm was used as the default VSLAM module for VIF algorithms discussed in this thesis. More details of this implementation can be found in Appendix B.

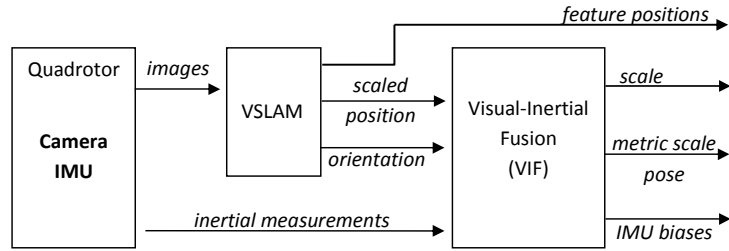


FIGURE 4.2: Structure of a loosely-coupled Visual-inertial fusion set-up.

The VSLAM module outputs an estimate of the position and orientation of $\{C\}$ with respect to $\{E\}$ along with their uncertainties. Due to the projective nature of a monocular camera, the VSLAM position estimates are only accurate up to an unknown scale. The output of the VSLAM module can be modelled as:

$$\mathbf{h}_{vp} = \lambda^e \mathbf{p} + \boldsymbol{\eta}_p \quad (4.1a)$$

$$\mathbf{h}_{vo} = \boldsymbol{\Theta} + \boldsymbol{\eta}_o \quad (4.1b)$$

where λ is an unknown constant and $\boldsymbol{\eta}_p, \boldsymbol{\eta}_o$ are 3×1 vectors of WGN variables with $E[[\boldsymbol{\eta}_p \boldsymbol{\eta}_o][\boldsymbol{\eta}_p \boldsymbol{\eta}_o]^T] = P_{rr}$ is the pose error covariance of the VSLAM module.

The analysis here focuses on the case where the quadrotor MAV is operated in a feature rich indoor environment with a maximum operating time of about 10-15 minutes.¹ In such a setting, frequent re-visiting of previously seen features occur and thus a state-of-the-art VSLAM system can be expected to produce pose estimates without notable drift, thus validating use of Equation 4.1.

The other input to the visual-inertial fusion module of Fig. 4.2 are the IMU measurements. The measurement equations for the accelerometers and gyroscopes were presented in Equation 2.15 and Equation 2.14 respectively. The full state vector for the VIF is given by $\mathbf{X} = [\mathbf{p} \ \mathbf{v} \ \lambda \ \boldsymbol{\Theta} \ \boldsymbol{\Omega} \ \boldsymbol{\beta}_a \ \boldsymbol{\beta}_g]^T$ where λ was included to account for the unknown scale of VSLAM pose estimates.

It is important to note that λ here is not the same as the absolute scale of the VSLAM algorithm, which is the scale of the estimated map to the true map. The VIF algorithm will drive λ estimate such that the error between the true and estimated position are minimised. If the output of the VSLAM algorithm is ideal, then all position estimates are scaled by the absolute scale value, and in that case, λ will converge to the absolute scale. However, if the VSLAM estimates become inconsistent due to reasons such as infrequent re-visitation of environmental landmarks, then λ will adjust to account for the errors in VSLAM estimates given that other sources of information about the motion of the camera is available. In this case it may deviate from the true absolute scale of the VSLAM

¹This is the typical operating time of a state-of-the-art quadrotor MAV.

algorithm. As such, the dynamics of λ is not deterministic. However, for the purpose of estimator design, it is reasonable to assume that λ is a slowly varying parameter [74].

The EKF based estimator design requires a process model that describes the time evolution of the states. The time derivative of the position, orientation and velocity states of the VIF state vector \mathbf{X} is governed by the rigid body dynamics equations introduced in Equation 2.4. As λ and IMU biases are assumed to be slowly varying, their time derivatives are modelled as WGN variables of suitable magnitudes. Combining these, the process model for a generic VIF algorithm can be obtained:

$$\dot{\mathbf{X}} = \begin{bmatrix} {}^E\dot{\mathbf{p}} \\ {}^E\dot{\mathbf{v}} \\ \dot{\lambda} \\ \dot{\Theta} \\ {}^B\dot{\Omega} \\ \dot{\beta}_a \\ \dot{\beta}_g \end{bmatrix} = \begin{bmatrix} {}^E\mathbf{v} \\ \mathbf{g} + \frac{1}{m} {}^E_B R {}^B\mathbf{F} \\ \eta_\lambda \\ \Xi {}^B\Omega \\ J^{-1}({}^B\mathbf{M} - {}^B\Omega \times J {}^B\Omega) \\ \eta_{\beta a} \\ \eta_{\beta g} \end{bmatrix} \quad (4.2)$$

Expressions for external forces ${}^B\mathbf{F}$ and moments ${}^B\mathbf{M}$ are required to realise an actual EKF implementation based on this process model. The C-VIF and the MA-VIF achieves this in different ways, as detailed in the following.

4.3.1 Conventional Visual Inertial Fusion

Equations relating the external forces, ${}^B\mathbf{F}$ and ${}^B\mathbf{M}$, and the system state are, in general, not available in a form suitable for use in state estimation for many robotic systems. Conventionally, VIF algorithm designs have circumvented the need for explicit dynamic models by using inertial sensor measurements to replace the dynamics in Equation 4.2 with rigid body kinematics. By considering the accelerometer and gyroscope measurement

equations of Chapter 2, the following expressions for ${}^E\dot{\boldsymbol{v}}$ and $\dot{\Theta}$ can be derived:

$${}^E\dot{\boldsymbol{v}} = {}_B^E R({}^B\boldsymbol{a} - \boldsymbol{\beta}_a - \boldsymbol{\eta}_a) + \boldsymbol{g} \quad (4.3)$$

$$\dot{\Theta} = \Xi({}^B\boldsymbol{\omega}_g - \boldsymbol{\beta}_g + \boldsymbol{\eta}_g). \quad (4.4)$$

The process equation for the C-VIF can be derived by substituting Equations 4.3 and 4.4 in Equation 4.2 for ${}^E\dot{\boldsymbol{v}}$ and $\dot{\Theta}$ respectively. The accelerometer and gyroscope measurements in these equations are then treated as inputs that drive the C-VIF process model. This substitution also means that ${}^B\Omega$ can be removed from the state vector as the expression for $\dot{\Theta}$ is independent of ${}^B\Omega$. The VSLAM pose estimates are treated as measurements from the perspective of the C-VIF and were given by Equation 4.1. The process and measurement equations for the C-VIF are summarised in Table 4.2.

TABLE 4.2: Conventional Visual-Inertial Fusion Estimator

Process Equations	
${}^E\dot{\boldsymbol{p}}$	${}^E\boldsymbol{v}$
$=$	
${}^E\dot{\boldsymbol{v}}$	${}_B^E R({}^B\boldsymbol{a} - \boldsymbol{\beta}_a - \boldsymbol{\eta}_a) + \boldsymbol{g}$
$\dot{\lambda}$	η_λ
$\dot{\Theta}$	$\Xi({}^B\boldsymbol{\omega}_g - \boldsymbol{\beta}_g + \boldsymbol{\eta}_g)$
$\dot{\boldsymbol{\beta}}_a$	$\boldsymbol{\eta}_{\beta a}$
$\dot{\boldsymbol{\beta}}_g$	$\boldsymbol{\eta}_{\beta g}$
Measurement Equations	
$\boldsymbol{h}_{vp} = \lambda {}^e \boldsymbol{p} + \boldsymbol{\eta}_p$	
$\boldsymbol{h}_{vo} = \boldsymbol{\Theta} + \boldsymbol{\eta}_o$	

4.3.2 Model-Aided Visual Inertial Fusion

The MA-VIF formulation proposed here extends the C-VIF by explicitly modelling some of the dynamic equations in Equation 4.2. For this, it makes use of the equation for

the evolution of the body frame velocity which presented in Equation 3.13. In-order to incorporate this equation into the process model, the velocity of the quadrotor MAV in the state vector \mathbf{X} is expressed in the $\{B\}$ instead of $\{E\}$. Similar to the C-VIF, MA-VIF also makes use of the gyroscope measurement equation to describe the time evolution of Θ .

The MA-VIF makes use of the same VSLAM measurement equations as the C-VIF. In addition, it makes use of the measurements of ${}^B\mathbf{x}$ and ${}^B\mathbf{y}$ accelerometers. The equations for these were derived in Section 3.3.2. Table 4.3 summarises the process and measurement equations for the MA-VIF.

TABLE 4.3: Model-Aided Visual-Inertial Fusion Estimator

Process Equations

$$\begin{bmatrix} {}^E\dot{\mathbf{p}} \\ {}^B\dot{\mathbf{v}} \\ \dot{\lambda} \\ \dot{\Theta} \\ \dot{\beta}_a \\ \dot{\beta}_g \end{bmatrix} = \begin{bmatrix} {}^ER{}^B\mathbf{v} \\ {}^ER\mathbf{g} + ({}^Ba_z - \beta_{az})\mathbf{e}_3 - \bar{D}_L {}^B\mathbf{v} + \boldsymbol{\eta}_v \\ \eta_\lambda \\ -\Xi(\beta_g + \boldsymbol{\eta}_g) \\ \boldsymbol{\eta}_{\beta a} \\ \boldsymbol{\eta}_{\beta g} \end{bmatrix}$$

Measurement Equations

$$\mathbf{h}_i = \begin{bmatrix} {}^B\mathbf{a}_x \\ {}^B\mathbf{a}_y \end{bmatrix} = \Upsilon(\bar{D}_L {}^B\mathbf{v} + \boldsymbol{\beta}_a + \boldsymbol{\eta}_a)$$

$$\mathbf{h}_{vp} = \lambda {}^E\mathbf{p} + \boldsymbol{\eta}_p$$

$$\mathbf{h}_{vo} = \Theta + \boldsymbol{\eta}_o$$

4.4 Observability of Visual-Inertial Fusion

4.4.1 Observability of C-VIF

To apply the Lie derivative based observability analysis the process equation need to be expressed in the input linear form introduced in 2.7. Rearranging the C-VIF process equation from Table 4.2 results in:

$$\begin{bmatrix} {}^E\dot{\boldsymbol{p}} \\ {}^E\dot{\boldsymbol{v}} \\ \dot{\lambda} \\ \dot{\boldsymbol{\Theta}} \\ \dot{\boldsymbol{\beta}_a} \\ \dot{\boldsymbol{\beta}_g} \end{bmatrix} = \underbrace{\begin{bmatrix} {}^E\boldsymbol{v} \\ -\frac{{}^ER}{B}\boldsymbol{\beta}_a + \boldsymbol{g} - \boldsymbol{\eta}_a \\ \eta_\lambda \\ \Xi(-\boldsymbol{\beta}_g + \boldsymbol{\eta}_g) \\ \boldsymbol{\eta}_{\beta a} \\ \boldsymbol{\eta}_{\beta g} \end{bmatrix}}_{\boldsymbol{l}_0} + \underbrace{\begin{bmatrix} \mathbf{0}_{3 \times 1} \\ \frac{{}^ER}{B} \\ 0 \\ \mathbf{0}_{3 \times 1} \\ \mathbf{0}_{3 \times 1} \\ \mathbf{0}_{3 \times 1} \end{bmatrix}}_{\boldsymbol{l}_1} {}^B\boldsymbol{a} + \underbrace{\begin{bmatrix} \mathbf{0}_{3 \times 1} \\ \mathbf{0}_{3 \times 1} \\ 0 \\ \Xi \\ \mathbf{0}_{3 \times 1} \\ \mathbf{0}_{3 \times 1} \end{bmatrix}}_{\boldsymbol{l}_2} {}^B\boldsymbol{\omega}_g \quad (4.5)$$

where \boldsymbol{l}_1 is a compact representations of three vectors of dimensions 16×1 according to:

$$\boldsymbol{l}_1 {}^B\boldsymbol{a} = \boldsymbol{l}_{11} {}^B\boldsymbol{a}_x + \boldsymbol{l}_{12} {}^B\boldsymbol{a}_y + \boldsymbol{l}_{13} {}^B\boldsymbol{a}_z$$

where $\boldsymbol{l}_{11}, \boldsymbol{l}_{12}, \boldsymbol{l}_{13}$ are, respectively, the first, second and third columns of \boldsymbol{l}_1 . Similarly \boldsymbol{l}_2 consists of the three column vectors $\boldsymbol{l}_{21}, \boldsymbol{l}_{22}, \boldsymbol{l}_{23}$.

The observability of C-VIF is analysed for two different scenarios.

1. Observability of the C-VIF when the acceleration is non-zero, i.e. ${}^E\dot{\boldsymbol{v}} \neq 0$.
2. Observability of the C-VIF when the acceleration is zero, i.e. ${}^E\dot{\boldsymbol{v}} = 0$.

For the first case, the C-VIF formulation is governed by Equation 4.5 and the measurement equations in Table 4.2 with zero noise terms.

Lemma 4.1. *The C-VIF formulation defined by Equations (4.5) and (4.1) is locally weakly-observable when ${}^E\dot{\boldsymbol{v}} \neq 0$.*

Proof. Consider the following observability matrix \mathcal{O}_1 constructed from the Lie derivatives of the system described by equations (4.5) and (4.1).

$$\begin{aligned}\mathcal{O}_1 &= [\nabla L^0 h_{vp}(x) \ \nabla L^0 h_{vo}(x) \ \nabla L_{l_0}^1 h_{vp}(x) \dots \\ &\quad \nabla L_{l_0}^1 h_{vo}(x) \ \nabla L_{l_0}^2 h_{vp}(x) \ \nabla L_{l_{11}l_0}^2 h_{vp}(x)]^T \\ &= \begin{bmatrix} \lambda \mathbf{I}_3 & \mathbf{0}_{3 \times 3} & {}^E\mathbf{p} & \mathbf{0}_{3 \times 3} & \mathbf{0}_{3 \times 3} & \mathbf{0}_{3 \times 3} \\ \mathbf{0}_{3 \times 3} & \mathbf{0}_{3 \times 3} & \mathbf{0}_{3 \times 1} & \mathbf{I}_3 & \mathbf{0}_{3 \times 3} & \mathbf{0}_{3 \times 3} \\ \mathbf{0}_{3 \times 3} & \lambda \mathbf{I}_3 & {}^E\mathbf{v} & \mathbf{0}_{3 \times 3} & \mathbf{0}_{3 \times 3} & \mathbf{0}_{3 \times 3} \\ \mathbf{0}_{3 \times 3} & \mathbf{0}_{3 \times 3} & \mathbf{0}_{3 \times 1} & \mathbf{D}_1 & \mathbf{0}_{3 \times 3} & -\Xi \\ \mathbf{0}_{3 \times 3} & \mathbf{0}_{3 \times 3} & \mathbf{D}_2 & \mathbf{D}_3 & -\lambda R & \mathbf{0}_{3 \times 3} \\ \mathbf{0}_{3 \times 3} & \mathbf{0}_{3 \times 3} & R_1 & \mathbf{D}_4 & \mathbf{0}_{3 \times 3} & \mathbf{0}_{3 \times 3} \end{bmatrix}\end{aligned}$$

where ${}^B_E R$ has been replaced with R for clarity and $\mathbf{D}_1, \mathbf{D}_2, \mathbf{D}_3, \mathbf{D}_4$ are functions of $\lambda, \Theta, \beta_a, \beta_g$. Also R_1 is the first column of R .

Block Gaussian elimination can be used to derive the rank of \mathcal{O}_1 . First noting that $\lambda > 0$, row blocks one, three and five are divided by λ . Then, noting that block $\mathcal{O}_1(2,4)$ is full rank, remaining non-zero elements from column block four can be eliminated. Also R is full rank so it is possible to multiply row block five and six by R^{-1} . Ξ is full rank for any Θ so row block four can be multiplied by $-\Xi^{-1}$ to obtain:

$$\mathcal{O}_1 \rightarrow \begin{bmatrix} \mathbf{I}_3 & \mathbf{0}_{3 \times 3} & {}^E\mathbf{p} & \mathbf{0}_{3 \times 3} & \mathbf{0}_{3 \times 3} & \mathbf{0}_{3 \times 3} \\ \mathbf{0}_{3 \times 3} & \mathbf{0}_{3 \times 3} & \mathbf{0}_{3 \times 1} & \mathbf{I}_3 & \mathbf{0}_{3 \times 3} & \mathbf{0}_{3 \times 3} \\ \mathbf{0}_{3 \times 3} & \mathbf{I}_3 & {}^E\mathbf{v} & \mathbf{0}_{3 \times 3} & \mathbf{0}_{3 \times 3} & \mathbf{0}_{3 \times 3} \\ \mathbf{0}_{3 \times 3} & \mathbf{0}_{3 \times 3} & \mathbf{0}_{3 \times 1} & \mathbf{0}_{3 \times 3} & \mathbf{0}_{3 \times 3} & \mathbf{I}_3 \\ \mathbf{0}_{3 \times 3} & \mathbf{0}_{3 \times 3} & \mathbf{D}_2 & \mathbf{0}_{3 \times 3} & \mathbf{I}_3 & \mathbf{0}_{3 \times 3} \\ \mathbf{0}_{3 \times 3} & \mathbf{0}_{3 \times 3} & \mathbf{e}_1 & \mathbf{0}_{3 \times 3} & \mathbf{0}_{3 \times 3} & \mathbf{0}_{3 \times 3} \end{bmatrix}.$$

Noting that $\mathbf{e}_1 = [1 \ 0 \ 0]^T$, and also noting that all other entries in last row is zero, all non-zero entries in column block three can be eliminated to obtain:

$$\mathcal{O}_1 \rightarrow \begin{bmatrix} \mathbf{I}_3 & \mathbf{0}_{3 \times 3} & \mathbf{0}_{3 \times 1} & \mathbf{0}_{3 \times 3} & \mathbf{0}_{3 \times 3} & \mathbf{0}_{3 \times 3} \\ \mathbf{0}_{3 \times 3} & \mathbf{0}_{3 \times 3} & \mathbf{0}_{3 \times 1} & \mathbf{I}_3 & \mathbf{0}_{3 \times 3} & \mathbf{0}_{3 \times 3} \\ \mathbf{0}_{3 \times 3} & \mathbf{I}_3 & \mathbf{0}_{3 \times 1} & \mathbf{0}_{3 \times 3} & \mathbf{0}_{3 \times 3} & \mathbf{0}_{3 \times 3} \\ \mathbf{0}_{3 \times 3} & \mathbf{0}_{3 \times 3} & \mathbf{0}_{3 \times 1} & \mathbf{0}_{3 \times 3} & \mathbf{0}_{3 \times 3} & \mathbf{I}_3 \\ \mathbf{0}_{3 \times 3} & \mathbf{0}_{3 \times 3} & \mathbf{0}_{3 \times 1} & \mathbf{0}_{3 \times 3} & \mathbf{I}_3 & \mathbf{0}_{3 \times 3} \\ \mathbf{0}_{3 \times 3} & \mathbf{0}_{3 \times 3} & \mathbf{e}_1 & \mathbf{0}_{3 \times 3} & \mathbf{0}_{3 \times 3} & \mathbf{0}_{3 \times 3} \end{bmatrix}.$$

which has full column rank. Thus it is possible to conclude that the C-VIF formulation is locally weakly-observable when ${}^E\dot{\mathbf{v}} \neq 0$. Note that a similar result can be obtained by using either $\nabla L_{l_{12}l_0}^2 h_{vp}(x)$ or $\nabla L_{l_{13}l_0}^2 h_{vp}(x)$ instead of $\nabla L_{l_{11}l_0}^2 h_{vp}(x)$ for the last row of \mathcal{O}_1 . ■

For the second case, the process equation can be obtained by setting ${}^E\dot{\mathbf{v}} = 0$ in Equations (4.5). There are conditions on the rotational kinematics that need to be enforced in Equations (4.5) to satisfy the condition ${}^E\dot{\mathbf{v}} = 0$. Fortunately, there is no need to explicitly model these conditions because the translational and angular kinematics of Equation 4.5 can be separated when ${}^E\dot{\mathbf{v}} = 0$. The process equation related to the translational kinematics therefore becomes:

$$\begin{bmatrix} {}^E\dot{\mathbf{p}} \\ {}^E\dot{\mathbf{v}} \\ \dot{\lambda} \end{bmatrix} = \underbrace{\begin{bmatrix} {}^E\mathbf{v} \\ \mathbf{0}_{3 \times 1} \\ 0 \end{bmatrix}}_{j_0} \quad (4.6)$$

with noise terms set to zero for the observability analysis. The accelerometer bias was removed from the state vector, as the accelerometer measurement is no longer required to complete the translational kinematics. The VSLAM measurement equation related to the translational kinematics is given by Equation 4.1a, after setting noise terms to zero.

Lemma 4.2. *The C-VIF formulation defined by Equations (4.6) and (4.1a) is locally unobservable.*

Proof. Considering all non-trivial Lie derivatives of the considered system the following observability matrix \mathcal{O}_2 can be constructed:

$$\begin{aligned}\mathcal{O}_2 &= [\nabla L^0 h_{vp}(x) \ \nabla L_{j_0}^1 h_{vp}(x)]^T \\ &= \begin{bmatrix} \lambda I_3 & \mathbf{0}_{3 \times 3} & {}^E\boldsymbol{p} \\ \mathbf{0}_{3 \times 3} & \lambda I_3 & {}^E\boldsymbol{v} \end{bmatrix}.\end{aligned}$$

All gradients of Lie derivatives not considered for \mathcal{O}_2 are identically zero. The rank of \mathcal{O}_2 is at most 6, whereas the dimension of the considered system is 7. Thus it can be deduced that the system defined by Equations (4.6) and (4.1a) is not locally weakly observable. The local unobservability can be deduced from this result as the local weak observability is a necessary condition for local observability. ■

By extension of Lemma 4.2, the following Corollary can be obtained.

Corollary 4.3. *The C-VIF formulation defined by Equations (4.5) and (4.1) is locally unobservable when ${}^E\dot{\boldsymbol{v}} = 0$.*

Proof. Lemma 4.2 considers the observability of part of the state in C-VIF formulation under the condition that ${}^E\dot{\boldsymbol{v}} \neq 0$. If a subset of the states is unobservable, then it follows that the full state vector of C-VIF formulation is also unobservable. ■

4.4.2 Observability of MA-VIF

Expressing the MA-VIF process equation from Table 4.3 in the input linear form results in:

$$\begin{bmatrix} {}^E\dot{\boldsymbol{p}} \\ {}^B\dot{\boldsymbol{v}} \\ \dot{\lambda} \\ \dot{\boldsymbol{\Theta}} \\ \dot{\boldsymbol{\beta}}_a \\ \dot{\boldsymbol{\beta}}_g \end{bmatrix} = \underbrace{\begin{bmatrix} {}^E R {}^B\boldsymbol{v} \\ {}^E R \boldsymbol{g} - \beta_{az} \mathbf{e}_3 - \bar{D}_L {}^B\boldsymbol{v} + \boldsymbol{\eta}_v \\ \eta_\lambda \\ -\Xi(\beta_g + \boldsymbol{\eta}_g) \\ \boldsymbol{\eta}_{\beta a} \\ \boldsymbol{\eta}_{\beta g} \end{bmatrix}}_{f_0} + \underbrace{\begin{bmatrix} \mathbf{0}_{3 \times 1} \\ {}^B a_z \mathbf{e}_3 \\ 0 \\ \Xi {}^B \boldsymbol{\omega}_g \\ \mathbf{0}_{3 \times 1} \\ \mathbf{0}_{3 \times 1} \end{bmatrix}}_{f_1}. \quad (4.7)$$

For the MA-VIF, the observability of the following two cases are analysed.

1. Observability of the MA-VIF when at least one of ${}^B v_x$ and ${}^B v_y$ is non-zero.
2. Observability of the MA-VIF when the quadrotor MAV is in hover.

For the first case, the following lemma can be stated.

Lemma 4.4. *The MA-VIF system defined by the process and measurement models of Table 4.3 is locally-weakly observable when at least one of ${}^B v_x$ and ${}^B v_y$ is non-zero.*

Proof. By considering the non-trivial Lie derivatives of up to second order, the following observability matrix can be constructed for the MA-VIF:

$$\begin{aligned} \mathcal{O}_3 &= [\nabla L^0 h_{vp}(x) \ \nabla L^0 h_{vo}(x) \ \nabla L_{f_0}^1 h_{vo}(x) \ \nabla L^0 h_i(x) \dots \\ &\quad \nabla L_{f_0}^1 h_{vp}(x) \ \nabla L_{f_0}^1 h_i(x) \ \nabla L_{f_0 f_0}^2 h_{vp}(x)]^T \\ &= \begin{bmatrix} \lambda I_3 & \mathbf{0}_{3 \times 3} & {}^e p & \mathbf{0}_{3 \times 3} & \mathbf{0}_{3 \times 3} & \mathbf{0}_{3 \times 3} \\ \mathbf{0}_{3 \times 3} & \mathbf{0}_{3 \times 3} & \mathbf{0}_{3 \times 1} & I_3 & \mathbf{0}_{3 \times 3} & \mathbf{0}_{3 \times 3} \\ \mathbf{0}_{3 \times 3} & \mathbf{0}_{3 \times 3} & \mathbf{0}_{3 \times 1} & C_1 & \mathbf{0}_{3 \times 3} & -\Xi \\ \mathbf{0}_{2 \times 3} & k_1 \Upsilon & \mathbf{0}_{2 \times 1} & \mathbf{0}_{2 \times 3} & \Upsilon & \mathbf{0}_{2 \times 3} \\ \mathbf{0}_{3 \times 3} & \lambda R & R {}^B v & C_2 & \mathbf{0}_{3 \times 3} & \mathbf{0}_{3 \times 3} \\ \mathbf{0}_{2 \times 3} & k_1^2 \Upsilon & \mathbf{0}_{2 \times 1} & C_3 & \mathbf{0}_{2 \times 3} & \mathbf{0}_{2 \times 3} \\ \mathbf{0}_{3 \times 3} & C_4 & C_5 & C_6 & -\lambda R \Gamma & C_7 \end{bmatrix} \quad (4.8) \end{aligned}$$

where ${}_E^B R$ has been replaced with R for clarity and $C_i, (i = 1 \dots 7)$ are functions of \mathbf{X} .

Block Gaussian elimination can be used to recover the rank of \mathcal{O}_3 .

First, given that $\lambda > 0$, row block one is divided by λ . Also since block $\mathcal{O}_3(2,4)$ is an identity matrix, all other non-zero entries in column block four can be eliminated. Rotational transformation matrix R is orthogonal and thus is always full rank. Therefore, row block four can be multiplied by R^{-1} . Similarly Ξ is always invertible for any Θ , so block $\mathcal{O}_3(3,6)$ can be multiplied by $-\Xi^{-1}$ to eliminate all non-zero entries in column block

6. Also, $k_1 \neq 0$ so row block five can be divided by k_1^2 to obtain:

$$\mathcal{O}_3 \rightarrow \begin{bmatrix} \mathbf{I}_3 & \mathbf{0}_{3 \times 3} & \frac{1}{\lambda} \mathbf{p} & \mathbf{0}_{3 \times 3} & \mathbf{0}_{3 \times 3} & \mathbf{0}_{3 \times 3} \\ \mathbf{0}_{3 \times 3} & \mathbf{0}_{3 \times 3} & \mathbf{0}_{3 \times 1} & \mathbf{I}_3 & \mathbf{0}_{3 \times 3} & \mathbf{0}_{3 \times 3} \\ \mathbf{0}_{3 \times 3} & \mathbf{0}_{3 \times 3} & \mathbf{0}_{3 \times 1} & \mathbf{0}_{3 \times 3} & \mathbf{0}_{3 \times 3} & \mathbf{I}_3 \\ \mathbf{0}_{2 \times 3} & k_1 \Upsilon & \mathbf{0}_{2 \times 1} & \mathbf{0}_{2 \times 3} & \Upsilon & \mathbf{0}_{2 \times 3} \\ \mathbf{0}_{3 \times 3} & \lambda \mathbf{I}_3 & {}^B \mathbf{v} & \mathbf{0}_{3 \times 3} & \mathbf{0}_{3 \times 3} & \mathbf{0}_{3 \times 3} \\ \mathbf{0}_{2 \times 3} & \Upsilon & \mathbf{0}_{2 \times 1} & \mathbf{0}_{2 \times 3} & \mathbf{0}_{2 \times 3} & \mathbf{0}_{2 \times 3} \\ \mathbf{0}_{3 \times 3} & \mathbf{C}_4 & \mathbf{C}_5 & \mathbf{0}_{3 \times 3} & \lambda R \Gamma & \mathbf{0}_{3 \times 3} \end{bmatrix}. \quad (4.9)$$

Now consider the following submatrix of (4.9)

$$\mathcal{O}_{(4:5,2:3)} = \begin{bmatrix} \lambda \mathbf{I}_3 & {}^B \mathbf{v} \\ \Upsilon & \mathbf{0}_{2 \times 1} \end{bmatrix} = \begin{bmatrix} \lambda & 0 & 0 & {}^B v_x \\ 0 & \lambda & 0 & {}^B v_y \\ 0 & 0 & \lambda & {}^B v_z \\ 1 & 0 & 0 & 0 \\ 0 & 1 & 0 & 0 \end{bmatrix}.$$

After two row operations and rearranging rows the following can be obtained:

$$\mathcal{O}_{(4:5,2:3)} \rightarrow \begin{bmatrix} 1 & 0 & 0 & 0 \\ 0 & 1 & 0 & 0 \\ 0 & 0 & \lambda & {}^B v_z \\ 0 & 0 & 0 & {}^B v_x \\ 0 & 0 & 0 & {}^B v_y \end{bmatrix}.$$

Clearly, $\mathcal{O}_{(4:5,2:3)}$ is of full column rank when at least one of ${}^B v_x$ and ${}^B v_y$ is non-zero.

Therefore all remaining non-zero entries in column blocks two and three of \mathcal{O}_3 can be eliminated. Finally multiplying the last row of \mathcal{O}_3 by $(-\lambda R)^{-1}$, removing all-zero rows

and rearranging rows the following can be obtained:

$$\mathcal{O}_3 \rightarrow \begin{bmatrix} \mathbf{I}_3 & \mathbf{0}_{3 \times 3} & \mathbf{0}_{3 \times 1} & \mathbf{0}_{3 \times 3} & \mathbf{0}_{3 \times 2} & \mathbf{0}_{3 \times 1} & \mathbf{0}_{3 \times 3} \\ \mathbf{0}_{3 \times 3} & \mathbf{0}_{3 \times 3} & \mathbf{0}_{3 \times 1} & \mathbf{I}_3 & \mathbf{0}_{3 \times 2} & \mathbf{0}_{3 \times 1} & \mathbf{0}_{3 \times 3} \\ \mathbf{0}_{3 \times 3} & \mathbf{0}_{3 \times 3} & \mathbf{0}_{3 \times 1} & \mathbf{0}_{3 \times 3} & \mathbf{0}_{3 \times 2} & \mathbf{0}_{3 \times 1} & \mathbf{I}_3 \\ \mathbf{0}_{2 \times 3} & \mathbf{0}_{2 \times 3} & \mathbf{0}_{2 \times 1} & \mathbf{0}_{2 \times 3} & \mathbf{I}_2 & \mathbf{0}_{2 \times 1} & \mathbf{0}_{2 \times 3} \\ \mathbf{0}_{3 \times 3} & \mathbf{I}_3 & \mathbf{0}_{3 \times 1} & \mathbf{0}_{3 \times 3} & \mathbf{0}_{3 \times 2} & \mathbf{0}_{3 \times 1} & \mathbf{0}_{3 \times 3} \\ \mathbf{0}_{1 \times 3} & \mathbf{0}_{1 \times 3} & 1 & \mathbf{0}_{1 \times 3} & \mathbf{0}_{1 \times 2} & 0 & \mathbf{0}_{1 \times 3} \\ \mathbf{0}_{1 \times 3} & \mathbf{0}_{1 \times 3} & 0 & \mathbf{0}_{1 \times 3} & \mathbf{0}_{1 \times 2} & 1 & \mathbf{0}_{1 \times 3} \end{bmatrix}$$

which has full column rank. Thus it is possible to conclude that the MA-VIF formulation is locally weakly observable when at least one of ${}^B v_x$ and ${}^B v_y$ is non-zero. ■

The second case analyses the observability of the MA-VIF when the quadrotor MAV is hovering. In this case ${}^B \dot{\mathbf{v}} = {}^B \mathbf{v} = \mathbf{0}_{3 \times 1}$ and $\phi = \theta = 0$. For hovering, the following lemma holds.

Lemma 4.5. *The MA-VIF system is locally unobservable when the quadrotor MAV is hovering.*

Proof. Dynamics of hovering obtained by enforcing the above conditions on the process and measurement models of Table 4.3. As before, under these conditions, it is possible to separate the translational and rotational kinematics of Equation 4.7. Considering only the translational kinematics:

$$\begin{bmatrix} {}^e \dot{\mathbf{p}} \\ {}^B \dot{\mathbf{v}} \\ \dot{\lambda} \\ \Upsilon \dot{\beta}_a \end{bmatrix} = \begin{bmatrix} \mathbf{0}_{3 \times 1} \\ \mathbf{0}_{3 \times 1} \\ 0 \\ \mathbf{0}_{2 \times 1} \end{bmatrix}. \quad (4.10)$$

Note that only the biases of x, y accelerometers are considered as the measurement of the z axis accelerometer is not used. The measurement equations for accelerometers and VSLAM

estimates remain the same as in Table 4.3. Considering all non-trivial Lie derivatives of this system, the following observability matrix can be constructed:

$$\begin{aligned}\mathcal{O}_4 &= [\nabla L^0 h_{vp}(x) \quad \nabla L^0 h_i(x)]^T \\ &= \begin{bmatrix} \lambda I_3 & \mathbf{0}_{3 \times 3} & {}^E p & \mathbf{0}_{3 \times 3} \\ \mathbf{0}_{2 \times 3} & k_1 \Upsilon & \mathbf{0}_{2 \times 1} & \Upsilon \end{bmatrix}.\end{aligned}$$

The rank of \mathcal{O}_4 is, at most, 5 whereas the considered system is 7 dimensional. Therefore, the system under consideration is locally weakly unobservable and by extension, the MA-VIF is locally weakly unobservable under hovering conditions. The local unobservability can be deduced from this result as the local weak observability is a necessary condition for local observability. ■

4.4.3 Discussion

As both the C-VIF and the MA-VIF systems are observable, the equations in Tables 4.2 and 4.3 can be combined with the EKF mechanization equations of Table 2.1 to design state estimators based on those systems. However, since their observability was dependent on different constraints, it can be expected that the C-VIF and MA-VIF formulations would produce different estimation accuracies.

The observability of the conventional formulation of VIF (C-VIF) depends on the quadrotor maintaining a non-zero acceleration. The need to maintain a non-zero acceleration imposes a rather restrictive condition on the flight pattern of the quadrotor and may not be easily satisfied in practice. Thus, the estimates from the C-VIF formulation are likely to be poor during most manoeuvres. Weiss et al. [67] reported encountering this in experiments.

On the other hand, the proposed model-aided formulation (MA-VIF) is guaranteed to be observable whenever the quadrotor MAV is moving in either of ${}^b x$, ${}^b y$ directions. This is a more relaxed condition than what is required for the C-VIF. Therefore, in practice,

the MA-VIF can be expected to produce estimates which are better conditioned than the C-VIF for all possible manoeuvres. The MA-VIF also allows for extra freedom in planning MAV trajectories, which can now be employed to achieve other critical objectives such as minimizing energy usage.

Both systems are observable only if both the scale of the VSLAM estimates and the sensor biases are considered fixed parameters, albeit unknown. In practice, both the scale and biases do tend to drift slowly with time. Local weak observability implies that the current state of the system can be distinguished from its immediate neighbourhood of state subspace using the measurements and control inputs obtained during a relatively short timespan centred on the current state [40]. Therefore, given that both the C-VIF and MA-VIF are locally weakly observable, it is reasonable to assume that they remain observable even with slow variations of biases and scale. Simulation results presented in Section 4.5 serves to validate this assumption.

The following sections provide a comparison between the performance of C-VIF and MA-VIF as well as on the impact of scale and bias drift, through computer simulations and experiments.

4.5 Simulations of C-VIF and MA-VIF

To further verify the observability properties of both the conventional formulation of VIF (C-VIF) and the proposed model-aided formulation (MA-VIF), a set of simulations were performed using the simulation set-up presented in Chapter 2. As detailed there, this set-up made use of the inverse-depth monocular SLAM algorithm by Civera et al. [45] to produce VSLAM estimates. As all simulations resulted in similar results, only a representative example is presented here.

In this simulation the quadrotor MAV was commanded to take-off and travel along a square of size approximately 200×120 meters, while keeping a constant heading and returning to the start position in the end. For this, the quadrotor MAV was controlled using the ground truth state estimates which were available as a part of the simulation. The true position and velocity of the quadrotor MAV for this simulation are presented in Fig. 4.3.

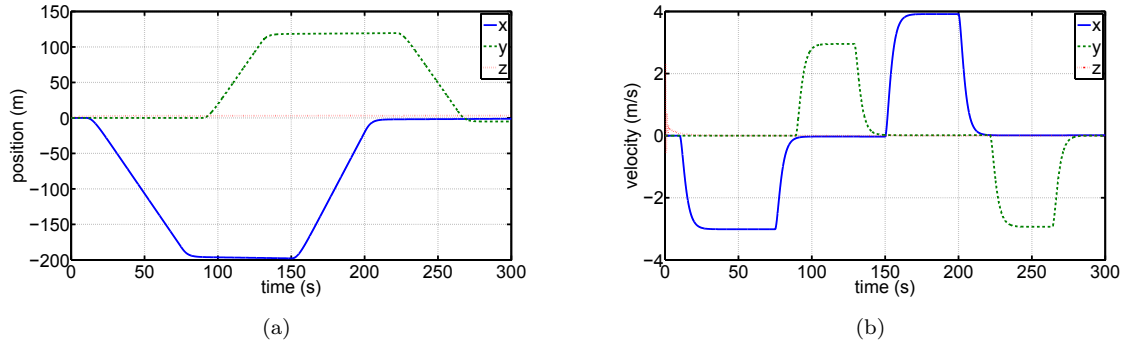


FIGURE 4.3: True states used in MA-VIF and C-VIF simulations: ((a)) position, ((b)) velocity.

4.5.1 Simulations with Consistent VSLAM Estimates

Initially, the virtual world through which the quadrotor MAV travels was populated with a point feature density that enables the VSLAM algorithm to extract and track at least 20 environmental features in each image. The objective here was to obtain accurate VSLAM estimates so that the performance of the two VIF algorithms can be analysed under ideal environmental conditions. A 2D projection of the VSLAM position estimates along with true position is presented in Fig. 4.4.

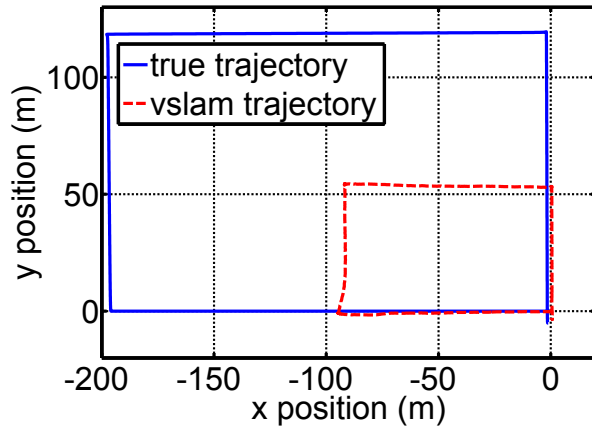


FIGURE 4.4: 2D projection of the VSLAM position estimates and ground truth for the first simulation. Note that the MAV heading was kept constant throughout the trajectory. Also note that the VSLAM position estimates are to an arbitrary scale. They have been adjusted for better comparison with ground truth by multiplying by a constant scale factor

Fig. 4.5 presents the velocity estimation error of the MA-VIF and the C-VIF for this simulation. Fig. 4.6 compares the scale estimation accuracy of the MA-VIF and the C-VIF. The true value of scale was obtained by calculating the ratio between the true and estimated distance from the origin of $\{E\}$ to the first environmental feature detected by the VSLAM algorithm.

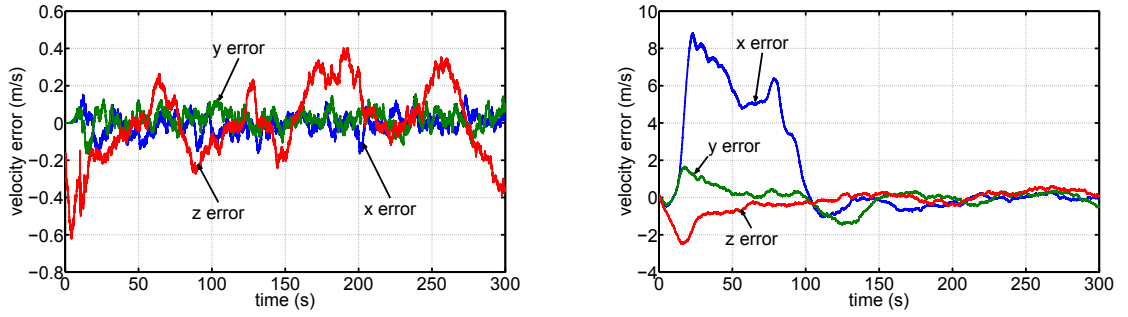


FIGURE 4.5: Velocity estimation error of ((a)) MA-VIF, ((b)) C-VIF for simulations with consistent VSLAM measurements. Note the difference in scale.

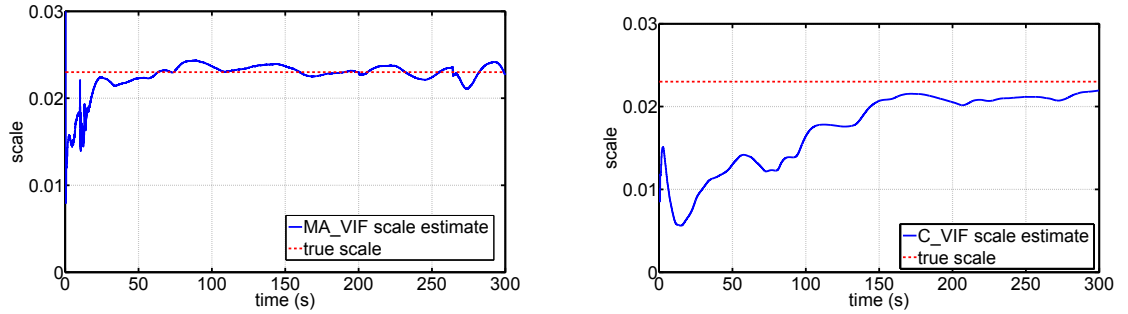


FIGURE 4.6: Scale estimates of MA-VIF ((a)), and C-VIF ((b)) for simulations with consistent VSLAM estimates.

As expected, both estimators are capable of producing metric scale velocity estimates. However, the accuracy of the MA-VIF is superior to the other, particularly during the 0 - 100s period. Analysing Fig. 4.6(b) and comparing it with the true velocity profile illustrated in Fig. 4.3(b), it can be seen that as predicted by the observability analysis, the corrections in C-VIF scale estimate only happens when the MAV is either accelerating or decelerating. The resulting scale estimation error causes the C-VIF to produce erroneous velocity estimates, as evident by Fig. 4.5(b). In contrast, the MA-VIF scale estimate is driven towards the true value as soon as the quadrotor starts moving and remains

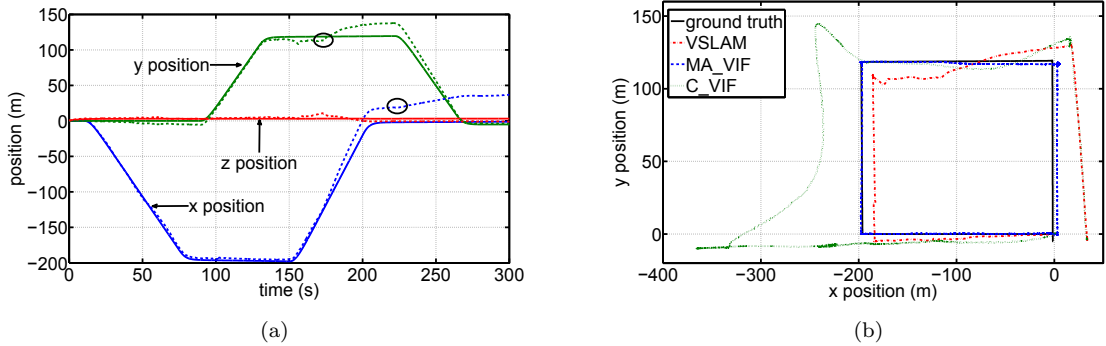


FIGURE 4.7: ((a)) - VSLAM position estimates (dotted lines) with ground truth (solid lines) position for the simulation with VSLAM errors. ((b)) - 2D projection of the position estimates (dotted lines) with ground truth (solid lines) for the second simulation. Note that the VSLAM position estimates are to arbitrary scale. They have been adjusted for better comparison with ground truth by multiplying by a constant scale factor.

sufficiently accurate to produce velocity estimates which, for the ${}^E\mathbf{x}$ and ${}^E\mathbf{y}$ axes, are an order of a magnitude more accurate than those of the C-VIF, throughout the flight. By comparing Fig. 4.6(a) with Fig. 4.3(b), it can be seen that the MA-VIF scale estimate begin to deviate from the true value when both Bv_x and Bv_y approach zero, as predicted by the observability analysis. However, it is difficult to observe the impact of this on the MA-VIF velocity estimation error plot of Fig. 4.5(a), as the MAV does not remain stationary for a considerably long period.

Both the MA-VIF and C-VIF produce similar velocity estimation errors for the ${}^E\mathbf{z}$ axis. This stems from the similarity in the process equations of the C-VIF and ${}^B\mathbf{z}$ axis of the MA-VIF. Neither of these is aided by a dynamic model with additional constraints, in contrast to the ${}^B\mathbf{x}$ and ${}^B\mathbf{y}$ axes of the MA-VIF.

4.5.2 Simulations with VSLAM Errors

Low feature density and incorrect matching due to illumination changes can introduce errors into the VSLAM pose estimates that are not modelled by Equation 4.1. Inherently, this will cause errors in the VIF estimates. To analyse the performance of the MA-VIF and the C-VIF under such conditions, the same simulation was performed again with the number of environmental features tracked by the VSLAM estimator in each image reduced to 5. Also during the experiments, two incorrect feature associations were artificially

introduced in the VSLAM estimator. Figure 4.7(a) presents the VSLAM position estimates so obtained, with the two incorrect feature matching events highlighted by small ellipses. As before, these estimates were then used as measurements in the MA-VIF and C-VIF algorithms.

A 2D projection of the position estimates from the VSLAM and the MA-VIF and C-VIF algorithms are presented in Fig. 4.7(b). Here again it can be seen that the MA-VIF outperforms the C-VIF in estimation accuracy. In addition, it is possible to see that the MA-VIF is capable of coping with the VSLAM errors more effectively than the C-VIF.

It is important to note that in the presence of these inconsistencies, Equation (4.1a) is no longer a valid description of the VSLAM estimates. In such a situation, the λ estimate of the VIF algorithms will no longer be a true description of scale. However, λ can be expected to change in a manner that would produce correct position and velocity estimates, at least in the short term. The scale estimates of the two VIF algorithms are presented in Fig. 4.8. It can be seen that the MA-VIF scale estimate deviates from the true value of scale when incorrect data associations take place near 175s and 210s to ensure the accuracy of the position and velocity estimates as illustrated by Fig. 4.7(b). The C-VIF on the other hand fails to make sufficient corrections in the scale estimate despite converging to the true scale near 175s.

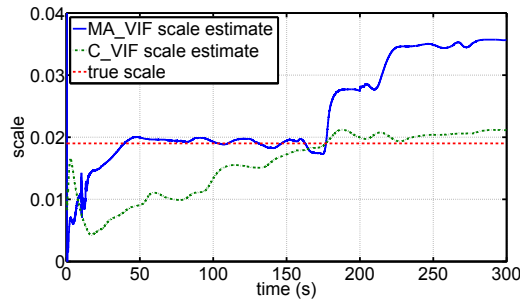


FIGURE 4.8: Scale estimates of the MA-VIF and C-VIF along with true scale. The C-VIF estimate converge to the true scale but fails to make corrections to account for the errors in VSLAM estimates.

4.6 Experimental Evaluation of C-VIF and MA-VIF

Several flights of the ARDrone were performed within the Vicon environment with the intention of experimentally evaluating the proposed model-aided VIF design and to identify the improvements due to model-aiding. Estimation results from one of the flights is provided in this section.

An open source implementation [75] of the inverse-depth monocular SLAM algorithm was used to process the time stamp images captured at approximately 10Hz from the front camera of the ARDrone and to produce orientation, scaled position estimates and their covariances. This VSLAM implementation makes use of constant angular and linear velocity models for tracking features between images. Fast camera motion caused by the flight pattern of the ARDrone and the close proximity of features of the indoor environments resulted in considerable apparent motion between the consecutive images of this data set. This made it extremely difficult for constant velocity based models to track environmental features between consecutive images. Therefore, attempts to process the images using the default implementation of EKF based ID monocular SLAM algorithm [75] failed repeatedly despite meticulous tuning of the filter noise parameters.

It is possible to forego the feature tracking step altogether by employing a high quality feature descriptor. In such an implementation, salient features and their descriptors are extracted throughout each new image and matched with the descriptors of the features currently in the map to establish initial correspondences. To achieve this, the ID monocular SLAM implementation [75] was modified to extract at least 50 SIFT [76] features in each image, descriptors of which were then used for data association process of the VSLAM estimator. A 2D projection of part of the VSLAM position estimate (220s - 230s) along with the ground truth is presented in Fig. 4.9 to highlight the quality and the arbitrary scale of the VSLAM estimates.

The orientation and scaled position estimates and their covariances obtained from the VSLAM implementation were then combined with the IMU measurements using a Matlab implementation of C-VIF and MA-VIF algorithms. All processing was done off-line and

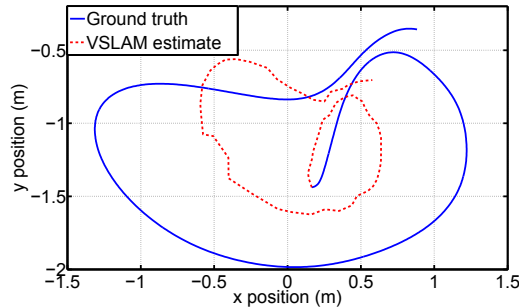


FIGURE 4.9: 2D projection of part of the VSLAM position estimates and ground truth used in loosely-coupled state estimation for the ARDrone experiments. Note that the starting point of the VSLAM estimate was translated to the ground truth position to enable better comparison with ground truth.

off-board on a desktop computer. Two separate estimation tasks were performed, one with all VSLAM estimates and the other with VSLAM estimates sub-sampled at about 1Hz.

4.6.1 VIF with Frequent VSLAM Estimates

First, the visual-inertial fusion was performed with 10Hz VSLAM pose estimates. The position and velocity estimates of the proposed MA-VIF estimator along with the ground truth of this experiment are presented in Fig. 4.10. This figure demonstrates that the MA-VIF is capable of producing metric scale translation estimates, even with less than perfect VSLAM estimates.

Fig. 4.11 compares the position estimation errors from both VIF estimators. Though MA-VIF estimates are more accurate, the improvement over C-VIF in this case is marginal. This is due to the fact that the flight pattern consisted of sufficiently exciting motion² - non-zero acceleration - ensuring that the C-VIF remains observable throughout the flight.

4.6.2 VIF with Sparse VSLAM Updates

To examine the impact of sparse VSLAM updates on the VIF algorithms, another experiment was performed with the frequency of VSLAM measurements reduced to about 1Hz.

²The small size of the capture volume in the Vicon motion capture studio made it difficult to operate the quadrotor MAV in a manner that maintained a constant velocity for a satisfactory time period.

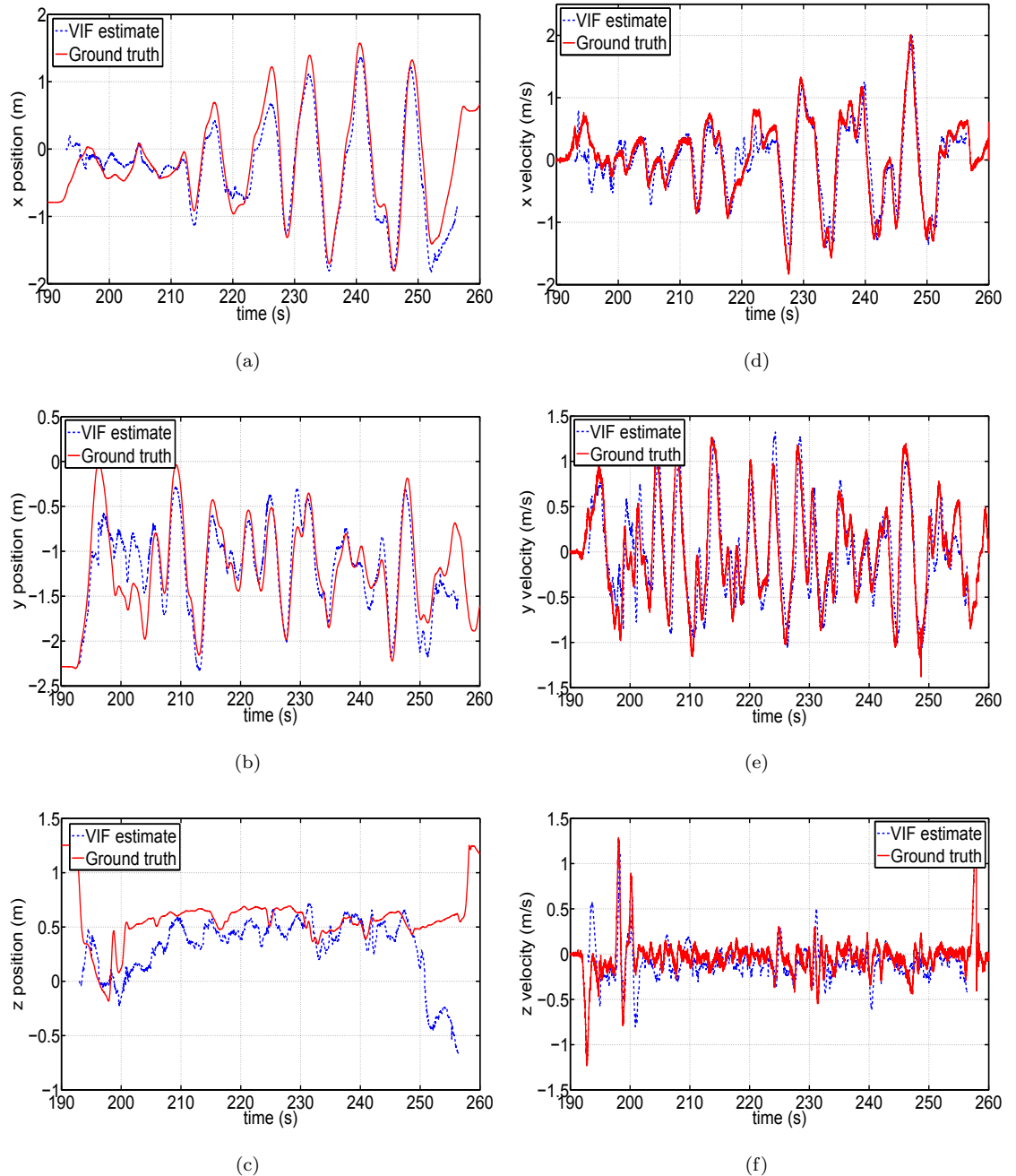


FIGURE 4.10: Position ((a)) - ((c)) and velocity ((d)) - ((f)) estimates of the loosely-coupled MA-VIF along with ground truth for ARDrone experiments using frequent VS-LAM measurements. The ground truth 2D plot for these estimates were illustrated in Fig. 4.9.

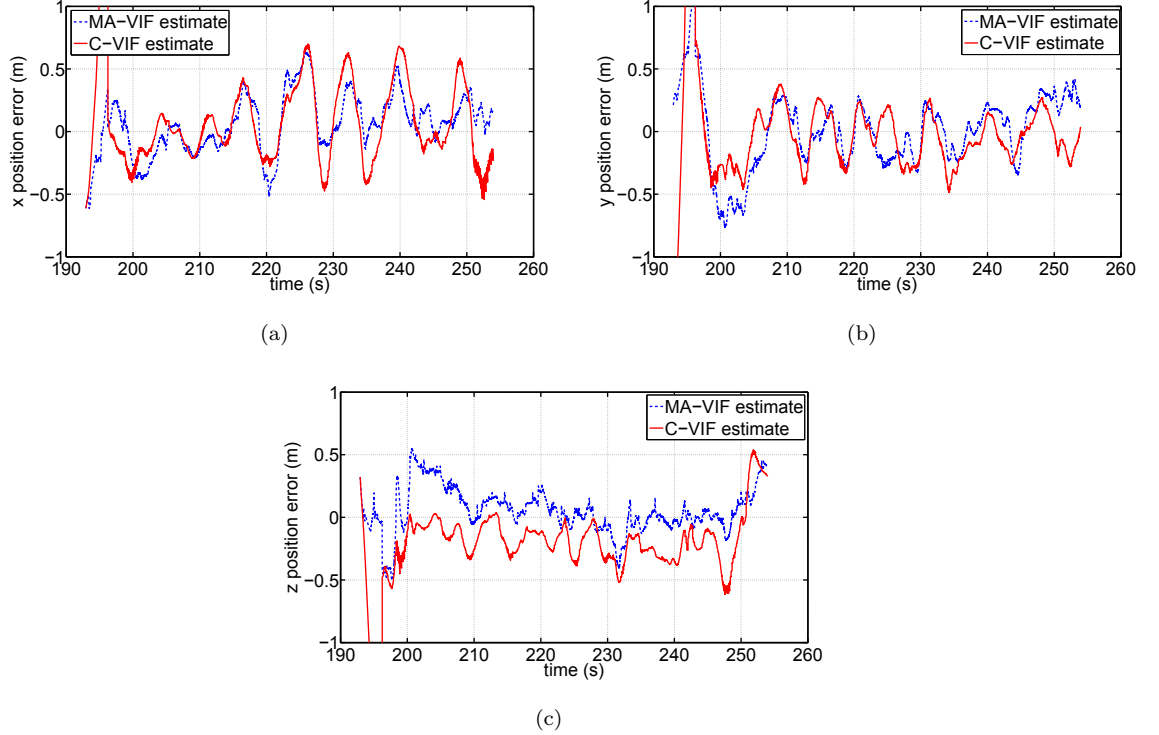


FIGURE 4.11: Position estimation errors of the loosely-coupled MA-VIF and C-VIF for ARDrone experiments using frequent VSLAM measurements.

The VSLAM estimates for this experiment were obtained by taking every tenth sample of the original VSLAM estimates. The results, presented in Fig. 4.12, demonstrate the improvements brought about by the MA-VIF estimator. The C-VIF estimator relies solely on acceleration measurements between VSLAM measurements, and thus even a small error in accelerometer bias estimate can cause significant position drift. In contrast, the MA-VIF estimator is aided by the dynamic model of the quadrotor MAV and as a result the evolution of position and velocity states is not directly driven by the accelerometer measurements. This restricts the position and velocity drift during prolonged inertial only update sequences.

Table 4.4 lists the RMS position estimation errors of each of the C-VIF and MA-VIF algorithm implementations. The improvement in estimation accuracy due to the incorporation of the MAV dynamic model can be clearly seen by analysing Table 4.4, especially for the case when the vision update rate was reduced to 1Hz.

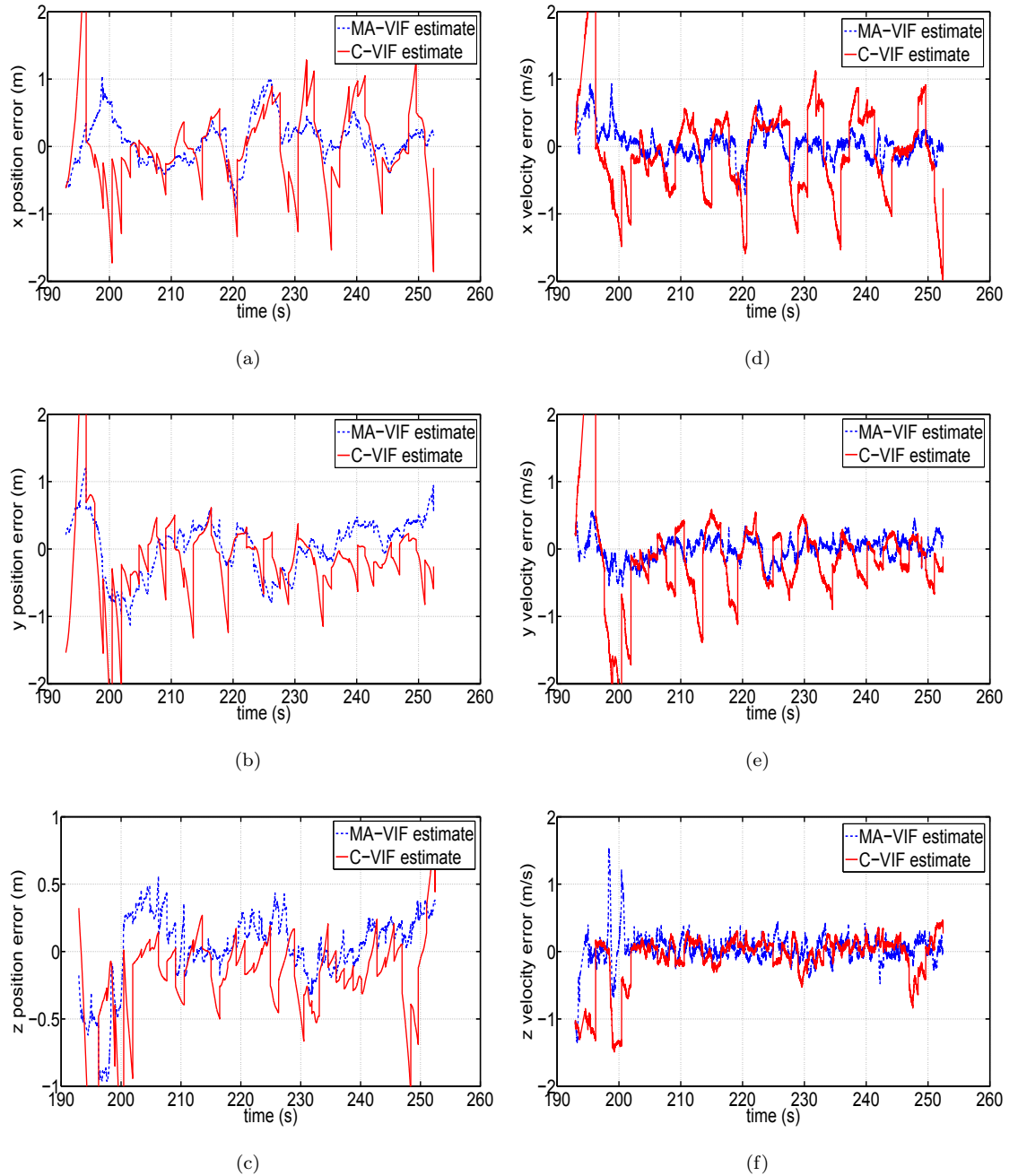


FIGURE 4.12: Position ((a)) - ((c)) and velocity ((d)) - ((f)) estimation errors of the loosely-coupled MA-VIF and C-VIF algorithms for ARDrone experiments with 1Hz VS-LAM measurements. The ground truth 2D plot for these estimates were illustrated in Fig. 4.9.

TABLE 4.4: Performance of different estimators. LC stands for loosely-coupled. The rate within brackets is the rate at which image information is used by the filter

Structure	RMS position error(m/s)		
	x	y	z
LC-C-VIF (10Hz)	0.27	0.25	0.35
LC-MA-VIF (10Hz)	0.24	0.24	0.30
LC-C-VIF (1Hz)	0.6	0.56	0.7
LC-MA-VIF (1Hz)	0.4	0.37	0.39

4.7 Tightly-Coupled MA-VIF

The previous section illustrated how incorporating the quadrotor MAV dynamics in the design can improve the performance of VIF estimators for quadrotor MAVs. Although the loosely-coupled version of the MA-VIF demonstrated a marked improvement compared to the C-VIF benchmark, its absolute estimation accuracy is still dominated by the accuracy of the VSLAM estimates due to the loosely-coupled design. It is possible to further improve this accuracy by redesigning the MA-VIF in a tightly-coupled manner.

Furthermore, tightly-coupling the inertial measurements and the quadrotor dynamic model into the VSLAM estimator has the potential to reduce the computational time required by the VSLAM module to track features from one image to another. A filter based VSLAM implementation makes use of the state prediction equations to limit the region that has to be searched in each image to identify each of the currently tracked features. The MA-VIF employs a process model with improved accuracy due to the incorporation of the quadrotor dynamics. This improved accuracy can further limit the image regions that have to be searched to identify the environmental features.

In a tightly-coupled formulation, the direct visual measurements - pixel positions of tracked features - are combined with inertial measurements and the quadrotor MAV dynamics within a single estimator, typically an EKF. A simplified block diagram of a tightly-coupled VIF is presented in Fig. 4.13. The feature management module is responsible for identifying and tracking salient environmental features through consecutive images. Each feature is identified uniquely by a descriptor that is extracted from the neighbourhood of its image location. Best estimate of the camera pose when the image was captured

and the current best estimate of the location of tracked features are provided to the feature management module so that the most likely region in the current image that the feature should appear can be predicted. A search within this region using the feature descriptor provides the measured pixel location of the feature in the current image. These measurements for each feature are then forwarded to the VIF module.

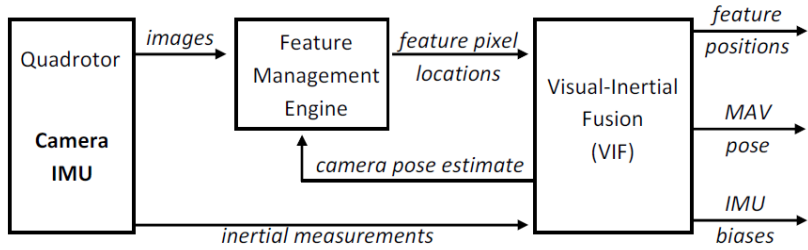


FIGURE 4.13: Structure of a tightly-coupled Visual-inertial fusion set-up.

A tightly-coupled MA-VIF implementation can be achieved by starting with a filter based VSLAM implementation and then augmenting it with the process and measurement equations detailed in Table 4.3. For the purpose of this thesis, the inverse-depth monocular SLAM implementation by Civera et al. [45] was chosen as the base VSLAM implementation as it performs accurate undelayed initialization of environmental features. Undelayed feature initialization is essential to an effective VSLAM algorithm with small number of features and fast camera motion. Details of this implementation and how it was modified can be found in Appendix B.

4.7.1 Estimation Results

The tightly-coupled MA-VIF was evaluated using the same IMU and image data used for evaluating the loosely-coupled implementations. A Matlab implementation of the tightly-coupled MA-VIF algorithm was developed and it was tuned so that it tracked about 10 environmental features in each image on average. The maximum number of environmental features in the state vector was limited to 30 to limit the computational time. All data processing was performed off-board and off-line. Position, velocity and orientation estimates for this experiment along with ground truth are presented respectively in Fig. 4.14, Fig. 4.15 and Fig. 4.16.

TABLE 4.5: Performance comparison of LC and TC MA-VIF implementations LC stands for loosely-coupled and TC stands for tightly-coupled. The rate within brackets is the rate at which image information is used by the filter. The experiments were conducted within the Matlab computing environment in an Intel Core2 Duo CPU operating at 3GHz with 4GB of main memory

Structure	RMS position error(m/s)			Execution time (s) per image
	x	y	z	
LC-MA-VIF (10Hz)	0.24	0.24	0.30	2
LC-MA-VIF (1Hz)	0.4	0.37	0.39	2
TC-MA-VIF (10Hz)	0.06	0.13	0.19	0.3

These figures clearly illustrates that the filter is producing consistent, metric scale estimates. The errors in ${}^e p_z$ axis for position and ${}^b v_z$ axis for velocity are considerably higher than the other axes. This increased error stems from the lack of a dynamic relationship in the filter constraining the quadrotor motion in ${}^b v_z$ axis, as is the case for ${}^b v_x$ and ${}^b v_y$ axes. A similar trend can be seen in yaw angle estimate when compared to the roll and pitch estimates.

Table 4.5 compares the performance of the loosely-coupled and tightly-coupled variations of the MA-VIF. It can be seen that the tightly-coupled formulation considerably improves both the accuracy and speed of execution of the model-aided visual-inertial fusion framework. Note that the execution times presented are for a Matlab implementation which was not optimized for speed of execution. It is expected that the execution times can be reduced when porting the Matlab implementations to a programming language optimized for real-time operation such as C.

4.8 Discussion and Limitations

The main contribution of the chapter was to show how the dynamic characteristics of the quadrotor MAV can be employed to improve the performance of a quadrotor MAV state estimator based on visual-inertial fusion. The observability analysis showed that the proposed model-aided VIF (MA-VIF) formulation improves the observability of the conventional visual-inertial fusion (C-VIF) algorithms. Unlike the C-VIF, the MA-VIF

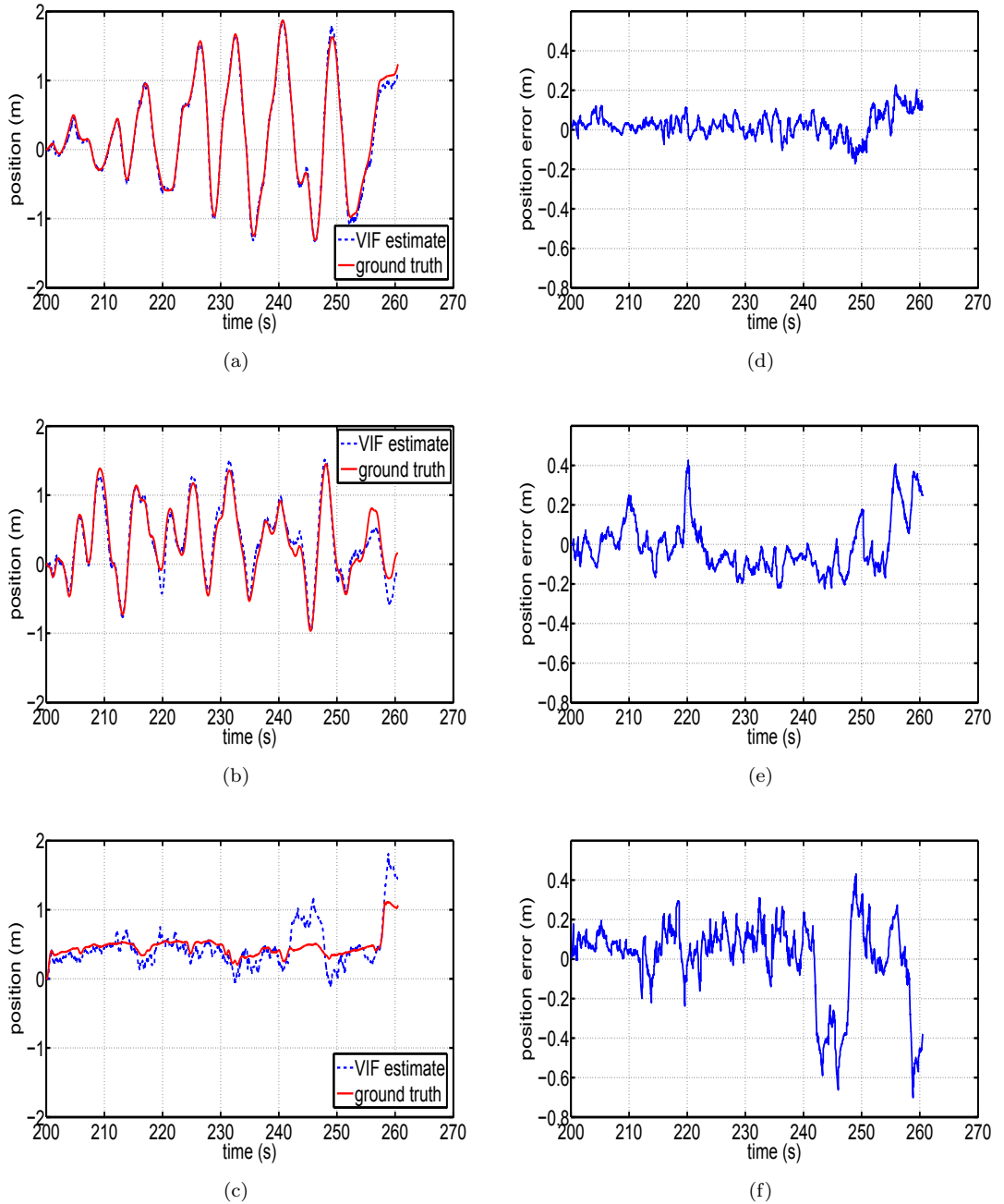


FIGURE 4.14: Tightly-coupled MA-VIF position estimates: x - ((a)), y - ((b)), z - ((c)) and respective position estimation errors ((d)) - ((f)) for ARDrone experiments

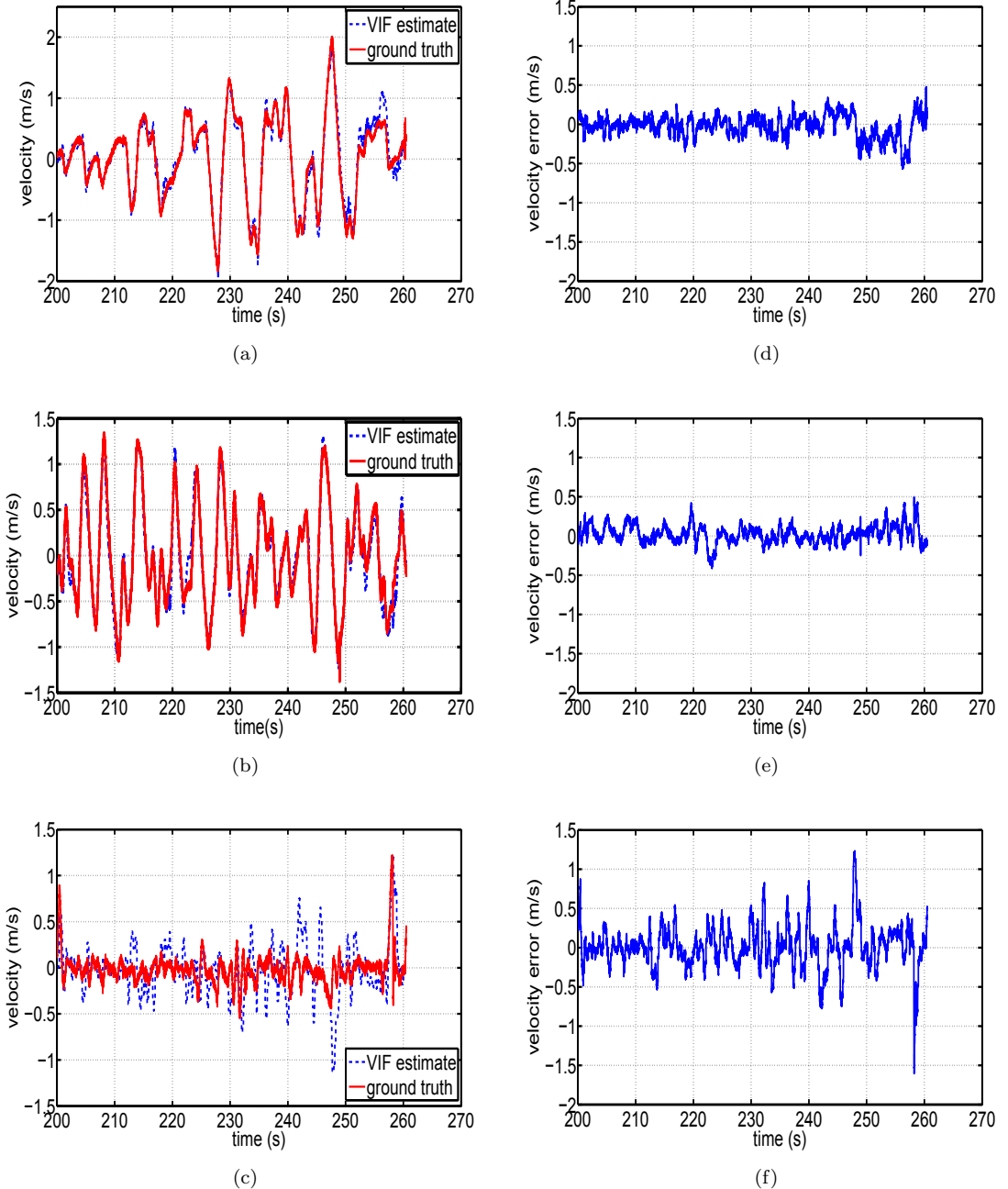


FIGURE 4.15: Tightly-coupled MA-VIF velocity estimates: x - ((a)), y - ((b)), z - ((c)) and respective velocity estimation errors ((d)) - ((f)) for ARDrone experiments

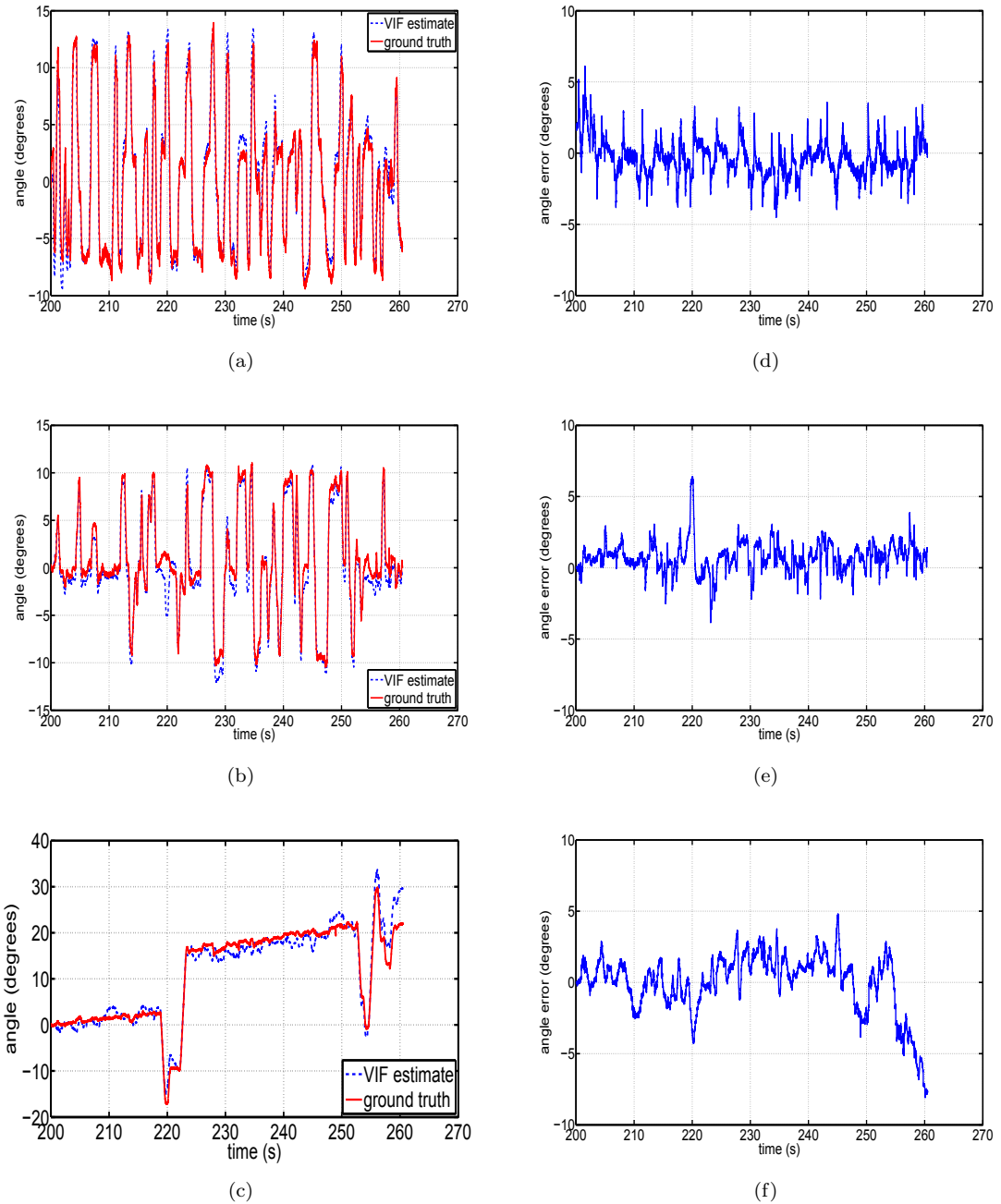


FIGURE 4.16: Tightly-coupled MA-VIF attitude estimates: roll - ((b)), pitch - ((a)), yaw - ((c)) and respective attitude estimation errors ((e)) - ((f)) for ARDrone experiments

formulation is observable whenever the quadrotor MAV is in motion, leading to an estimator design that is well conditioned for almost all flight envelopes. The MA-VIF loses scale observability when the quadrotor MAV is hovering. However, it should also be noted that the scale drift of a VSLAM algorithm is negligible when the camera is stationary and observing the same set of features. Therefore, the unobservability of scale during hover is unlikely to cause significant estimation errors if a sufficiently accurate estimate of scale is already available.

Simulations presented in Section 4.4 illustrated that the improved observability of the MA-VIF translates to increased estimation accuracy compared to the C-VIF. The accuracy improvement was most prominent when the quadrotor MAV undergoes flight sequences with small inertial accelerations. Experimental results also demonstrated that model-aiding resulted in improved performance in situations where the VSLAM updates become infrequent. This points to the possibility of reducing the computational complexity of VIF algorithms without compromising the estimation accuracy.

In a loosely-coupled VIF implementation, the VSLAM module functions independently of the quadrotor MAV dynamics and therefore is not aided by its dynamic characteristics. This design can be further improved by the tight-coupling of the three available information sources - IMU measurements, camera images and quadrotor MAV dynamic model in a single coherent estimator. The tightly-coupled MA-VIF implementation presented in Section 4.7 showed that such a design is capable of limiting the position estimation errors to a few tens of centimetres, while only tracking a handful of environmental features between images.

There is however, one aspect of the model-aided state estimation framework that has not been addressed in the exposition of both this chapter and Chapter 3. The quadrotor MAV dynamic model employed in the design of model-aided state estimators is only accurate in zero wind conditions. While such conditions can be expected when operating in spacious indoor environments, most other environments where GPS-denied operation is required are affected by ambient wind streams or wind disturbances. How the MA-VIF would react to such wind disturbances needs to be analysed and the possibility of extending the

MA-VIF to cope with wind disturbances needs to be explored. This is the focus of the next chapter.

Chapter 5

Effects of and Estimating Wind

5.1 Introduction

The model-aided state estimators designed in Chapters 3 and 4 made use of the assumption that the quadrotor MAV is operating in an environment with zero wind disturbances. While this assumption is valid for spacious indoor environments, the quadrotor MAV could be subjected to large wind disturbances when it is operating in outdoor environments such as urban areas or when operating close to large structures such as buildings, dams or bridges. As a result, its behaviour could deviate substantially from that predicted by a dynamic model which assumes that the wind velocity is zero. If such a dynamic model is used to aid a state estimator, then it will cause an increase in the estimation errors when the quadrotor MAV is undergoing non-zero wind disturbances.

The aim of this chapter is twofold. First, it analyses the impact of non-zero wind on the estimation accuracy of model-aided state estimators that rely on the zero wind assumption. For this the simulations of the Model-aided Attitude and Velocity Estimator (MAVE) of Chapter 3 and the Model-Aided Visual-Inertial Fusion (MA-VIF) implementations of Chapter 4 are employed. As the effects of wind was not modelled in the basic quadrotor MAV simulation detailed in Chapter 2, a more realistic high-fidelity quadrotor MAV simulation including an environmental wind model developed by Waslander and Wang [44] is employed in this chapter to generate the simulation data required to analyse the

performance of these two filters. With this analysis, it will be shown that both algorithms are capable of coping with slowly varying wind disturbances but produce increased errors when the wind disturbances are strong and rapidly varying.

The second aim of this chapter is to explore the possibility of extending the MA-VIF design to incorporate the effects of wind into the design of the state estimator. It demonstrates through an observability analysis, simulations and experiments that it is indeed possible to produce accurate pose estimates amidst strong wind disturbances by properly extending the model-aided VIF framework to account for the effects of wind. It also demonstrates that, as a by product of this extension, an estimate of two components of the wind velocity can be obtained. As demonstrated by Waslander and Wang [44], such an estimate can then be employed to improve the positioning accuracy of a quadrotor MAV following a given trajectory.

5.2 Background and Related Work

Estimating the direction and speed of wind can be of critical importance to a MAV operating in out-door environments. If an estimate of the platforms inertial velocity and its velocity with respect to the air stream is available, then the wind velocity can be calculated instantaneously by subtracting the two velocities. Langelaan et al. [77] made use of air speed measurements from a pitot tube and GPS based ground velocity to directly calculate the wind velocity for a fixed wing aircraft. Using simulations, they showed that main source of error in estimating wind velocity is the airspeed sensor. Kim and Sukkarieh [78] demonstrated through simulations of a fixed wing MAV that wind velocity can be estimated using an air-data system and a vision sensor which provides range, bearing and elevation to environmental features on the ground. An aid-data system provides angle of attack (pitch angle relative to the wind) and side-slip angle (yaw angle relative to the wind) of the aircraft in addition to airspeed and these measurements contain the information required to estimate the velocity of the MAV with respect to the air. Kim and Sukkarieh [78] combined those measurements with the vision measurements in a Kalman filter to simultaneously estimate the vehicle pose and the wind velocity.

A single pitot tube can only be employed to obtain an airspeed measurement when the motion is mostly uni-directional, such as that of a fixed wing aircraft. However, for holonomic mobile robots such as quadrotor MAVs, a single airspeed sensor is not sufficient. Zachariah et al. [79] presented a wind speed estimator suitable for a generic MAV by making use of measurements from three orthogonal anemometers and a monocular camera. There again, only simulation results were used for validation. This method however, is not suitable for quadrotors as an arrangement of multiple anemometers adds significant additional complexity and weight to the design. Also airspeed sensors such as pitot tubes are only accurate in high flight speeds, so while they may be suitable for fixed wing MAVs, they are not ideal for quadrotor MAVs.

Instead of airspeed sensors, Waslander and Wang [44] employed the quadrotor dynamic model along with IMU measurements to predict the MAV velocity with respect to air. Using simulations they showed that it is possible to estimate wind velocity by combining the MAV velocity estimate with GPS measurements. Neumann et al. [80] followed a similar approach but made use of an experimentally derived relationship between the quadrotor inclination angle and the air speed instead of a dynamic model. Through experiments performed in a wind tunnel, they showed that this method can produce reasonably accurate wind speed and direction estimates. Similar to these approaches, this chapter also employs the quadrotor MAV dynamic model to estimate its velocity with respect to air. However, here the pose estimates from a monocular VSLAM algorithm are used instead of GPS measurements. This change introduces an additional challenge as the position estimates of the VSLAM algorithm are of arbitrary scale. To the best of author's knowledge, this is the first time the observability of such an approach has been analysed and the conditions for observability identified.

5.3 Wind Model for Simulations

It is convenient to have a simulation model for wind velocity in a typical urban environment to aid the design and evaluation of state estimators for windy environments. Milbank et al. [81] employed empirical data to identify typical characteristics of wind patterns that would affect a MAV operating in urban environments, close to ground and at velocities less than

$10m/s$. Waslander and Wang [44] developed a mathematical model that adheres to those characteristics to simulate such wind conditions. The input to the model is the above ground altitude of the MAV and the output is the wind velocity currently affecting the MAV. It consists of two main components: a static dominant wind model and a wind gust model dependent on a standard power spectral density (PSD). The static component characterizes the underlying dominant wind characteristics and was presumed to vary on a time scale somewhat larger than the scale of vehicle flight time. The wind gust model with accompanying PSD was derived from the Dryden model [82] relying on the static wind model to generate necessary parameters for the PSD. The resulting wind gust velocities contain components with several different frequencies to simulate realistic wind gust patterns.

This wind model was used in the high-fidelity quadrotor MAV simulator described in Chapter 2 to obtain the earth frame wind velocity $E\mathbf{v}_w$. To ease the analysis of the estimator performance in windy conditions, only either the static component or the wind gust component was turned on in any given simulation. An example output of the two components is shown in Fig. 5.1.

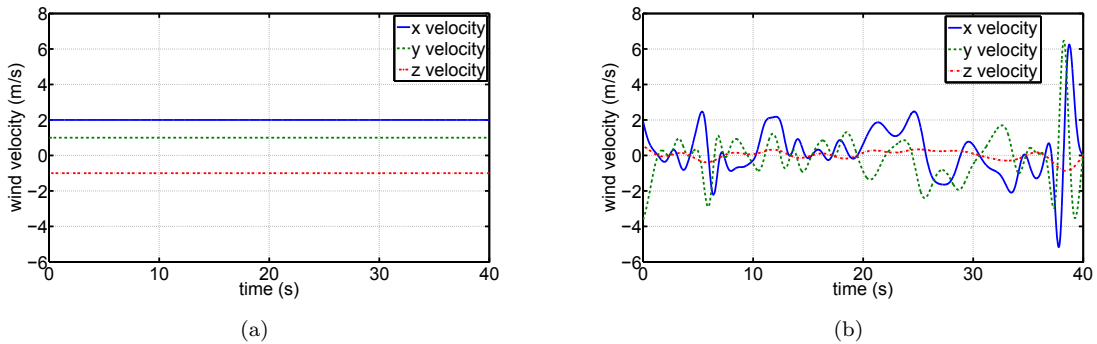


FIGURE 5.1: True inertial frame wind velocities used for simulations (a) - constant wind
(b) - wind gusts.

5.4 Effects of Wind on State Estimation

The MAVE of Chapter 3 and MA-VIF of Chapter 4 were designed to operate in environments with no external wind disturbances. To understand how these estimators would

perform when subjected to wind disturbances, several simulations were performed with the wind patterns shown in Fig. 5.1.

5.4.1 Inertial Estimators

Velocity and attitude estimation errors of the MAVE when the wind velocity is constant are shown in Fig. 5.2. It can be seen that the MAVE can produce accurate attitude estimates even amidst wind disturbances. However, the MAVE velocity estimates exhibits a significant error, the magnitude of which is equal to the wind velocities in ${}^B\mathbf{x}$, ${}^B\mathbf{y}$ axes. This can be explained by revisiting the quadrotor MAV dynamic model upon which the

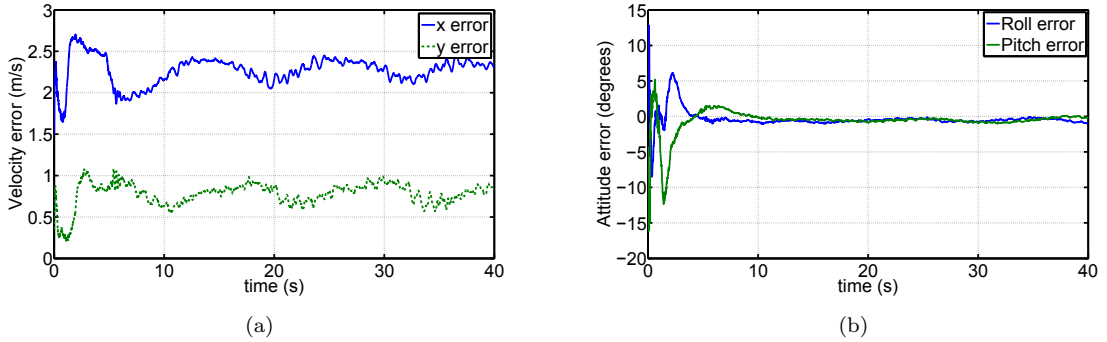


FIGURE 5.2: Estimation errors of the MAVE from constant wind simulations (a) - Velocity
(b) - Attitude.

MAVE is based on. Rewriting Equation 3.12 for non-zero wind case and noting that ${}^B\mathbf{v}_\infty = {}^B\mathbf{v} - {}^B\mathbf{v}_w$ and also noting that if the wind velocity is constant in $\{B\}$ then ${}^B\dot{\mathbf{v}}_\infty = {}^B\dot{\mathbf{v}}$, the following can be obtained:

$${}^B\dot{\mathbf{v}}_\infty = {}_E^BR\mathbf{g} + \frac{f_T}{m}\mathbf{e}_3 - \bar{D}_L {}^B\mathbf{v}_\infty + \boldsymbol{\eta}_v. \quad (5.1)$$

Therefore, it can be seen that when wind velocity is constant in $\{B\}$, the MAVE operates as a filter that estimates the attitude and free stream velocity of the quadrotor MAV. The difference between this estimate and the MAV true inertial velocity in $\{B\}$ is exactly given by the velocity of wind in $\{B\}$. Though the wind velocity for this experiment generated to be constant in $\{E\}$, as the MAV only underwent small roll and pitch angles, it is

reasonable to assume that wind velocity in $\{B\}$ is also smoothly varying, thus making the same reasoning valid for this simulation.

With the above analysis and the results in Fig. 5.2, it can be concluded that the MAVE can produce accurate estimates of the MAV attitude when it is operating in near hover conditions amidst constant wind disturbances. However, when these conditions are violated, the MAVE estimates of both the velocity and attitude of the quadrotor MAV will become erroneous. This can be seen in Fig. 5.3, which presents the velocity and attitude estimation errors of the MAVE for the wind gusts shown in Fig. 5.1(b).

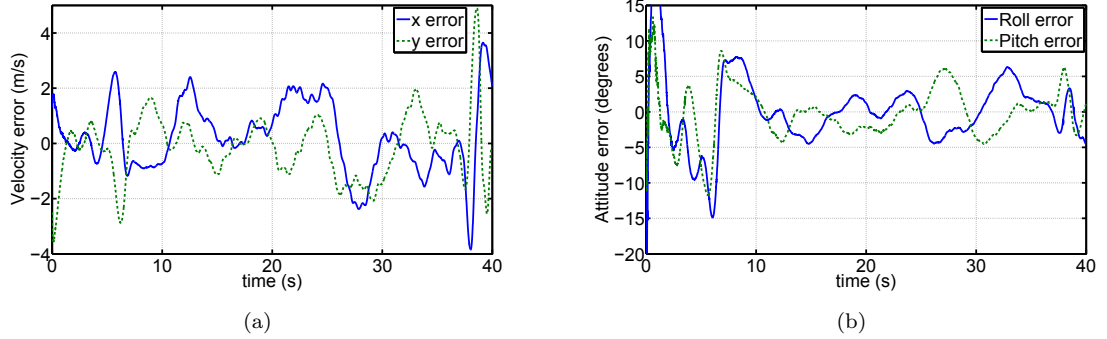


FIGURE 5.3: Estimation errors of the MAVE from wind gust simulations (a) - Velocity
(b) - Attitude.

5.4.2 Visual Inertial Estimators

Position and velocity estimation errors of the MA-VIF for both constant wind velocity and wind gusts are presented in Fig. 5.4. Similar to the MAVE, the MA-VIF is demonstrably capable of coping with constant (slowly varying) wind patterns. But it produces significant errors when the wind disturbances are of higher amplitude and rapidly varying. This result is as expected because the MA-VIF is based on a dynamic model that becomes inaccurate when external wind disturbances are present. Small wind disturbances may be tolerated by way of increasing the process noise terms that account for the dynamic model imperfections. More details on this can be found in Section 5.5.5. However, when wind disturbances are large and rapidly varying, the process model becomes substantially inaccurate. This indicates that the MA-VIF needs to be redesigned taking the effects of

wind into account if the quadrotor MAV dynamics are to be exploited to aid the state estimation process.

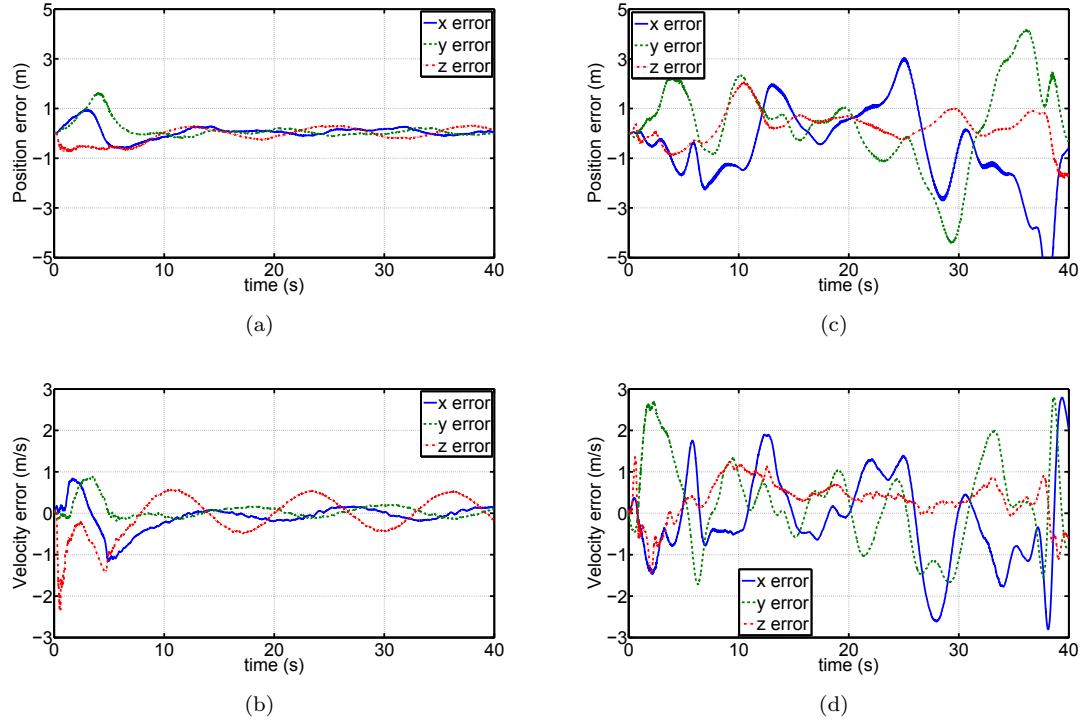


FIGURE 5.4: Estimation errors of the MA-VIF from constant wind simulations (a) - position (b) - velocity, and from wind gust simulations (c) - position (d) - velocity

5.5 Incorporating the Wind Effects in the Estimator

The MA-VIF can be redesigned to overcome its limitations in the presence of wind by extending the quadrotor MAV dynamics to explicitly model the effects of wind. Such a design has the additional advantage of being able to estimate the velocity of wind affecting the MAV. This section presents the process and measurement equations required for such a filter including the observability analysis. For ease of reference, this filter design is termed wMA-VIF.

5.5.1 States, Process Model and Measurements

The translational dynamics of the quadrotor MAV when the wind is presented is given by:

$${}^B\dot{\mathbf{v}} = {}^B_E R \mathbf{g} + ({}^B a_z - \beta_{az}) \mathbf{e}_3 - \bar{D}_L {}^B \mathbf{v}_\infty + \boldsymbol{\eta}_v. \quad (5.2)$$

where ${}^B \mathbf{v}_\infty = {}^B \mathbf{v} - {}^B \mathbf{v}_w$. This equation is the same as that used in the process dynamics of MA-VIF, except that the induced drag term is now a function of ${}^B \mathbf{v}_\infty$ instead of ${}^B \mathbf{v}$, due to the non-zero wind velocity.

As the quadrotor MAV dynamics in Equation 5.2 depend on the velocity of the wind, ${}^B \mathbf{v}_w$ needs to be included in the state vector and for that an expression describing the time evolution of wind velocity need to be derived. Given the complexities associated with deriving a precise dynamic model that describes the dynamics of wind, here it is assumed that the wind velocity is smoothly varying in $\{E\}$, thus resulting in ${}^E \dot{\mathbf{v}}_w = \boldsymbol{\eta}_w$ where $\boldsymbol{\eta}_w$ is a 3×1 vector of zero mean WGN variables which are uncorrelated with each other. The same assumption has been used previously by Waslander and Wang [44].

Similar to the MA-VIF, the wMA-VIF makes use of the ${}^B \mathbf{x}, {}^B \mathbf{y}$ accelerometers and the VSLAM algorithm as sensors providing measurements according to Equations 2.16 and 4.1, respectively. The process and measurement equations for this initial design of the wMA-VIF are summarised in Table 5.1. The complete state vector for the wMA-VIF has 19 states and the observability of it is analysed in the next section prior to proceeding with an EKF based state estimator design.

TABLE 5.1: Model-Aided Visual-Inertial Fusion Estimator with Wind States

Process Equations	
$\begin{bmatrix} {}^E\dot{\mathbf{p}} \\ {}^B\dot{\mathbf{v}} \\ \dot{\lambda} \\ \dot{\Theta} \\ \dot{\beta}_a \\ \dot{\beta}_g \\ {}^E\dot{\mathbf{v}}_w \end{bmatrix}$	$\begin{bmatrix} {}^E R {}^B \mathbf{v} \\ {}^B R \mathbf{g} + ({}^B a_z - \beta_{az}) \mathbf{e}_3 - \bar{D}_L ({}^B \mathbf{v} - {}^B R^T {}^E \mathbf{v}_w) + \boldsymbol{\eta}_v \\ \eta_\lambda \\ \Xi ({}^B \boldsymbol{\omega}_g - \beta_g + \boldsymbol{\eta}_g) \\ \boldsymbol{\eta}_{\beta a} \\ \boldsymbol{\eta}_{\beta g} \\ \boldsymbol{\eta}_w \end{bmatrix}$
Measurement Equations	
$\mathbf{h}_i = \begin{bmatrix} {}^B a_x \\ {}^B a_y \end{bmatrix} = -k_1 \Upsilon ({}^B \mathbf{v} - {}^B R^T {}^E \mathbf{v}_w) + \Upsilon \beta_a + \Upsilon \boldsymbol{\eta}_a$	
$\mathbf{h}_{vp} = \lambda {}^e \mathbf{p} + \boldsymbol{\eta}_p$	
$\mathbf{h}_{vo} = \Theta + \boldsymbol{\eta}_o$	

5.5.2 Observability Analysis of Wind Affected System

For the locally-weak observability analysis, the process equation of the wMA-VIF in Table 5.1 needs to be expressed in the input linear form. This results in:

$$\begin{aligned}
 \mathbf{X} = & \underbrace{\begin{bmatrix} {}^E\dot{\mathbf{p}} \\ {}^B\dot{\mathbf{v}} \\ \dot{\lambda} \\ \dot{\Theta} \\ \dot{\beta}_a \\ \dot{\beta}_g \\ {}^E\dot{\mathbf{v}}_w \end{bmatrix}}_{f_0} = \begin{bmatrix} {}^E R {}^B \mathbf{v} \\ {}^B R^T \mathbf{g} - \bar{D}_L({}^B \mathbf{v} - {}^B R^T {}^E \mathbf{v}_w) - \Gamma \boldsymbol{\beta}_a + \boldsymbol{\eta}_v \\ \eta_\lambda \\ -\Xi \boldsymbol{\beta}_g - \boldsymbol{\eta}_\Theta \\ \boldsymbol{\eta}_{\beta a} \\ \boldsymbol{\eta}_{\beta g} \\ \boldsymbol{\eta}_w \end{bmatrix} \\
 & + \underbrace{\begin{bmatrix} \mathbf{0}_{3 \times 1} \\ [0 \ 0 \ 1]^T \\ 0 \\ \mathbf{0}_{3 \times 1} \\ \mathbf{0}_{3 \times 1} \\ \mathbf{0}_{3 \times 1} \\ \mathbf{0}_{3 \times 1} \end{bmatrix}}_{f_1} {}^B a_z + \underbrace{\begin{bmatrix} \mathbf{0}_{3 \times 1} \\ \mathbf{0}_{3 \times 1} \\ 0 \\ \Xi \\ \mathbf{0}_{3 \times 1} \\ \mathbf{0}_{3 \times 1} \\ \mathbf{0}_{3 \times 1} \end{bmatrix}}_{f_2} {}^B \boldsymbol{\omega}_g. \tag{5.3}
 \end{aligned}$$

By considering the non-trivial Lie derivatives of the system up to second order, the following observability matrix can be constructed for the wMA-VIF:

$$\begin{aligned}
\mathcal{O}_5 &= [\nabla L^0 h_{vp}(x) \ \nabla L^0 h_{vo}(x) \ \nabla L^0 h_i(x) \ \nabla L_{f_0}^1 h_{vp}(x) \dots \\
&\quad \nabla L_{f_0}^1 h_{vo}(x) \ \nabla L_{f_0}^1 h_i(x) \ \nabla L_{f_0}^2 h_{vp}(x)]^T \tag{5.4} \\
&= \begin{bmatrix} \lambda I_3 & \mathbf{0}_{3 \times 3} & {}^e p & \mathbf{0}_{3 \times 3} & \mathbf{0}_{3 \times 3} & \mathbf{0}_{3 \times 3} & \mathbf{0}_{3 \times 3} \\ \mathbf{0}_{3 \times 3} & \mathbf{0}_{3 \times 3} & \mathbf{0}_{3 \times 1} & I_3 & \mathbf{0}_{3 \times 3} & \mathbf{0}_{3 \times 3} & \mathbf{0}_{3 \times 3} \\ \mathbf{0}_{2 \times 3} & -k_1 \Upsilon & \mathbf{0}_{2 \times 1} & D_1 & \Upsilon & \mathbf{0}_{3 \times 3} & -k_1 \Upsilon R^T \\ \mathbf{0}_{3 \times 3} & \lambda R & R^b v & D_2 & \mathbf{0}_{3 \times 3} & \mathbf{0}_{3 \times 3} & \mathbf{0}_{3 \times 3} \\ \mathbf{0}_{3 \times 3} & \mathbf{0}_{3 \times 3} & \mathbf{0}_{3 \times 1} & \mathbf{0}_{3 \times 3} & \mathbf{0}_{3 \times 3} & \Xi & \mathbf{0}_{3 \times 3} \\ \mathbf{0}_{2 \times 3} & k_1^2 \Upsilon & \mathbf{0}_{2 \times 1} & D_3 & \mathbf{0}_{2 \times 3} & \mathbf{0}_{3 \times 3} & k_1^2 \Upsilon R^T \\ \mathbf{0}_{3 \times 3} & -\lambda k_1 R \Lambda & D_4 & D_5 & \lambda R \Gamma & \mathbf{0}_{3 \times 3} & \lambda k_1 R \Lambda R^T \end{bmatrix}
\end{aligned}$$

where ${}_E^B R$ has been replaced with R for clarity, $D_i (i = 1 \dots 5)$ are functions of $\lambda, \Theta, {}^B v, \beta_a, {}^E v_w$, and:

$$D_4 = g - k_1 R \Lambda {}^B v + k_1 R \Lambda R^T {}^E v_w + R \Gamma \beta_a$$

where:

$$\Lambda = \begin{bmatrix} 1 & 0 & 0 \\ 0 & 1 & 0 \\ 0 & 0 & 0 \end{bmatrix}$$

All other Lie derivatives of the this system are either linearly dependent on the rows of \mathcal{O}_1 or are trivially zero. The following Lemma can be stated for the rank of \mathcal{O}_5 .

Lemma 1: The matrix \mathcal{O}_5 is rank deficient. It has a column rank of 18 when at least one of ${}^B \dot{v}_x$ and ${}^B \dot{v}_y$ is non-zero.

Proof. Block Gaussian elimination can be used to recover the rank of \mathcal{O}_5 . The notation $\mathcal{O}_5(p, q)$ is used to represent the $(p, q)^{th}$ block, and $\mathcal{O}_5(p, :)$ represents the p^{th} row block of \mathcal{O}_5 .

First, given that $\lambda > 0$, it is possible to divide row block one by λ . Also since block $\mathcal{O}_5(2,4)$ is an identity matrix, all non-zero entries in $\mathcal{O}_5(:,4)$ can be eliminated. Rotational transformation matrix R is orthogonal and thus is always full rank. Thus $\mathcal{O}_5(4,:)$ can be multiplied by $(\lambda R)^{-1}$. Ξ transforms the body rotational rates to Euler rotational rates and is also full rank. Thus it is possible to multiply $\mathcal{O}_5(5,:)$ by Ξ^{-1} . Next $\mathcal{O}_5(7,:)$ is multiplied by $\frac{k_1}{\lambda} \Upsilon R^T$ and the result is added to $\mathcal{O}_5(6,:)$ to obtain:

$$\mathcal{O}_5 \rightarrow \begin{bmatrix} \mathbf{I}_3 & \mathbf{0}_{3 \times 3} & {}^e\mathbf{p} & \mathbf{0}_{3 \times 3} & \mathbf{0}_{3 \times 3} & \mathbf{0}_{3 \times 3} & \mathbf{0}_{3 \times 3} \\ \mathbf{0}_{3 \times 3} & \mathbf{0}_{3 \times 3} & \mathbf{0}_{3 \times 1} & \mathbf{I}_3 & \mathbf{0}_{3 \times 3} & \mathbf{0}_{3 \times 3} & \mathbf{0}_{3 \times 3} \\ \mathbf{0}_{2 \times 3} & -k_1 \Upsilon & \mathbf{0}_{2 \times 1} & \mathbf{0}_{2 \times 3} & \Upsilon & \mathbf{0}_{3 \times 3} & -k_1 \Upsilon R^T \\ \mathbf{0}_{3 \times 3} & \mathbf{I}_3 & \frac{{}^b\mathbf{v}}{\lambda} & \mathbf{0}_{3 \times 3} & \mathbf{0}_{3 \times 3} & \mathbf{0}_{3 \times 3} & \mathbf{0}_{3 \times 3} \\ \mathbf{0}_{3 \times 3} & \mathbf{0}_{3 \times 3} & \mathbf{0}_{3 \times 1} & \mathbf{0}_{3 \times 3} & \mathbf{0}_{3 \times 3} & \mathbf{I}_3 & \mathbf{0}_{3 \times 3} \\ \mathbf{0}_{2 \times 3} & \mathbf{0}_{2 \times 3} & \mathbf{D}_7 & \mathbf{0}_{2 \times 3} & \mathbf{0}_{2 \times 3} & \mathbf{0}_{3 \times 3} & \mathbf{0}_{2 \times 3} \\ \mathbf{0}_{3 \times 3} & -\lambda k_1 R \Lambda & \mathbf{D}_4 & \mathbf{0}_{3 \times 3} & \lambda R \Gamma & \mathbf{0}_{3 \times 3} & \lambda k_1 R \Lambda R^T \end{bmatrix}$$

where

$$\begin{aligned} \mathbf{D}_7 &= \frac{k_1}{\lambda} \Upsilon R^T (\mathbf{g} - k_1 R \Lambda {}^B v + k_1 R \Lambda R^T {}^E v_w + R \Gamma \beta_a) \\ &= \frac{k_1}{\lambda} \Upsilon (R^T \mathbf{g} - k_1 ({}^B \mathbf{v} - R^T {}^E \mathbf{v}_w)) \\ &= \frac{k_1}{\lambda} \Upsilon {}^B \dot{\mathbf{v}} = \frac{k_1}{\lambda} \begin{bmatrix} {}^B \dot{v}_x & {}^B \dot{v}_y \end{bmatrix}^T. \end{aligned}$$

If either one of ${}^B \dot{v}_x$ and ${}^B \dot{v}_y$ is non-zero, then at least one element of the 2×1 vector \mathbf{D}_7 is non-zero and it is possible to eliminate all remaining non-zero elements of $\mathcal{O}_5(:,3)$. This results in $\mathcal{O}_5(4,:)$ being all zero except in column block two. Thus all remaining non-zero

elements in $\mathcal{O}_5(:, 2)$ can be eliminated to obtain:

$$\mathcal{O}_5 \rightarrow \begin{bmatrix} \mathbf{I}_3 & \mathbf{0}_{3 \times 3} & \mathbf{0}_{3 \times 1} & \mathbf{0}_{3 \times 3} & \mathbf{0}_{3 \times 3} & \mathbf{0}_{3 \times 3} & \mathbf{0}_{3 \times 3} \\ \mathbf{0}_{3 \times 3} & \mathbf{0}_{3 \times 3} & \mathbf{0}_{3 \times 1} & \mathbf{I}_3 & \mathbf{0}_{3 \times 3} & \mathbf{0}_{3 \times 3} & \mathbf{0}_{3 \times 3} \\ \mathbf{0}_{2 \times 3} & \mathbf{0}_{2 \times 3} & \mathbf{0}_{2 \times 1} & \mathbf{0}_{2 \times 3} & \Upsilon & \mathbf{0}_{3 \times 3} & -k_1 \Upsilon R^T \\ \mathbf{0}_{3 \times 3} & \mathbf{I}_3 & \mathbf{0}_{3 \times 1} & \mathbf{0}_{3 \times 3} & \mathbf{0}_{3 \times 3} & \mathbf{0}_{3 \times 3} & \mathbf{0}_{3 \times 3} \\ \mathbf{0}_{3 \times 3} & \mathbf{0}_{3 \times 3} & \mathbf{0}_{3 \times 1} & \mathbf{0}_{3 \times 3} & \mathbf{0}_{3 \times 3} & \mathbf{I}_3 & \mathbf{0}_{3 \times 3} \\ \mathbf{0}_{1 \times 3} & \mathbf{0}_{1 \times 3} & 1 & \mathbf{0}_{1 \times 3} & \mathbf{0}_{1 \times 3} & \mathbf{0}_{1 \times 3} & \mathbf{0}_{1 \times 3} \\ \mathbf{0}_{3 \times 3} & \mathbf{0}_{3 \times 3} & \mathbf{0}_{3 \times 1} & \mathbf{0}_{3 \times 3} & \lambda R \Gamma & \mathbf{0}_{3 \times 3} & \lambda k_1 R \Lambda R^T \end{bmatrix}$$

after removing an all-zero row corresponding to one of the elements of D_7 . Now consider the following sub-matrix made up of all remaining non-zero elements of row blocks $\mathcal{O}_5(3, :)$ and $\mathcal{O}_5(7, :)$:

$$\mathcal{O}_6 = \begin{bmatrix} \Upsilon & -k_1 \Upsilon R^T \\ \lambda R \Gamma & \lambda k_1 R \Lambda R^T \end{bmatrix}.$$

Multiplying $\mathcal{O}_6(2, :)$ by $(\lambda R)^{-1}$ and then adding $\Upsilon \mathcal{O}_6(2, :)$ to $\mathcal{O}_6(1, :)$ and finally moving the last row of $\mathcal{O}_6(2, :)$ to immediately after $\mathcal{O}_6(1, :)$ the following can be obtained:

$$\mathcal{O}_6 \rightarrow \begin{bmatrix} \mathbf{I}_3 & \mathbf{0}_{3 \times 3} \\ \mathbf{0}_{2 \times 3} & k_1 \Upsilon R^T \end{bmatrix}$$

which has a column rank of 5 for any given R . Thus returning to \mathcal{O}_5 it is possible to see that its column rank is 18. ■

5.5.3 Unobservable Modes

The above analysis proves that the dimension of the null space of \mathcal{O}_5 is 1. It is easy to show that

$$\mathbf{n}_1 = \begin{bmatrix} \mathbf{0}_{3 \times 1}; & \mathbf{0}_{3 \times 1}; & 0; & \mathbf{0}_{3 \times 1}; & \mathbf{0}_{3 \times 1}; & \mathbf{0}_{3 \times 1}; & R \begin{bmatrix} 0 \\ 0 \\ 1 \end{bmatrix} \end{bmatrix} \quad (5.5)$$

is a basis for the said null space.

Consider a function of states given by $g(\mathbf{X}) = {}^B v_{wz} = \Gamma(:, 3)^T {}^B \mathbf{v}_w = \Gamma(:, 3)^T R^T {}^E \mathbf{v}_w$, where $\Gamma(:, 3)$ is the third column of Γ . The gradient of $g(\mathbf{X})$ with respect to the state is given by:

$$\frac{\partial g(\mathbf{X})}{\partial \mathbf{X}} = \begin{bmatrix} \mathbf{0}_{1 \times 3} & \mathbf{0}_{1 \times 3} & 0 & \mathbf{D}_8 & \mathbf{0}_{1 \times 3} & \mathbf{0}_{1 \times 3} & R(3, :) \end{bmatrix} \quad (5.6)$$

where \mathbf{D}_8 is a function of Θ , ${}^E \mathbf{v}_w$ and $R(3, :)$ is the third column of R . The gradient of $g(\mathbf{X})$ is not orthogonal to \mathbf{n}_1 as $\mathbf{n}_1^T \frac{\partial g(\mathbf{X})}{\partial \mathbf{X}} = 1 \neq 0$. Thus, making use of property 1 of Section 2.7, it can be concluded that the unobservable dimension corresponding to \mathbf{n}_1 is the ${}^B z$ component of wind. It is possible to also conclude that all other states including the position, velocity and orientation of the quadrotor remain observable, despite wind disturbances.

5.5.4 Removing Unobservable Modes

The unobservable mode, namely the ${}^B z$ component of wind velocity, needs to be removed from the state vector to proceed with the estimator design. This can be achieved by replacing ${}^E \mathbf{v}_w$ by ${}^B \mathbf{v}_w$ in the state vector and rewriting the process and measurement equations of Table 5.1 in-terms of ${}^B \mathbf{v}_w$. As the third column of both \bar{D}_L and Υ comprises of zero-vectors, the resulting process and measurement equations are independent of the third component of ${}^B \mathbf{v}_w$. Therefore ${}^B v_{wz}$ can be removed from the state vector. The time evolution of the remaining two components of the wind velocity $\tilde{\mathbf{v}}_w = [{}^B v_{wx} \ {}^B v_{wy}]^T$ can be given by:

$$\begin{aligned} \dot{\tilde{\mathbf{v}}}_w &= \Upsilon_B^E R {}^E \dot{\mathbf{v}}_w \\ &= \Upsilon_B^E R \boldsymbol{\eta}_w \\ &= \tilde{\boldsymbol{\eta}}_w. \end{aligned}$$

The zero-mean WGN and the uncorrelatedness assumptions made regarding the wind velocity in Section 5.5.1 implies that $\boldsymbol{\eta}_w \in \mathcal{N}(\mathbf{0}_{3 \times 1}, \sigma_w^2 \mathbf{I}_3)$ where σ_w is the assumed standard deviation wind velocity in $\{E\}$. As $\dot{\tilde{\mathbf{v}}}_w$ is obtained by an affine transformation of ${}^E \dot{\mathbf{v}}_w$, then

the noise associated with that, which is defined as $\tilde{\boldsymbol{\eta}}_w$ here, is also Gaussian distributed with $\tilde{\boldsymbol{\eta}}_w \in \mathcal{N}(\mathbf{0}_{2 \times 1}, \sigma_w^2 \Upsilon \frac{B}{E} R \mathbf{I}_3 \frac{E}{B} R) \equiv \mathcal{N}(\mathbf{0}_{2 \times 1}, \sigma_w^2 \mathbf{I}_2)$. This implies that $\tilde{\boldsymbol{\eta}}_w \equiv \Upsilon \boldsymbol{\eta}_w$.

The process and measurement equations for the wMA-VIF after the removal of the unobservable mode are summarized in Table 5.2. An observability analysis similar to that carried out in Section 5.5.2 can be employed to show that same condition in *Lemma 1* is sufficient to ensure that the system described by the equations in Table 5.2 is locally-weakly observable. Therefore, the equations in Table 5.2 can be combined with the EKF mechanization equations of Table 2.1 to implement a state estimator for the quadrotor MAV based on the wMA-VIF design.

One important aspect of such an implementation is that it, as opposed to the design by Waslander and Wang [44], does not make the assumption that the ${}^B z$ component of wind velocity is zero or small. The removal of the ${}^B z$ component of wind velocity from the state vector is made possible by the fact that the process equation for ${}^B \dot{\boldsymbol{v}}$ is independent of the ${}^B z$ component of wind. Therefore, the presence of a non-zero ${}^B z$ component of wind does not affect the accuracy of the wMA-VIF state estimates, as will be demonstrated in Section 5.6.

5.5.5 Similarity between MA-VIF and wMA-VIF

The accelerometer measurement equation in Table 5.2 can be rewritten by combining $\boldsymbol{\beta}_a$ and ${}^B \boldsymbol{v}_w$ as they both have the same process dynamics:

$$\boldsymbol{h}_i = \begin{bmatrix} {}^B a_x \\ {}^B a_y \end{bmatrix} = -k_1 \Upsilon {}^B \boldsymbol{v} + \Upsilon \tilde{\boldsymbol{\beta}}_a + \Upsilon \boldsymbol{\eta}_a \quad (5.7)$$

where $\tilde{\boldsymbol{\beta}}_a = \boldsymbol{\beta}_a + k_1 {}^B \boldsymbol{v}_w$. This implies that it is not possible to distinguish between the effect of wind and bias by only analysing the accelerometer measurements. Wind velocity and accelerometer biases are only made observable as the same replacement cannot be made in the dynamics for ${}^B \dot{\boldsymbol{v}}$ in the process Equation of Table 5.2. However, when the wind effects are not explicitly modelled, this implies that the accelerometer bias estimates will be a combination of both the actual bias itself and the body frame wind velocity. This

TABLE 5.2: Modified Model-Aided Visual-Inertial Fusion Estimator with Wind States

Process Equations	
$\begin{bmatrix} {}^E\dot{\mathbf{p}} \\ {}^B\dot{\mathbf{v}} \\ \dot{\lambda} \\ \dot{\Theta} \\ \dot{\beta}_a \\ \dot{\beta}_g \\ \dot{\tilde{\mathbf{v}}}_w \end{bmatrix}$	$\begin{bmatrix} {}^E R {}^B \mathbf{v} \\ {}^B R \mathbf{g} + ({}^B a_z - \beta_{az}) \mathbf{e}_3 - \bar{D}_L ({}^B \mathbf{v} - {}^B R^T {}^E \mathbf{v}_w) + \boldsymbol{\eta}_v \\ \eta_\lambda \\ \Xi({}^B \boldsymbol{\omega}_g - \beta_g + \boldsymbol{\eta}_g) \\ \boldsymbol{\eta}_{\beta a} \\ \boldsymbol{\eta}_{\beta g} \\ \tilde{\boldsymbol{\eta}}_w \end{bmatrix}$
Measurement Equations	
$\mathbf{h}_i = \begin{bmatrix} {}^B a_x \\ {}^B a_y \end{bmatrix}$	$= -k_1 \Upsilon ({}^B \mathbf{v} - {}^B \mathbf{v}_w) + \Upsilon \boldsymbol{\beta}_a + \Upsilon \boldsymbol{\eta}_a$
$\mathbf{h}_{vp} = \lambda {}^e \mathbf{p} + \boldsymbol{\eta}_p$	
$\mathbf{h}_{vo} = \Theta + \boldsymbol{\eta}_o$	

behaviour can be seen in the experimental results of the MA-VIF presented in Section 5.7.1.

5.6 Simulations of wMA-VIF

The wMA-VIF design was tested using the same wind simulations that were used in Section 5.4. The position and orientation estimation errors when the wind velocity is constant are presented in Fig. 5.5. This figure demonstrates that the wMA-VIF estimates are not affected by the component of wind velocity in the ${}^B z$ direction, thus validating the method employed to remove the unobservable component in Section 5.5.4.

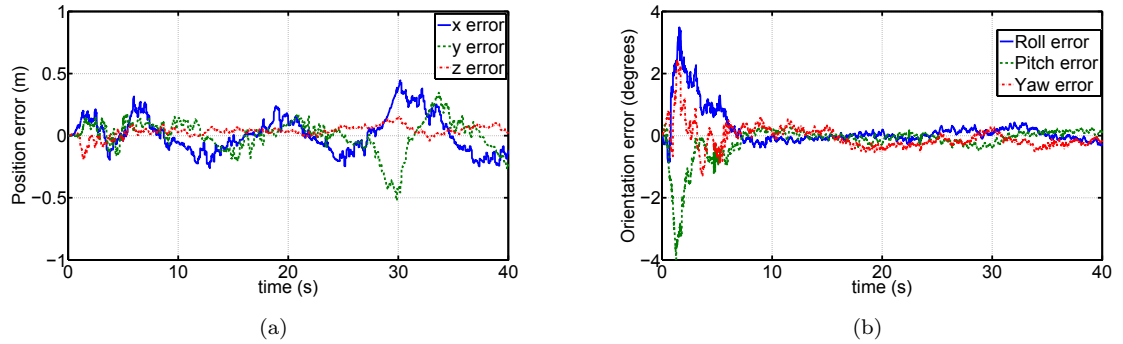


FIGURE 5.5: Estimation errors of the wMA-VIF from constant wind simulations (a) - position (b) - orientation

Figure 5.6, presents the position, velocity and orientation estimation errors of both the MA-VIF and wMA-VIF when the quadrotor was affected by rapidly varying wind gusts shown in Fig. 5.1(b). This figure clearly demonstrates that, in contrast to the MA-VIF, the wMA-VIF is capable of producing accurate pose estimates even amidst strong wind gusts. Figure 5.7 presents the estimated wind velocity and the wind velocity estimation errors of the wMA-VIF. The wMA-VIF only estimates the ${}^B\mathbf{x}$, ${}^B\mathbf{y}$ components of wind but it can be seen that these two components are accurately estimated despite non-zero ${}^B\mathbf{v}_{wz}$ component. The wind velocity estimation error increases after about 35s when a high frequency wind gust begins affecting the quadrotor MAV. This increased error is due to the violation of the smoothly varying wind velocity assumption made during the design of the wMA-VIF. Such estimation errors due to rapid variations in wind velocity can be reduced by increasing the magnitude of the process noise in wind dynamics of the wMA-VIF process equation. However, doing so increases the noise in pose estimates and therefore, a suitable compromise has to be made.

5.7 Experimental Evaluation of wMA-VIF

There are two aspects of wMA-VIF that need to be evaluated experimentally. First is the accuracy of MAV pose estimates amidst wind disturbances. Second is the accuracy of the wind velocity estimate. While the former could be easily analysed by performing the experiments in the Vicon environment, analysing the accuracy of wind estimates is

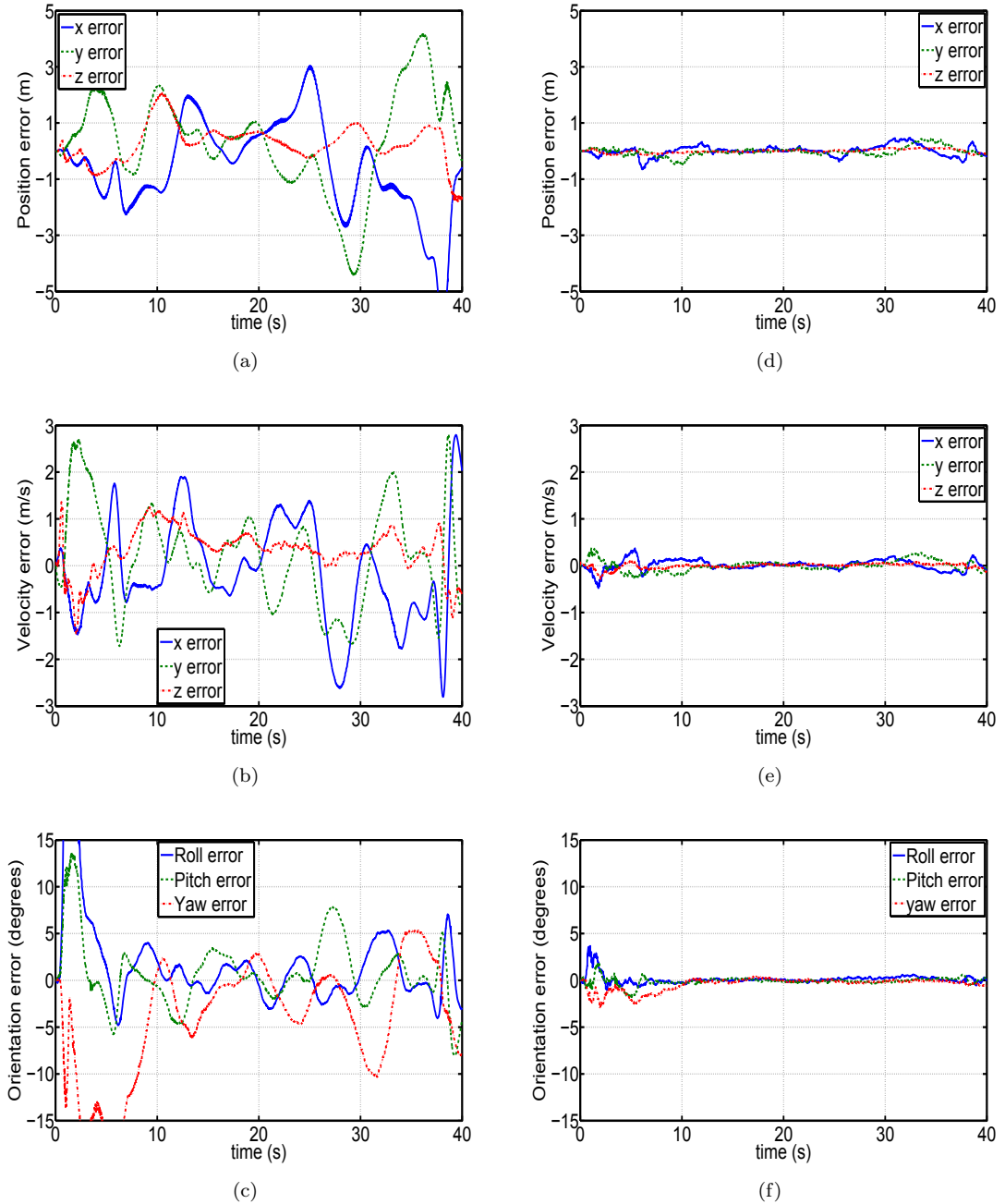


FIGURE 5.6: Estimation errors of MA-VIF (a) - (c) and wMA-VIF (d) - (f) for simulations with wind gusts.

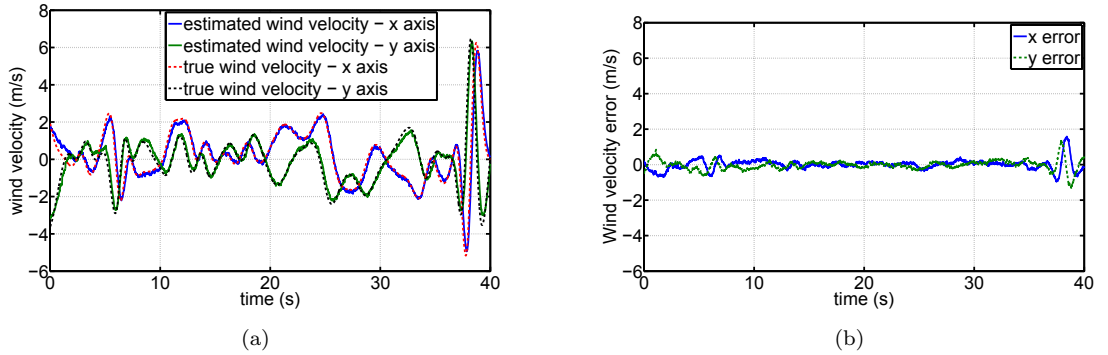


FIGURE 5.7: True and estimated wind velocity (a) and the wind estimation errors (b) of wMA-VIF wind gust simulations.

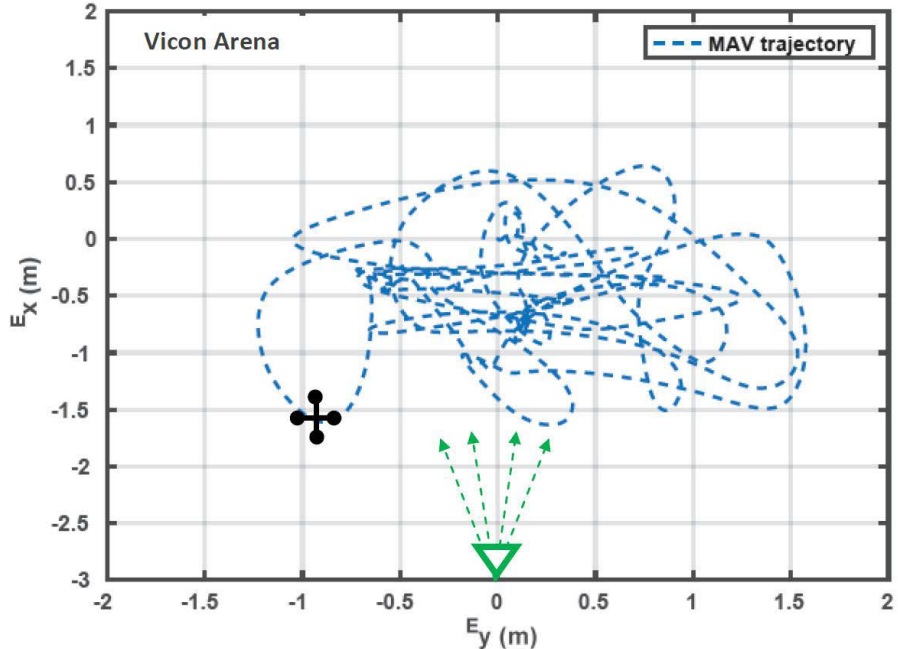


FIGURE 5.8: Top view of the motion capture environment showing the setup for wind disturbed experiments. The coordinates shown denotes the world coordinate frame $\{E\}$. Black cross denotes the ARDrone and the green traingle denotes the fan, both not to scale. The fan was positioned statically and the green arrows denotes the non-uniform airflow of the fan.

difficult unless the experiments are performed in a wind tunnel. Due to the unavailability of a suitable wind tunnel to perform quadrotor MAV flights, the experimental results presented here will only validate the wind velocity estimation accuracy in a qualitative manner. A quantitative analysis of the wind velocity estimation accuracy was already presented with the aid of simulations in the previous section.

An industrial grade fan was placed on one side of the Vicon capture area to simulate windy conditions. This fan was used to generate wind predominately along the x axis of $\{E\}$ frame (see Fig. 5.8). A hand held anemometer was used to obtain a rough measurement of the wind speed which, at the centre of the arena, was about 1.5m/s.

The main purpose of the experiments presented here is to verify the ability of the wMA-VIF to produce accurate vehicle pose estimates amidst wind disturbances, given the measurements from a suitable VSLAM algorithm and an IMU. For this reason, it was chosen to simulate the VSLAM algorithm using the Vicon motion estimates. This was achieved by first sub-sampling the Vicon position and orientation estimates at 10Hz and then scaling and adding suitable levels of noise according to Equation (4.1) with $\lambda = 1/5$, $\eta_p \in \mathcal{N}(0, (1/5)^2)$ (1 m standard deviation in metric scale) and $\eta_o \in \mathcal{N}(0, 4)$ (2 degrees standard deviation). The resulting position and orientation measurements are illustrated in Fig. 5.9.

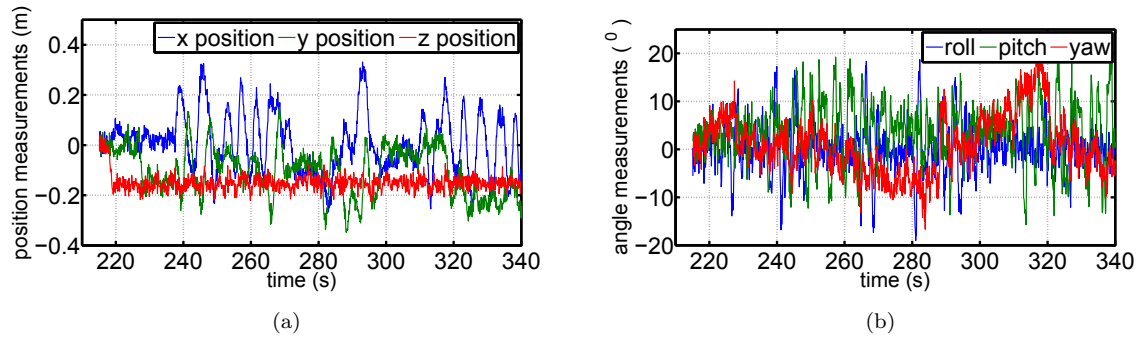


FIGURE 5.9: Simulated VSLAM position (a) and orientation (b) measurements utilised for the wMA-VIF experiments. The position measurements have been scaled using a $\lambda = 0.2$.

5.7.1 Results

Two different estimation tasks were performed with the data gathered by operating the quadrotor MAV in the Vicon environment. First the IMU and simulated VSLAM measurements were processed using the loosely-coupled MA-VIF implementation of Chapter 4. Second, the same set of data was processed by an implementation of the wMA-VIF design proposed in this chapter. For both experiments, position, velocity and scale estimates are presented in Fig. 5.10, 5.11 and 5.12 respectively.

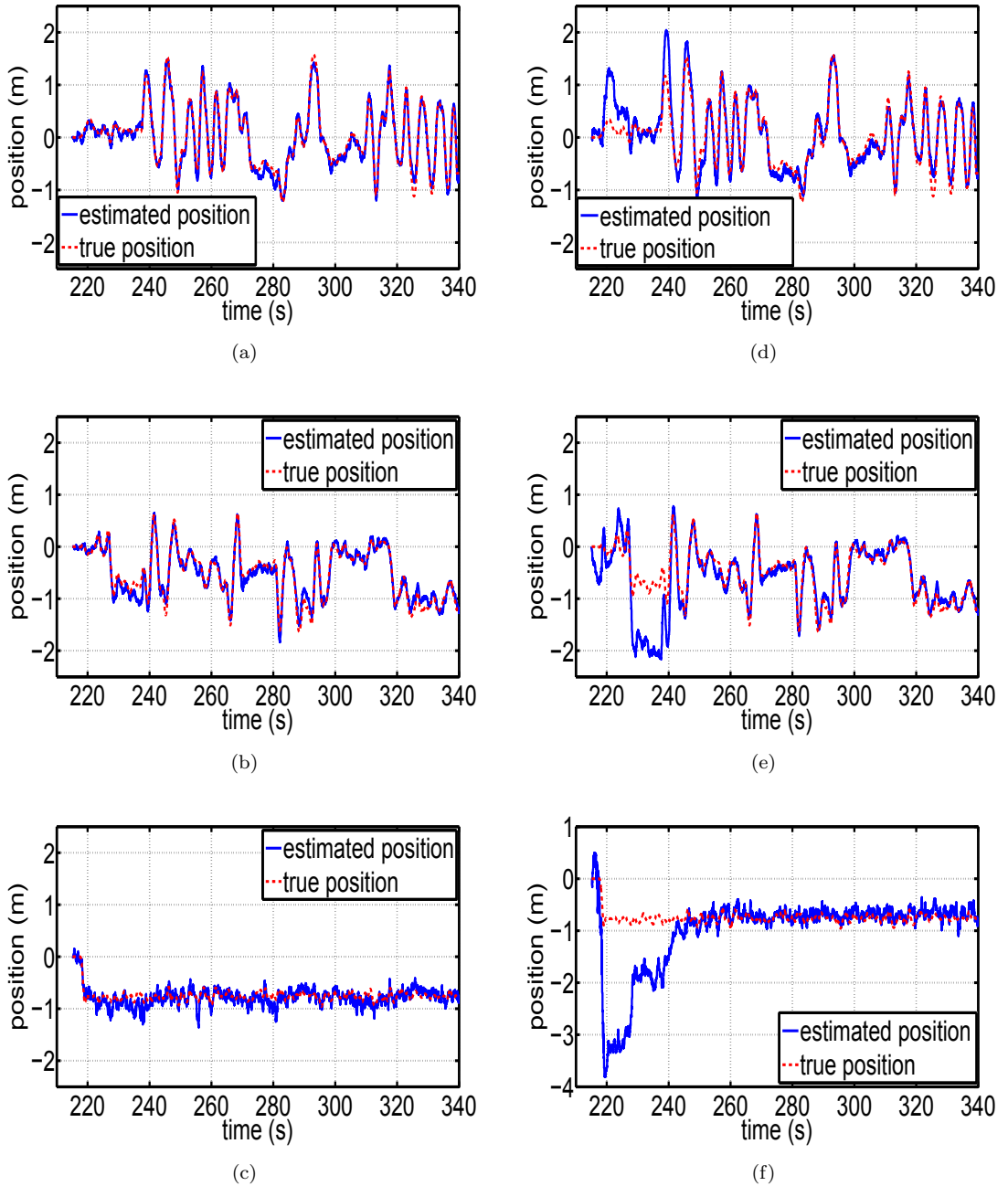


FIGURE 5.10: Position estimates with ground truth of wMA-VIF (a) - x, (b) - y, (c) - z and MA-VIF (d) - (f) for the wind disturbed experiments.

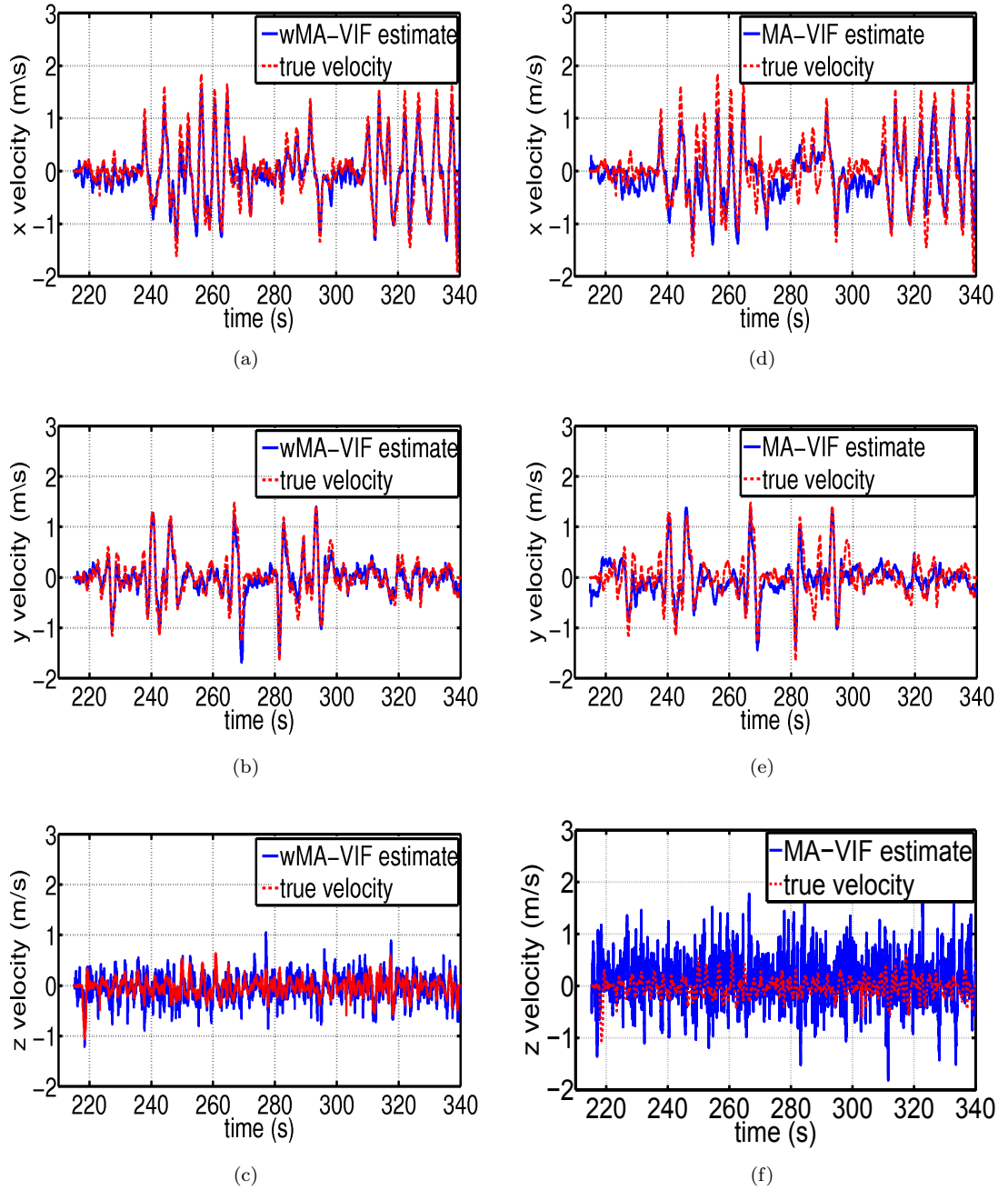


FIGURE 5.11: Velocity estimates with ground truth of wMA-VIF (a) - (c) and MA-VIF (d) - (f) for the wind disturbed experiments.

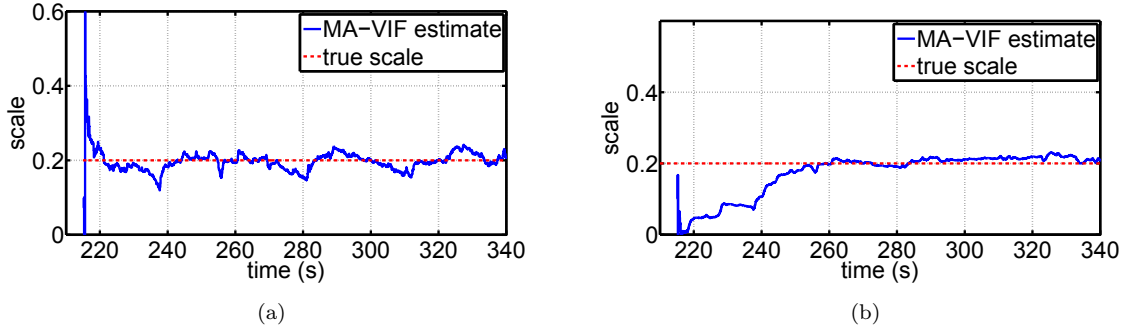


FIGURE 5.12: Scale estimate of the wMA-VIF (a) and MA-VIF (b) for the wind disturbed experiments.

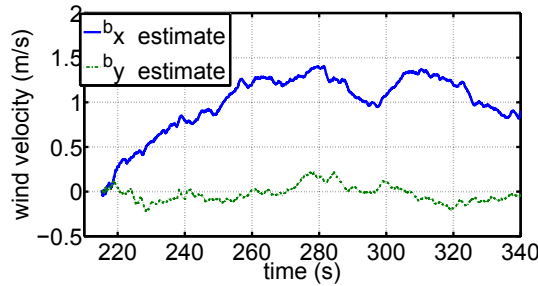


FIGURE 5.13: Wind velocity estimates of the wMA-VIF for the wind disturbed experiments.

Figures 5.10 and 5.12 illustrate that the wMA-VIF is capable of quickly recovering the scale λ and producing accurate position and velocity estimates in metric scale. The scale estimate closely matches the true value. It can also be seen that the scale estimate begins to deviate from the true value when the both Bv_x , Bv_y are approximately zero. This agrees with the theoretical observability results. The wind velocity estimates for the wMA-VIF are presented in Fig. 5.13. The wind is predominantly in the x direction as is expected. Also, both the x and y components of wind estimates rapidly decrease when the quadrotor MAV moves away from the origin along y axis (for example 290s - 300s and 320s - 340s). These observations indicate that the wind estimates are qualitatively accurate.

Focusing on the estimates of MA-VIF, it can be seen that the scale estimate takes longer to converge. As a result, MA-VIF produces substantial errors in position estimates during the first twenty seconds. Even in the long run, the MA-VIF scale estimate does not converge to the true value, creating inconsistencies in position estimates. Although the position estimates of the MA-VIF seems comparable with those of wMA-VIF after the

first twenty seconds, the advantage of the latter can be seen when the estimation accuracy is quantitatively analysed. Velocity estimation errors of both estimators presented in Fig. 5.14 illustrates this fact clearly. RMS velocity estimation errors for the wMA-VIF were 0.21, 0.15 and 0.17 for the x,y,z axes respectively and 0.38, 0.29 and 0.57 for MA-VIF. Also the estimation errors of the MA-VIF are considerably larger than the 3σ bounds of the estimation error predicted by the filter, thus indicating an inconsistent estimator design. This result is as expected. The MA-VIF assumes zero wind disturbances, thus resulting in over-confident and less accurate estimates when this assumption is violated.

The accelerometer bias estimates of both estimators are presented in Fig. 5.15. Note the similarity in MA-VIF bias estimates for the Bx , By axes and the wind velocity estimates for the same axes for the wMA-VIF. In fact, as expected, it can be seen that the bx , by accelerometer biases of MA-VIF agrees closely with the values predicted for $\tilde{\beta}_a$ by Equation 5.7. This is also the reason why MA-VIF estimates are not substantially erroneous, despite using an insufficient process model.

5.8 Discussion and Limitations

Wind disturbances can be a serious concern for lightweight MAVs operating in close proximity to obstacles. In the absence of GPS measurements and air speed measurements, state estimation for safe operation of MAVs operating in such an environment becomes a difficult task. This chapter focused on two problems related to that task. The first problem was determining whether any of the model-aided state estimators designed in the previous chapters can be successfully employed when the quadrotor MAV was affected by wind. Through simulations and experimental results, it was shown that the MAVE, which only employed inertial measurements, could still produce accurate orientation estimates when wind velocity is smoothly varying. Simulations and experimental results also showed that the MA-VIF could still produce reasonably accurate pose estimates, given that the wind disturbances are small and smoothly varying. When faced with strong wind disturbances however, the simulations showed that the MA-VIF estimates become substantially inaccurate.

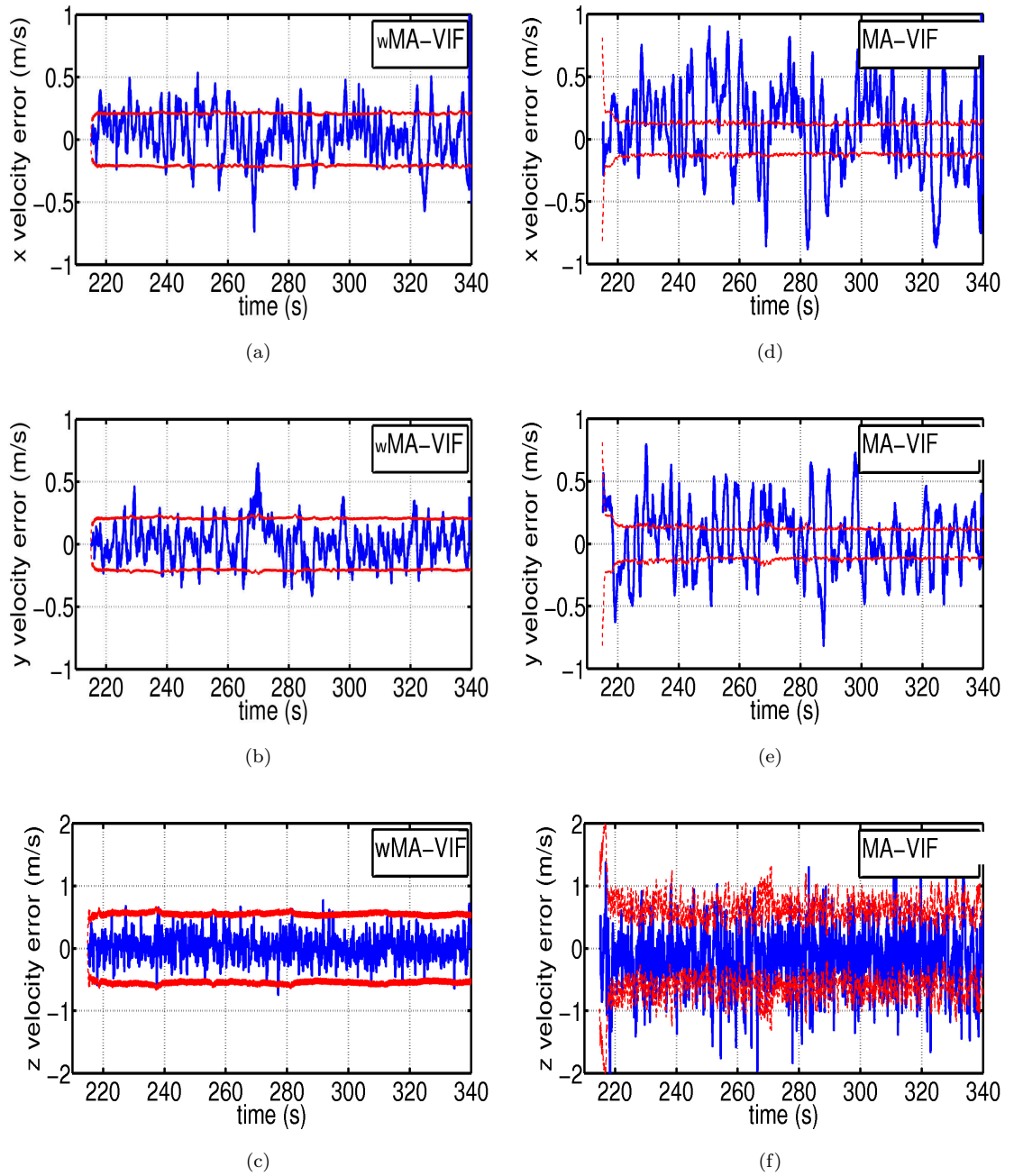


FIGURE 5.14: Velocity estimation error with 3σ bounds of wMA-VIF (a) - (c) and MA-VIF (d) - (f) for the wind disturbed experiments.

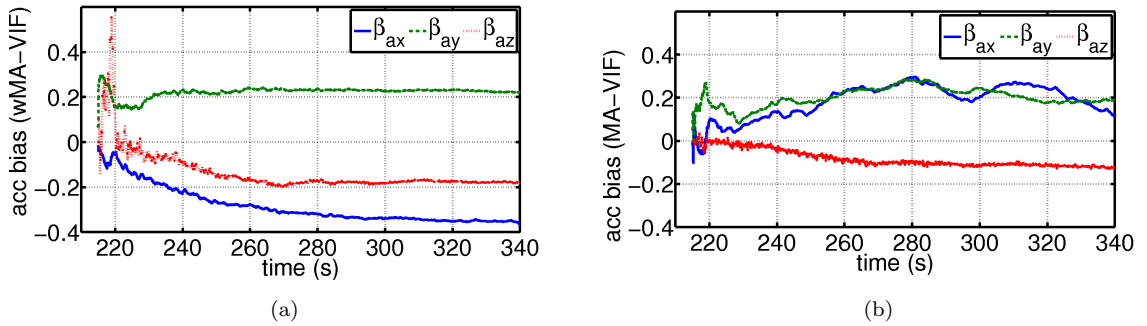


FIGURE 5.15: Accelerometer bias estimate of the wMA-VIF (a) and MA-VIF (b) for the wind disturbed experiments.

The second problem this chapter focused on stems from this last observation. Is it possible to improve the accuracy of the MA-VIF when faced with strong wind disturbances by simultaneously attempting to estimate the wind velocity? If so, under what conditions does this become possible? The answers to these two questions were provided by designing and analysing the wMA-VIF. It was shown that it is indeed possible to simultaneously estimate the pose of the MAV and the horizontal component of wind velocity, only employing a monocular camera and an IMU.

One limitation of the approach presented here is that it cannot estimate the full wind velocity vector. It is possible to estimate the remaining component of wind velocity if a suitable dynamic model for the quadrotor MAV thrust can be derived. Propeller thrust is a function of the wind velocity incident on the propeller plane. If an analytic expression for this function is available, then it is possible to incorporate that into the wMA-VIF design and this has the potential to make the ${}^B\mathbf{z}$ component of wind observable. Initial work in this direction can be found in the recent publication by Allibert et al. [83]. However, this approach was not pursued any further in this thesis, as deriving such an expression for propeller thrust is beyond its scope.

Chapter 6

Conclusions

This thesis focused on the task of GPS-denied state estimation for quadrotor MAVs. It introduced the MAV dynamic model as an additional information source that can be employed to improve the accuracy of such estimators. To incorporate this dynamic model in a principled manner into state estimator designs, a set of simplified equations that capture the relationship between the acceleration, velocity and attitude of the quadrotor MAV were derived.

Three different estimation tasks were analysed in this thesis to identify the improvements brought about by incorporating the quadrotor dynamic model into the state estimation process. In each task, an observability analysis was performed to identify the observable states and the conditions under which those states become observable. Based on these analyses, an EKF based state estimator that seamlessly fuses the information available the sensor measurements and the quadrotor MAV dynamic model was presented to achieve the objective of each task. These designed estimators were benchmarked by comparing their performance to the performance of similar designs which either did not benefit from the quadrotor MAV dynamic model or designs which incorporated an insufficient description of the quadrotor motion. Extensive simulation and real-world experimental results were employed in the benchmarking process.

6.1 Summary of Contributions

6.1.1 Quadrotor MAV Dynamic Model

Though several detailed derivations of the quadrotor MAV translational dynamics can be found in the literature, none of those were derived with the intention of employing the dynamic equations in state estimation. This thesis presented a simplified dynamic model that satisfactorily captures the translational motion of the quadrotor MAV. The dynamic model presented can be easily incorporated into most state estimator designs that make use of inertial measurements for pose estimation. It has not been presented in the previous literature in this simplified form.

6.1.2 Model-Aided Inertial Estimators

Most commercially-off-the-shelf quadrotor MAVs are equipped with a GPS receiver and an IMU. When GPS measurements are not available, state-of-the-art estimation algorithms for quadrotor MAVs can only produce a drift free estimate of the MAV attitude using the IMU measurements. This thesis presented an improved estimator design that combines the IMU measurements with the quadrotor MAV dynamic model. Through observability analysis and experimental results it was demonstrated that this design is capable of not only improving the attitude estimation accuracy but also of producing a drift free estimate of the lateral and longitudinal components of the quadrotor MAV body frame velocity.

6.1.3 Model-Aided Visual-Inertial Fusion

The information contained in both the IMU measurements and the quadrotor MAV dynamic model is not sufficient to estimate the full pose of the MAV. Monocular cameras provide a rich source of information that can be employed for to augment this sensor configuration. State estimator designs that combine the visual information from a monocular camera and inertial information from an IMU are widely used in mobile robotic applications. However, these designs can only produce consistent results when the camera-IMU platform undergoes specific motion patterns. This thesis illustrated that the restrictions

on the quadrotor MAV motion can be substantially relaxed by incorporating the MAV dynamic model into state estimators that fuse camera and IMU measurements. Through an observability analysis and simulations it demonstrated that such a state estimator can produce consistent state estimates whenever the quadrotor MAV is in motion. Through experimental results, this thesis also illustrated that both the accuracy and speed of visual inertial fusion algorithms can be improved by the fusion of the three available information sources - IMU measurements, camera images and quadrotor MAV dynamic model - in a single coherent estimator.

6.1.4 Model-Aided State Estimation amidst Wind Disturbances

The dynamic model of the quadrotor MAV is dependent on the ambient wind velocity incident on the MAV. This dependency can be neglected for operations in spacious indoor environments. However, when the quadrotor MAV is operating outdoors, the effects of wind needs to be explicitly modelled in the quadrotor dynamic model if it is to be employed to aid the state estimation. This thesis demonstrated how the model-aided state estimation framework can be extended to incorporate the effects of wind. An observability analysis was presented to identify the observable states of the wind affected system and the underlying conditions on the MAV trajectory for ensuring the observability. A state estimator design based on the insights gained through the observability analysis was proposed to simultaneously estimate the pose of the quadrotor and the components of the wind velocity that affect the quadrotor MAV. Extensive simulations and experimental results were presented to illustrate that the incorporation of the effect of wind on the quadrotor MAV dynamic model results in improved state estimation accuracy when compared to a model-aided design in which wind effects were neglected.

6.2 Discussion of Limitations

There are several limitations of the model-aided state estimation framework discussed in this thesis. First, all three model-aided state estimator designs assumed that the value of the induced drag coefficient is known. Though this value only needs to be calculated

once for a given quadrotor design and can be estimated offline as detailed in Appendix A, that process requires ground truth state estimates such as those available from a Vicon motion capture system. When such a system is not available, it may be possible to employ GPS velocity measurements for the same purpose. However, the resulting estimate of the induced drag coefficient would be less accurate than that obtained using Vicon ground truth states.

The second limitation of the model-aided state estimation framework applies to the visual-inertial fusion estimators proposed in chapters four and five. Both the MA-VIF and wMA-VIF formulations become unobservable when the quadrotor MAV is stationary. For example, this can occur when the quadrotor MAV is hovering in-place to inspect a given area of its environment. The loss of scale observability would cause the position estimates to deviate from the true value. If these position estimates are being used by a feedback control algorithm for trajectory control, then the quadrotor MAV would begin to drift away from the hover position. Though this motion would cause the MA-VIF to become observable again, the resulting motion pattern due to this phenomenon means that such a system would not be able to keep the quadrotor MAV in perfect hover. It is possible to limit the drift in position estimates during hover in an ad hoc manner, by reducing the magnitude of the process noise in scale when the quadrotor MAV velocity approaches zero. A more principled solution to this problem is discussed in Section 6.3.

The third limitation of the model-aided state estimation framework applies to the wMA-VIF design proposed in Chapter 5. The wMA-VIF is only able to estimate two components of the wind velocity vector, as the third component is not incorporated into the MAV dynamics. Chapter 6 illustrated that, irrespective of this missing component, the MAV pose could still be estimated accurately, even when the third component of wind velocity vector is non-zero. However, this lack of information about ${}^B v_{wz}$ becomes problematic if the wind velocity estimates are to be employed for purposes such as improving the trajectory tracking performance of the MAV.

6.3 Future Work

This thesis demonstrated that the accuracy and robustness of quadrotor MAV state estimators can be improved by employing the MAV dynamic model as an information source. There are a number of additional improvements that can be incorporated into those estimators to further increase their utility. Though these improvements are beyond the scope of this thesis, they are presented here with the hope that they may inspire future work on MAV state estimation.

The loss of observability of the state estimator designs presented in Chapters 4 and 5 during hover manoeuvres of the quadrotor and the problems associated with that were discussed in the previous section. One way to overcome these problems is to employ an Image Based Visual Servoing (IBVS) approach similar to the one discussed by Hamel and Mahony [84]. An IBVS algorithm aims to solve the control problem of a dynamic system without explicitly deriving estimates for the states that need to be controlled. Instead, an IBVS algorithm operates by generating a control law that minimize the errors of features directly on the image plane. Hamel and Mahony [84] demonstrated that such an algorithm could employ visual and inertial information to successfully stabilize a VTOL MAV in hover. However, an IBVS algorithm alone would not be sufficient to control the trajectory of a MAV, as it relies on the knowledge of the expected image locations of features to derive a measure of MAV pose error. This information is available when the objective is hovering the MAV at an arbitrary location; the expected position of features is exactly their current position. In contrast, when the objective is to control the MAV along a given trajectory in a previously unknown environment, then the expected feature locations at each point in the trajectory are unknown. As a result, an IBVS algorithm cannot be employed for controlling the motion along an arbitrary trajectory. Therefore, for a quadrotor MAV, the ideal solution would be a combination of a model-aided state estimation algorithm and an IBVS algorithm similar to the one presented in [84]. The best way to combine these two algorithms remains to be investigated.

Future work should also look into the possibility of extending the wMA-VIF design to obtain an estimate of the complete wind velocity vector affecting the quadrotor MAV. One way to achieve this is to develop a dynamic model for the quadrotor MAV thrust.

Propeller thrust is a function of the wind velocity incident on the propeller plane. If an analytic expression for this function is available, then it is possible to incorporate that into the wMA-VIF design. This incorporation has the potential to make the Bz component of wind observable. Initial work in this direction can be found in the recent publication by Allibert et al. [83]. There, a closed-form estimate of the Bz component of the quadrotor MAV velocity with respect to the air is derived using measurements of propeller rotational rates and motor electrical properties, without accounting for the noise in those measurements. A more principled way to achieve this would be to incorporate those measurements directly into a model-aided state estimator with suitable noise models. However, the expressions for those measurements are complex functions of states and much work remains to be done to develop suitable noise models to describe their measurement errors.

Appendix A

Estimating the Propeller Drag Coefficient

Accelerometer measurements expressed in Equation 2.16 can be employed in a least-squares manner to obtain an offline estimate of the lumped propeller drag coefficient k_1 , when ground truth state estimates are available. Consider the measurement of ${}^B\mathbf{x}$, ${}^B\mathbf{y}$ accelerometers:

$$\begin{bmatrix} {}^B a_x \\ {}^B a_y \end{bmatrix} = \begin{bmatrix} -k_1 {}^B v_x + \beta_{ax} + \eta_{ax} \\ -k_1 {}^B v_y + \beta_{ay} + \eta_{ay} \end{bmatrix}. \quad (\text{A.1})$$

The body frame velocity ${}^B\mathbf{v}$ can be obtained by differentiating the Vicon position measurements and then transforming to the body coordinate frame using the Vicon orientation estimates. The numerical differentiation of Vicon position estimates does not introduce considerable quantization noise as the Vicon ground truth estimates are obtained at 120Hz. Therefore, assuming that the biases are constant over short time periods, this equation can be solved in a least-squares manner to obtain an estimate of $k_1, \beta_{ax}, \beta_{ay}$ given sufficient measurements. Note that once the value of k_1 has been determined for a specific quadrotor MAV, it can be used for all successive estimation tasks, given that the physical structure or the weight of the quadrotor has not been changed. For the ARDrone quadrotor MAV

used in the experiments of this thesis, the value of k_1 has been determined to be 0.57 without the protective hull.

Appendix B

ID Monocular SLAM and Tightly-Coupled MA-VIF

This appendix presents the basic building blocks of an open-source implementation of the Inverse-Depth (ID) monocular SLAM by Civera et al. [45], [75]. It also details how this implementation was adopted to implement the tightly-coupled Model-Aided Visual-Inertial Fusion (MA-VIF) described in section 4.7. More details of the inverse-depth parametrization for monocular SLAM can be found in [65].

B.1 Inverse-Depth monocular SLAM

Civera and Montiel [75] implemented the ID monocular SLAM algorithm using an EKF. The state vector consisted of the position, orientation and linear and angular velocity of the camera with respect to the world coordinate frame: $\mathbf{X} = \begin{bmatrix} {}^E\mathbf{p} & {}^E\mathbf{v} & \mathbf{q} & {}^B\boldsymbol{\Omega} \end{bmatrix}$, where the orientation was represented using the unit quaternion \mathbf{q} . The process model made use of the assumption that the linear and angular accelerations are negligible given that the

camera motion is smooth:

$$\dot{\mathbf{X}} = \begin{bmatrix} {}^E\dot{\mathbf{p}} \\ {}^E\dot{\mathbf{v}} \\ \dot{\mathbf{q}} \\ {}^B\dot{\Omega} \end{bmatrix} = \begin{bmatrix} {}^E\mathbf{v} \\ \boldsymbol{\eta}_v \\ \frac{1}{2}\mathbf{q} \oplus {}^B\bar{\Omega} \\ \boldsymbol{\eta}_{\Omega} \end{bmatrix} \quad (\text{B.1})$$

where ${}^B\bar{\Omega}$ denotes the pure quaternion formed from ${}^B\Omega$, \oplus denotes quaternion multiplication and $\boldsymbol{\eta}_v, \boldsymbol{\eta}_{\Omega}$ denote 3×1 vectors of zero-mean WGN noise variables.

In addition, the state vector is augmented with the position of environmental features as they are observed for the first time in images. All new features are initialised in the inverse-depth parametrization with a 6-D vector:

$$\mathbf{y}_i = [x_i \ y_i \ z_i \ \vartheta_i \ \varphi_i \ \rho_i] \quad (\text{B.2})$$

which models a 3-D point located at $[X_i \ Y_i \ Z_i]$ as:

$$\mathbf{p}_i = \begin{bmatrix} X_i \\ Y_i \\ Z_i \end{bmatrix} = \begin{bmatrix} x_i \\ y_i \\ z_i \end{bmatrix} + \frac{1}{\rho} \mathbf{m}(\vartheta_i, \varphi_i) \quad (\text{B.3})$$

$$\mathbf{m}(\vartheta_i, \varphi_i) = [\cos \varphi_i \sin \vartheta_i \ -\sin \varphi_i \ \cos \varphi_i \cos \vartheta_i]^T$$

where $[x_i \ y_i \ z_i]^T$ is the location of the camera when the feature was first observed, $\mathbf{m}(\vartheta_i, \varphi_i)$ denotes the unit vector from that location to the feature with ϑ_i, φ_i respectively the azimuth and elevation of that unit vector with respect to $\{E\}$. Also, ρ_i is the inverse of the depth to the feature along that unit vector. The environmental features are considered as stationary and thus they are represented in the process model with zero-dynamics:

$$\dot{\mathbf{p}}_i = \mathbf{0}.$$

Measurements to the current set of features in the state vector are made in each camera image. To express these measurements mathematically, the position of the feature needs to be expressed in $\{C\}$: ${}^C\mathbf{p}_i = [{}^Cp_{ix} \ {}^Cp_{iy} \ {}^Cp_{iz}]$. For an ID features, this can be given

by:

$${}^C\mathbf{p}_i = R^T \left(\rho_i \begin{pmatrix} \begin{bmatrix} x_i \\ y_i \\ z_i \end{bmatrix} - {}^e\mathbf{p} \end{pmatrix} + \mathbf{m}(\vartheta_i, \varphi_i) \right) \quad (\text{B.4})$$

The actual measurements are the projection of the features onto the image plane assuming a pinhole camera. The final visual measurement equation can be obtained after the application of camera calibration:

$$\mathbf{h}_c = \begin{bmatrix} u \\ v \end{bmatrix} = \begin{bmatrix} u_0 - \frac{f {}^C p_{iy}}{{}^C p_{ix}} \\ v_0 - \frac{f {}^C p_{iz}}{{}^C p_{ix}} \end{bmatrix} + \begin{bmatrix} \eta_{ui} \\ \eta_{vi} \end{bmatrix} \quad (\text{B.5})$$

where f is the camera focal length, u_0, v_0 is the camera's principal point and η_{ui}, η_{vi} are WGN variables with 1 pixel standard deviation.

To measure the bearing to the current set of features in the state vector, their location in each image needs to be identified. This is the well known feature correspondence problem. In this implementation it is solved by a two step process. As each feature is initialized, an image patch around that feature is stored in a separate vector. For each new image, the current best estimate of the camera pose and feature position are used to predict the region that the feature is most likely to appear. A correlation based search within this region using the stored feature patch is used to identify the exact feature location with sub-pixel accuracy. This search is computationally expensive and is only performed for features that are likely to appear in the current image, given the camera orientation and field-of-view.

B.2 Tightly-coupled Model-Aided Visual-Inertial Fusion

The open source implementation [75] of Inverse-Depth (ID) monocular SLAM algorithm[45] discussed in the previous section was used as the basis for implementing the tightly-coupled Model-Aided VIF (MA-VIF) algorithm detailed in section 4.7. This section discusses the how the quadrotor dynamic model was incorporated into that implementation.

The state vector of the ID monocular SLAM implementation was augmented with 6 additional states to account for the accelerometer and gyroscope biases β_a, β_g . The process model for the camera pose and IMU biases (Equation B.1) was replaced by the same process model employed for the loosely-coupled MA-VIF presented in Table 4.3, except for the state λ which was removed as it is not required in a tightly-coupled formulation. Similar to the loosely-coupled MA-VIF, Euler angles were used to represent the orientation $\{B\}$, given that the quadrotor MAV is operated in a manner that prevents the associate singularities. The environmental feature initialization and management was not changed and the bearing measurement equation for the feature also remained unchanged. In addition to those measurements, the tightly-coupled MA-VIF formulation also makes use of the same accelerometer measurement equation (Equation 3.14) as the loosely-coupled formulation. The process and measurement equations for the tightly-coupled MA-VIF are summarised in Table B.1.

One major advantage of the ID parametrization for monocular SLAM is the ability to perform un-delayed initialization of environmental features. At the first observation, each feature is incorporated into the state vector using the 6 parameter vector \mathbf{y}_i with a mean inverse depth of ρ_{i0} and a variance in inverse depth σ_{i0} . Several rule of thumb guidelines on how to select values for both ρ_{i0} and σ_{i0} can be found in [45]. The idea is to set ρ_{i0} such that the range of depths from the minimum expected depth to infinite depth is covered within the $2\sigma_{i0}$ bound. While these rules generally provided good results for vision only experiments, some difficulties were faced when fusion with inertial information was attempted. In this case, it was observed that features that are considerably further away than the closest feature tend to end up behind the camera after the first EKF update step, especially when the camera is moving toward the features. Other authors have noted the same behaviour when attempting to incorporate metric scale information to EKF based monocular SLAM algorithms using ID parametrization [85]. To overcome this issue, features were initialized at approximately the mean depth of features in the environment rather than at the depth of the closest feature. With just a simple visual inspection of the environment, it was possible to set an approximate value to the initial feature depth that would perform satisfactorily. Subsequently, the mean depth of features was calculated online using the set of currently tracked features.

TABLE B.1: Tightly-Coupled Model-Aided Visual-Inertial Fusion Estimator

Process Equations	
$\begin{bmatrix} {}^E\dot{\mathbf{p}} \\ {}^B\dot{\mathbf{v}} \\ \dot{\Theta} \\ \dot{\beta}_a \\ \dot{\beta}_g \\ \dot{\mathbf{p}}_1 \\ \vdots \\ \dot{\mathbf{p}}_n \end{bmatrix}$	$= \begin{bmatrix} {}^E R {}^B v \\ {}^E R g + ({}^B a_z - \beta_{az}) e_3 - \bar{D}_L {}^B v + \boldsymbol{\eta}_v \\ -\Xi(\beta_g + \boldsymbol{\eta}_g) \\ \boldsymbol{\eta}_{\beta a} \\ \boldsymbol{\eta}_{\beta g} \\ \mathbf{0} \\ \vdots \\ \mathbf{0} \end{bmatrix}$
Measurement Equations	
$\mathbf{h}_i = \begin{bmatrix} {}^B a_x \\ {}^B a_y \end{bmatrix} = \Upsilon(\bar{D}_L {}^B v + \boldsymbol{\beta}_a + \boldsymbol{\eta}_a)$	
$\mathbf{h}_c = \begin{bmatrix} u_i \\ v_i \end{bmatrix}$	$= \begin{bmatrix} u_0 - \frac{f^C p_{iy}}{C p_{ix}} \\ v_0 - \frac{f^C p_{iz}}{C p_{ix}} \end{bmatrix} + \begin{bmatrix} \eta_{ui} \\ \eta_{vi} \end{bmatrix}$

Bibliography

- [1] J. Zou, K. Su, and H. Tso. The modeling and implementation of tri-rotor flying robot. *Artificial Life and Robotics*, 17(1):86 – 91, 2012.
- [2] P. Pounds, R. Mahony, P. Hynes, and J. Roberts. Design of a four-rotor aerial robot. In *Proc. Australasian Conference on Robotics and Automation (ACRA)*, pages 145–150, 2002.
- [3] R. Baránek and F. Solc. Modelling and control of a hexa-copter. In *Proc. IEEE 13th International Carpathian Control Conference (ICCC)*, pages 19 – 23, 2012.
- [4] P. E. I. Pounds. *Design, construction and control of a large quadrotor micro air vehicle*. PhD thesis, Australian National University, 2007.
- [5] D. Mellinger, N. Michael, and V. Kumar. Trajectory generation and control for precise aggressive maneuvers with quadrotors. In *Proc. International Symposium on Experimental Robotics*, Dec. 2010.
- [6] D. Mellinger and V. Kumar. Minimum snap trajectory generation and control for quadrotors. In *Proc. IEEE International Conference on Robotics and Automation (ICRA)*, pages 2520 – 2525, 2011.
- [7] M. Turpin, N. Michael, and V. Kumar. Trajectory design and control for aggressive formation flight with quadrotors. *Autonomous Robots*, 33(1-2):143 – 156, 2012.
- [8] J. Kim, S. Sukkarieh, and S. Wishart. Real-time navigation, guidance, and control of a UAV using low-cost sensors. In *Proc. Field and Service Robotics*, pages 299 – 309. Springer, 2006.

- [9] H. Lim, J. Park, D. Lee, and H. J. Kim. Build your own quadrotor: Open-source projects on unmanned aerial vehicles. *IEEE Robotics and Automation Magazine*, 19(3):33 – 45, 2012.
- [10] William J. Hughes Technical Center. Global positioning system (GPS) standard positioning service (SPS) performance analysis report. http://www.nstb.tc.faa.gov/reports/PAN85_0414.pdf, 2014.
- [11] A. Bachrach, S. Prentice, R. He, and N. Roy. RANGE - robust autonomous navigation in GPS-denied environments. *Journal of Field Robotics*, 28(5):644–666, 2011.
- [12] A. Bachrach, S. Prentice, R. He, P. Henry, A. S. Huang, M. Krainin, D. Maturana, D. Fox, and N. Roy. Estimation, planning and mapping for autonomous flight using an RGB-D camera in GPS-denied environments. *International Journal of Robotic Research*, 31(11):1320–1343, 2012.
- [13] G. Nützi, S. Weiss, D. Scaramuzza, and R. Siegwart. Fusion of IMU and vision for absolute scale estimation in monocular SLAM. *Journal of Intelligent and Robotic Systems*, 61:287 – 299, 2011.
- [14] P. Martin and E. Salaun. The true role of accelerometer feedback in quadrotor control. In *Proc. IEEE International Conference on Robotics and Automation (ICRA)*, pages 1623 –1629, May 2010.
- [15] D. Abeywardena, S. Kodagoda, R. Munasinghe, and G. Dissanayake. A virtual odometer for a quadrotor micro aerial vehicle. In *Proc. Australasian Conference on Robotics and Automation (ACRA)*, Dec. 2011.
- [16] G. Dissanayake, S. Sukkarieh, E. Nebot, and H.D. Whyte. A new algorithm for the alignment of inertial measurement units without external observation for land vehicle applications. In *Proc. IEEE International Conference on Robotics and Automation (ICRA)*, pages 2274 –2279, 1999.
- [17] M. Koifman and I. Y. Bar-Itzhack. Inertial navigation system aided by aircraft dynamics. *IEEE Transactions on Control Systems Technology*, 7(4):487 – 493, 1999.

- [18] R. Mahony, M. Euston, J. Kim, P. Coote, and T. Hamel. A non-linear observer for attitude estimation of a fixed-wing unmanned aerial vehicle without gps measurements. *Transactions of the Institute of Measurement and Control*, 33(6):699 – 717, 2011.
- [19] D. Abeywardena, S. Kodagoda, G. Dissanayake, and R. Munasinghe. Improved state estimation in quadrotor MAVs: A novel drift-free velocity estimator. *IEEE Robotics Automation Magazine*, 20(4):32 – 39, Dec. 2013.
- [20] D. Abeywardena, Z Wang, S. Kodagoda, and G. Dissanayake. Visual-inertial fusion for quadrotor Micro Air Vehicles with improved scale observability. In *Proc. IEEE International Conference on Robotics and Automation (ICRA)*, pages 3133 – 3138, May 2013.
- [21] D. Abeywardena and G. Dissanayake. Tightly-coupled model aided visual-inertial fusion for quadrotor micro air vehicles. In *Field and Service Robotics*, volume 105 of *Springer Tracts in Advanced Robotics*, pages 153 – 166. Springer International Publishing, 2015.
- [22] D. Abeywardena, Z Wang, G. Dissanayake, S. L. Waslander, and S. Kodagoda. Model-aided state estimation for quadrotor micro air vehicles amidst wind disturbances. In *Proc. IEEE/RSJ International Conference on Intelligent Robots and Systems (IROS)*, Sept. 2014.
- [23] D. Abeywardena, Z Wang, S. Kodagoda, and G. Dissanayake. Model-aided visual-inertial fusion for quadrotor micro air vehicles with improved observability. *IEEE Transactions on Robotics*, under review.
- [24] J. Stuelpnagel. On the parametrization of the three-dimensional rotation group. *SIAM Review*, 6(4):422 – 430, 1964.
- [25] T. Hamel, R. Mahony, R. Lozano, and J. P. Ostrowski. Dynamic modelling and configuration stabilization for an x4-flyer. In *Proc. IFAC World Congress on Automatic Control*, 2002.
- [26] J Gordon Leishman. *Principles of Helicopter Aerodynamics*. Cambridge university press, 2000.

- [27] P. Pounds, R. Mahony, J. Gresham, P. Corke, and J. Roberts. Towards dynamically favourable quad-rotor aerial robots. In *Proc. Australasian Conference on Robotics and Automation (ACRA)*, December 2004.
- [28] S. Bouabdallah, P. Murrieri, and R. Siegwart. Design and control of an indoor micro quadrotor. In *Proc.s of the 2005 IEEE International Conference on Robotics and Automation*, volume 5, pages 4393–4398 Vol.5, April 2004.
- [29] S. Bouabdallah and R. Siegwart. Backstepping and sliding-mode techniques applied to an indoor micro quadrotor. In *Proc. of the 2005 IEEE International Conference on Robotics and Automation*, pages 2247–2252, April 2005.
- [30] H. Huang, G. M. Hoffmann, S. L. Waslander, and C. J. Tomlin. Aerodynamics and control of autonomous quadrotor helicopters in aggressive maneuvering. In *Proc. IEEE International Conference on Robotics and Automation (ICRA)*, pages 3277–3282, 2009.
- [31] R. Mahony, V. Kumar, and P. Corke. Multirotor aerial vehicles: Modeling, estimation, and control of quadrotor. *IEEE Robotics and Automation Magazine*, 19(3):20 – 32, 2012.
- [32] R. Leishman, J. Macdonald, R. Beard, and T. McLain. Quadrotors and accelerometers: State estimation with an improved dynamic model. *IEEE Control Systems Magazine*, 34(1):28 – 41, Feb. 2014.
- [33] M. Bangura and R. Mahony. Real-time model predictive control for quadrotors. In *Proc. The 19th World Congress of the International Federation of Automatic Control (IFAC)*, 2014.
- [34] M. Park and Y. Gao. Error and performance analysis of MEMS-based inertial sensors with a low-cost GPS receiver. *Sensors*, 8(4):2240–2261, 2008.
- [35] J. L. Crassidis, F. L. Markley, and Y. Cheng. Survey of nonlinear attitude estimation methods. *Journal of Guidance, Control, and Dynamics*, 30(1):12 – 28, 2007.
- [36] R. E. Kalman. A new approach to linear filtering and prediction problems. *Journal of Basic Engineering*, 82(1):35 – 45, 1960.

- [37] P. S. Maybeck. *Stochastic Models, Estimation, and Control*, volume 1. Academic International Press, 1979.
- [38] J. Kelly and G. S. Sukhatme. Visual-inertial sensor fusion: Localization, mapping and sensor-to-sensor self-calibration. *International Journal of Robotic Research*, 30(1):56 – 79, 2011.
- [39] R. Mahony, T. Hamel, and J. M. Pflimlin. Nonlinear complementary filters on the special orthogonal group. *IEEE Transactions on Automatic Control*, 53(5):1203 – 1218, June 2008.
- [40] R. Hermann and A. Krener. Nonlinear controllability and observability. *IEEE Transactions on Automatic Control*, 22(5):728 – 740, Oct. 1977.
- [41] A. Martinelli. State estimation based on the concept of continuous symmetry and observability analysis: The case of calibration. *IEEE Transactions on Robotics*, 27(2):239 – 255, April 2011.
- [42] F. M. Mirzaei and S. I. Roumeliotis. A Kalman filter-based algorithm for IMU-camera calibration: Observability analysis and performance evaluation. *IEEE Transactions on Robotics*, 24(5):1143 – 1156, 2008.
- [43] G. Hoffmann, D. G. Rajnarayan, S. L. Waslander, D. Dostal, J. S. Jang, and C. J. Tomlin. The stanford testbed of autonomous rotorcraft for multi agent control (STAR-MAC). In *Proc. The 23rd Digital Avionics Systems Conference*, volume 2, pages 12–E. IEEE, 2004.
- [44] S. L. Waslander and C. Wang. Wind disturbance estimation and rejection for quadrotor position control. In *AIAA Infotech Aerospace Conference and AIAA Unmanned Unlimited Conference*, 2009.
- [45] J. Civera, O. G. Grasa, A. J. Davison, and J. M. M. Montiel. 1-point RANSAC for extended Kalman filtering: Application to real-time structure from motion and visual odometry. *Journal of Field Robotics*, 27(5):609–631, 2010.
- [46] J. Y. Bouguet. Camera calibration toolbox for matlab. http://www.vision.caltech.edu/bouguetj/calib_doc/, 2008.

- [47] J. Lobo and J. Dias. Relative pose calibration between visual and inertial sensors. *The International Journal of Robotics Research*, 26(6):561 – 575, 2007.
- [48] D. Titterton and J. L. Weston. *Strapdown Inertial Navigation Technology*, volume 17. IET, 2004.
- [49] M. M. Kuritsky, M. S. Goldstein, I. A. Greenwood, H. Lerman, J. E. McCarthy, T. Shanahan, M. Silver, and J. H. Simpson. Inertial navigation. *Proceedings of the IEEE*, 71(10):1156–1176, 1983.
- [50] D. A. MacKenzie. *Inventing Accuracy: A Historical Sociology of Nuclear Missile Guidance*. MIT press, 1993.
- [51] B. Barshan and H. F. Durrant-Whyte. Inertial navigation systems for mobile robots. *IEEE Transactions on Robotics and Automation*, 11(3):328 – 342, 1995.
- [52] E. Gai, K. Daly, J. Harrison, and L. Lemos. Star-sensor-based satellite attitude/attitude rate estimator. *Journal of Guidance, Control, and Dynamics*, 8(5):560 – 565, 1985.
- [53] S. I. Roumeliotis, G. Sukhatme, and G. A. Bekey. Smoother based 3D attitude estimation for mobile robot localization. In *Proc. IEEE International Conference on Robotics and Automation (ICRA)*, pages 1979 – 1986, 1999.
- [54] M. L. Psiaki, F. Martel, and P. K. Pal. Three-axis attitude determination via Kalman filtering of magnetometer data. *Journal of Guidance, Control, and Dynamics*, 13(3): 506 – 514, 1990.
- [55] M. Hua. Attitude observers for accelerated rigid bodies based on GPS and INS measurements. In *Proc. 48th IEEE Conference on Decision and Control (CDC)*, pages 8071 – 8076, 2009.
- [56] J. Marins, X. Yun, E. R. Bachmann, R. B. McGhee, and M. J. Zyda. An extended Kalman filter for quaternion-based orientation estimation using MARG sensors. In *Proc. IEEE International Conference on Intelligent Robots and Systems (IROS)*, pages 2003 – 2011, 2001.

- [57] J. Vaganay, M. Aldon, and A. Fournier. Mobile robot attitude estimation by fusion of inertial data. In *Proc. IEEE International Conference on Robotics and Automation (ICRA)*, pages 277 – 282, 1993.
- [58] P. Martin and E. Salaün. Design and implementation of a low-cost observer-based attitude and heading reference system. *Control Engineering Practice*, 18(7):712 – 722, 2010.
- [59] P Aggarwal, Z Syed, X Niu, and N El-Sheimy. A standard testing and calibration procedure for low cost mems inertial sensors and units. *Journal of navigation*, 61(02):323–336, 2008.
- [60] R. Hartley and A. Zisserman. *Multiple View Geometry in Computer Vision*. Cambridge university press, 2003.
- [61] G. Klein and D. Murray. Parallel tracking and mapping for small AR workspaces. In *Proc. 6th IEEE and ACM International Symposium on Mixed and Augmented Reality*, pages 225 – 234, Nov. 2007.
- [62] A. J. Davison. Real-time simultaneous localisation and mapping with a single camera. In *Proc. IEEE International Conference on Computer Vision*, pages 1403 – 1410, 2003.
- [63] P. Smith, I. D. Reid, and A. J. Davison. Real-time monocular slam with straight lines. In *Proc. British Machine Vision Conference*, volume 6, pages 17 – 26, 2006.
- [64] M. Bryson and S. Sukkarieh. Building a robust implementation of bearing-only inertial SLAM for a UAV. *Journal of Field Robotics, Special issue on SLAM in the field*, 24(1-2):113–143, 2007.
- [65] J. Civera, A.J. Davison, and J. Montiel. Inverse depth parametrization for monocular SLAM. *IEEE Transactions on Robotics*, 24(5):932 – 945, Oct. 2008.
- [66] P. Corke, J. Lobo, and J. Dias. An introduction to inertial and visual sensing. *International Journal of Robotic Research*, 26(6):519 – 535, 2007.
- [67] S. Weiss, M. Achtelik, S. Lynen, M. Chli, and R. Siegwart. Real-time onboard visual-inertial state estimation and self-calibration of MAVs in unknown environments. In

- Proc. IEEE International Conference on Robotics and Automation (ICRA)*, pages 957 – 964, May 2012.
- [68] I. Sa, H. He, V. Huynh, and P. Corke. Monocular vision based autonomous navigation for a cost-effective MAV in GPS-denied environments. In *Proc. IEEE/ASME International Conference on Advanced Intelligent Mechatronics (AIM)*, pages 1355 – 1360, 2013.
- [69] E. S. Jones and S. Soatto. Visual-inertial navigation, mapping and localization: A scalable real-time causal approach. *The International Journal of Robotics Research*, 30(4):407 – 430, 2011.
- [70] J. Kim and S. Sukkarieh. Real-time implementation of airborne inertial-SLAM. *Robotics and Autonomous Systems*, 55(1):62 – 71, 2007.
- [71] J. Engel, J. Sturm, and D. Cremers. Camera-based navigation of a low-cost quadrocopter. In *Proc. IEEE/RSJ International Conference on Intelligent Robots and Systems (IROS)*, pages 2815 – 2821, Oct. 2012.
- [72] A. Martinelli. Vision and IMU data fusion: Closed-form solutions for attitude, speed, absolute scale, and bias determination. *IEEE Transactions on Robotics*, 28(1):44 – 60, Feb. 2012.
- [73] M. Achtelik, M. Achtelik, S. Weiss, and R. Siegwart. Onboard IMU and monocular vision based control for MAVs in unknown in- and outdoor environments. In *Proc. IEEE International Conference on Robotics and Automation (ICRA)*, pages 3056 – 3063, May 2011.
- [74] H. Strasdat, J. M. M. Montiel, and A. J. Davison. Scale drift-aware large scale monocular SLAM. In *Proc. Robotics: Science and Systems*, volume 2, 2010.
- [75] J. Civera and J. Montiel. EKF monocular SLAM. <https://openslam.org/ekfmonoslam.html>, 2010.
- [76] D. G. Lowe. Distinctive image features from scale-invariant keypoints. *International Journal of Computer Vision*, 60(2):91 – 110, 2004.

- [77] J. W. Langelaan, N. Alley, and J. Neidhoefer. Wind field estimation for small unmanned aerial vehicles. *Journal of Guidance, Control, and Dynamics*, 34(4):1016 – 1030, 2011.
- [78] J. Kim and S. Sukkarieh. Towards robust airborne slam in unknown wind environments. In *Proc. of the International Conference on Robotics and Automation (ICRA), Orlando, FL, USA*, pages 15–19, 2006.
- [79] D. Zachariah and M. Jansson. Self-motion and wind velocity estimation for small-scale UAVs. In *Proc. IEEE International Conference on Robotics and Automation (ICRA)*, pages 1166 – 1171, 2011.
- [80] P. P. Neumann, S. Asadi, A. J. Lilienthal, M. Bartholmai, and J. H. Schiller. Autonomous gas-sensitive microdrone: Wind vector estimation and gas distribution mapping. *IEEE Robotics and Automation Magazine*, 19(1):50 – 61, 2012.
- [81] J. Milbank, B. Loxton, S. Watkins, and W. H. Melbourne. *Replication of Atmospheric Conditions for the Purpose of Testing MAVs: MAV Flight Environment Project Final Report*. Royal Melbourne Institute of Technology, 2005.
- [82] Military Specification. Flying qualities of piloted airplanes. *United States Department of Defense*, 1980.
- [83] G. Allibert, D. Abeywardena, M. Bangura, and R. Mahony. Estimating body-fixed frame velocity and attitude form inertial measurements for a quadrotor vehicle. In *Proc. IEEE Multi-Conference on Systems and Control*, 2014.
- [84] T. Hamel and R. Mahony. Visual servoing of an under-actuated dynamic rigid-body system: an image-based approach. *IEEE Transactions on Robotics and Automation*, 18(2):187 – 198, 2002.
- [85] R. Munguia and A. Grau. Delayed features initialization for inverse depth monocular SLAM. In *Proc. European Conference on Mobile Robotics*, 2007.